

Synthesis and characterization of phosphate phosphors
with isolated oxygen for white light-emitting diodes

Naoyuki Komuro

February 2016

Synthesis and characterization of phosphate phosphors
with isolated oxygen for white light-emitting diodes

Naoyuki Komuro

Doctoral Program in Applied Physics

Submitted to the Graduate School of
Pure and Applied Sciences
in Partial Fulfillment of the Requirements
for the Degree of Doctor of Philosophy in
Engineering
at the
University of Tsukuba

Abstract

Through a rapid development of countries around the world, a climate change is becoming a crucial word for all of us since its huge impact on natural systems cannot be neglected. Anthropogenic greenhouse gas (GHG) emissions had been causing the temperature rise of combined land and ocean surface, to which recent devastating natural disasters can be related. Variety type of technologies can contribute to solve this crisis, however, solid-state lighting (SSL) based on white light-emitting diode (LED) is the most ready technology for saving energy consumption in a short period.

White LEDs have been intensively developed for SSL with high luminous efficiency, good color quality, long lifetime and the elimination of the risk of hazardous Hg exposure. The replacement of conventional lighting sources by LEDs has accelerated in recent years, driven by the requirement to reduce consumption of both energy and resources, and there is no doubt that LEDs are the most promising lighting sources for the future. The development of phosphors have been contributing to this since the fabrication of white LEDs currently relies on the use of phosphors to convert high energy blue or near-ultraviolet (UV) LED light into lower energy visible light. Most oxide phosphors for LED use have been adapted from those used in cathode ray tubes (CRTs) or lamps, and there are few examples of new oxide-based phosphors that exhibit good excitation and emission performance when combined with blue LEDs. The phosphors suitable for use in practical application for SSL comprise a crystalline oxide, nitride, oxy-nitride, or oxy-fluoride host doped with small amounts of Ce^{3+} or Eu^{2+} ions. They need a large redshift in the $5d$ energy level such that it absorbs in the near-UV or blue region. Discovering the key factors required to achieve a large red shift is crucial for developing suitably improved phosphors for creating better white LEDs. The main goals of this research were to show the prospect in finding new phosphors for SSL based on the oxide system. There are few examples of new oxide-based phosphors which are suitable for a practical use in SSL.

In this work, phosphate system was chosen as a host material to be studied. At the starting point of this research, there was no example of LED phosphors in a phosphate system in terms of excitation wavelength. Finding LED phosphors in phosphate system and analyzing their crystal structures could provide clues to understand key factors for optimizing phosphor performances to LED applications.

This dissertation introduces four phosphate phosphors including completely new crystal phase of phosphors: the red luminescence of $Ca_4(PO_4)_2O:Eu^{2+}$ and $Sr_4(PO_4)_2O:Eu^{2+}$, the yellow luminescence of $Ca_6Ba(PO_4)_4O:Eu^{2+}$ and the blue-green luminescence of $Ca_6Ba(PO_4)_4O:Ce^{3+}$. In which, it is discussed that the relation between crystal structures and its optical characteristics focusing on the strength of crystal fields and the band gaps.

The importance of the higher anion polarizability and the heavy distortion of the coordination polyhedron were highlighted based on the idea of the electronegativity of the cations and the effective coordination numbers (ECoNs). The idea of the ECoN was introduced for describing the degree of distortion, differentiating the eight

Ca (Sr) sites in the $\text{Ca}_4(\text{PO}_4)_2\text{O}:\text{Eu}^{2+}$ or $\text{Sr}_4(\text{PO}_4)_2\text{O}:\text{Eu}^{2+}$ phosphor. The different thermal quenching behaviors for Eu^{2+} dopants in $\text{Sr}_4(\text{PO}_4)_2\text{O}:\text{Eu}^{2+}$ and $\text{Ca}_4(\text{PO}_4)_2\text{O}:\text{Eu}^{2+}$ were also discussed and attributed to the degree of auto/photo-ionization caused by the different band gaps of the materials. The importance of the large band gap of the host lattice in avoiding non-radiative processes of energy relaxation was also confirmed.

Table of Contents

Chapter 1	Introduction.....	1
1.1	Phosphors for white LEDs.....	1
1.2	Aims of the Research	1
1.3	Structure of the Dissertation	2
1.4	References	3
Chapter 2	Technical background	4
2.1	Introduction	4
2.2	Technologies and Environments	4
2.2.1	Solar power generation (Photovoltaic power generation).....	6
2.2.2	Wind power generation.....	7
2.2.3	Nuclear power generation	8
2.2.4	Carbon capture and storage (CCS).....	8
2.3	Lighting	9
2.3.1	A short history of lighting	9
2.3.2	Global LED lighting market.....	12
2.3.3	Opportunity for access to lighting	15
2.4	Assessment Parameters for white LEDs.....	16
2.4.1	Efficiency (external quantum efficiency).....	16
2.4.2	Efficacy.....	17
2.4.3	Color Coordinates.....	17
2.4.4	Correlated Color Temperature (CCT).....	20
2.4.5	Color Rendering Index (CRI).....	20
2.5	White light-emitting diodes	21
2.6	References	26
Chapter 3	Phosphors for white LED applications	28
3.1	Introduction	28
3.2	Photoluminescence processes in phosphors	28
3.3	Luminescence from $4f-4f$ transitions	28
3.4	Luminescence from $5d-4f$ transitions	32
3.5	Oxide phosphors	35
3.6	Nitride and oxy-nitride phosphors	37
3.7	References	43
Chapter 4	Experimental	44
4.1	Introduction	44
4.2	High-temperature ceramic synthesis	44

4.3	Structural characterization.....	44
4.3.1	Rietveld Method.....	48
4.3.2	Structure determination for new phases.....	48
4.3.3	Effective coordination number (ECoN).....	49
4.4	Spectroscopic characterization.....	49
4.4.1	UV-vis reflectance spectroscopy.....	50
4.4.2	Photoluminescence spectroscopy.....	50
4.4.3	Photoluminescence Quantum Efficiency measurement.....	52
4.5	Topographical and elemental analysis (SEM and EDX).....	53
4.6	Characterization in LED.....	53
4.7	References.....	54
Chapter 5	Red luminescence of $\text{Ca}_4(\text{PO}_4)_2\text{O}:\text{Eu}^{2+}$	55
5.1	Introduction.....	56
5.2	Experimental.....	57
5.3	Results.....	57
5.3.1	The structure refinement of $\text{Ca}_4(\text{PO}_4)_2\text{O}:\text{Eu}^{2+}$	57
5.3.2	Optical properties of $\text{Ca}_4(\text{PO}_4)_2\text{O}:\text{Eu}^{2+}$	62
5.3.3	The absorption of $\text{Ca}_4(\text{PO}_4)_2\text{O}$	64
5.4	Discussion.....	65
5.5	Summary.....	71
5.6	References.....	72
Chapter 6	Red luminescence of $\text{Sr}_4(\text{PO}_4)_2\text{O}:\text{Eu}^{2+}$	73
6.1	Introduction.....	74
6.2	Experimental.....	75
6.3	Results and discussion.....	76
6.3.1	The structure refinement of $\text{Sr}_4(\text{PO}_4)_2\text{O}:\text{Eu}^{2+}$	76
6.3.2	Optical properties of $\text{Sr}_4(\text{PO}_4)_2\text{O}:\text{Eu}^{2+}$	80
6.4	Summary.....	93
6.5	References.....	94
Chapter 7	Yellow luminescence of $\text{Ca}_6\text{Ba}(\text{PO}_4)_4\text{O}:\text{Eu}^{2+}$	95
7.1	Introduction.....	96
7.2	Experimental.....	97
7.2.1	Synthetic procedures.....	97
7.2.2	Crystallography.....	97
7.2.3	Optical characterization.....	98
7.2.4	White LED fabrication.....	98
7.3	Results and discussion.....	98

7.3.1	The structure of $\text{Ca}_6\text{Ba}(\text{PO}_4)_4\text{O}$	98
7.3.2	Optical properties of $\text{Ca}_6\text{Ba}(\text{PO}_4)_4\text{O}:\text{Eu}^{2+}$	103
7.3.3	Temperature dependence of the photoluminescence	108
7.3.4	Luminescence from a white LED	110
7.4	Summary	111
7.5	References	112
Chapter 8	Blue-green luminescence of $\text{Ca}_6\text{Ba}(\text{PO}_4)_4\text{O}:\text{Ce}^{3+}$	114
8.1	Introduction	115
8.2	Experimental	116
8.2.1	Synthetic procedures	116
8.2.2	Crystallography and optical characterization	116
8.2.3	White LED fabrication	116
8.3	Results and discussion	117
8.3.1	Phase identification	117
8.3.2	Optical properties of $\text{Ca}_6\text{Ba}(\text{PO}_4)_4\text{O}:\text{Ce}^{3+}$	118
8.3.3	Ce^{3+} , Si^{4+} co-doping in $\text{Ca}_6\text{Ba}(\text{PO}_4)_4\text{O}$	121
8.3.4	Temperature dependence of the photoluminescence	127
8.3.5	Luminescence from a white LED	130
8.4	Summary	131
8.5	References	132
Chapter 9	Conclusions	133
Acknowledgements	135
List of Publications	137

Chapter 1 Introduction

1.1 Phosphors for white LEDs

Through the rapid development of countries around the world, climate change is becoming crucial for all of us, since its huge impact on natural systems cannot be neglected. Anthropogenic greenhouse gas (GHG) emissions have been causing the temperature of combined land and ocean surface to rise, to which recent devastating natural disasters can be related. A variety of technologies can contribute to solving this problem, however solid-state lighting (SSL) based on white light-emitting diodes (LEDs) is the technology most ready for GHG emission cuts by reducing energy consumption in a short period.

White LEDs have been intensively developed for SSL with high luminous efficiency, good color quality and long lifetime. The replacement of conventional lighting sources by LEDs has accelerated in recent years, driven by the requirement to reduce consumption of both energy and resources and eliminate the risk of hazardous Hg exposure, and there is no doubt that LEDs are the most promising lighting sources for the future.

The development of phosphors have been contributing to this development, since the fabrication of white LEDs currently relies on the use of phosphors to convert high energy blue or near-ultraviolet (UV) LED light into lower energy visible light. Although different configurations are possible for white LED based on either a blue LED or a near UV LED,^{1,2} the most common approach currently used for white LEDs is to combine a blue LED with a blue-to-yellow down-converting phosphor, first achieved using $\text{Y}_3\text{Al}_5\text{O}_{12}:\text{Ce}^{3+}$ (YAG: Ce^{3+}). Most oxide phosphors for LED use have been adapted from those used in cathode ray tubes (CRTs) or lamps, and there are few examples of new oxide-based phosphors that exhibit good excitation and emission performance when combined with blue LEDs. The phosphors suitable for use in practical application for SSL comprise a crystalline oxide, nitride, oxy-nitride, or oxy-fluoride host doped with small amounts of Ce^{3+} or Eu^{2+} . They need a large redshift in the $5d$ energy level of the lanthanide element, such that it absorbs in the near-UV or blue region. Discovering the key factors required to achieve a large red shift is crucial for developing suitably improved phosphors necessary for creating better white LEDs.

1.2 Aims of the Research

The main goals of this research were to investigate the prospect of finding new phosphors for SSL based on oxide systems. There are few examples of new oxide-based phosphors which are suitable for practical use in SSL. The desired phosphors for SSL would ideally satisfy the following criteria:

1. Strong and flat excitation band in the near-UV to blue region matching LED light.
2. Intense broad emission band in the green to red region.

3. Minimal thermal quenching of emission up to 200 °C, bearing in mind normal LED operation temperatures.
4. Stable emission under prolonged operation (Reliability).
5. Chemical stability against moisture, light and heat (Durability).
6. Easy and cheap manufacturing in terms of raw materials and synthesis process.

The first criterion is essential for LED applications, which strongly rely on the crystal structure of host materials. In this work, phosphate systems were chosen as the host materials to be studied. At the starting point of this research, there was no example of an LED phosphor in a phosphate system in terms of the suitable excitation wavelength matching to LED light. Finding LED phosphors in phosphate systems and analyzing their crystal structures could provide important information to understand the key factors for optimizing phosphor performances in LED applications. This dissertation will be of interest to both optical materials specialists and the broader materials chemistry community, and also provide stimulation to find new phases and/or phosphors in oxide system for SSL.

1.3 Structure of the Dissertation

This dissertation is organized into nine chapters. Chapters 1 to 4 are introductory chapters. Chapter 2 is a guide to the technical background of this research from technologies and environments to SSL. Chapter 3 introduces phosphors for white LEDs including the fundamentals of photoluminescence in phosphors, with particular attention paid to Ce^{3+} and Eu^{2+} ions. Chapter 4 introduces the experimental methods used for sample preparations and characterizations. Subsequently, Chapter 5, Chapter 6, Chapter 7 and Chapter 8 present the results. In Chapter 5, structure–property correlations in Eu-doped tetra calcium phosphate phosphor, $\text{Ca}_4(\text{PO}_4)_2\text{O}:\text{Eu}^{2+}$, are discussed as a key factor to SSL applications in view of the importance of higher anion polarizability and the distortion of coordination polyhedra. $\text{Ca}_4(\text{PO}_4)_2\text{O}$ has an isolated oxygen atom, which is not related to PO_4 tetrahedra in the structure. In Chapter 6, new red phosphor, $\text{Sr}_4(\text{PO}_4)_2\text{O}:\text{Eu}^{2+}$, is introduced and the importance of higher anion polarizability and the distortion of coordination polyhedra are confirmed by comparing $\text{Ca}_4(\text{PO}_4)_2\text{O}:\text{Eu}^{2+}$ and $\text{Sr}_4(\text{PO}_4)_2\text{O}:\text{Eu}^{2+}$. The importance of large band gap of host materials in avoiding non-radiative energy relaxation processes is also reported. In Chapter 7, a new phase of $\text{Ca}_6\text{Ba}(\text{PO}_4)_4\text{O}$ is introduced in the CaO–BaO– P_2O_5 phase diagram based on the idea of isolated oxygen atoms, and its Eu^{2+} doped derivative is evaluated as a possible phosphor for SSL. In Chapter 8, a new blue-green phosphor, $\text{Ca}_6\text{Ba}(\text{PO}_4)_4\text{O}:\text{Ce}^{3+}$, is derived from a new phase of $\text{Ca}_6\text{Ba}(\text{PO}_4)_4\text{O}$ as a candidate phosphor for SSL with near-UV LEDs. Finally, these results are summarized in Chapter 9 and promising future work is proposed.

1.4 References

- 1 S. Nakamura, S. Pearton and G. Fasol, *The Blue Laser Diode : The Complete Story*, Springer-Verlag, Berlin, 2000, pp. 230-235.
- 2 J. McKittrick, M. E. Hannah, A. Piquette, J. K. Han, J. I. Choi, M. Anc, M. Galvez, H. Lugauer, J. B. Talbot and K. C. Mishra, *ECS J. Solid State Sci. Technol.*, 2013, **2**, R3119.

Chapter 2 Technical background

2.1 Introduction

Technologies have thoroughly changed our life: fast transportations, variety of entertainments, worldwide communications and even longevities by the improvements of medical services. These examples are clearly the upside to technology, but everything has a downside at the same time. Certain technologies might degenerate our physical and mental strength or give the potential to cause criminal acts based on information technologies. Even large numbers of lives can be lost by the malicious use of advanced technologies. Moreover our planet is suffering from a side effect of industrial technologies. The balances between the prosperity of human being and environmental conservation should be taken seriously. A variety number of technologies are confronting this issue. The technologies have huge potential for our future as long as they are handled properly. In this chapter, some recent technologies contributing to this are introduced.

2.2 Technologies and Environments

The energy supply security, which is the key to maintaining our desirable living condition, is strongly related to technologies and environments. The more we pursue economic growth, the more energy is required. In fact, countries are desperate to secure the energy to meet their demand. On the other hand, some gas emissions from generating energy have been raising controversial issues. Well known issue in the energy problem is the climate change attributed to mainly carbon dioxide emission (CO_2). Since 1983, anthropogenic greenhouse gas (GHG) emissions, which include CO_2 , methane (CH_4) and nitrous oxide (N_2O), have increased through rapid industrialization accompanied by explosive population and economic growth, and are now higher than ever. Figure 2-1 shows the long term historical temperature anomaly trends in the combination of land and ocean surface with different data sets. Figure 2-2 presents the atmospheric concentrations of the GHG in CO_2 (green), CH_4 (orange) and N_2O (red) evaluated from direct measurements in the atmosphere (lines) and from ice core data (dots). By comparison between Figure 2-1 and Figure 2-2, human influence on the climate system is clear, and recent climate changes have also had widespread impacts on human and natural systems.

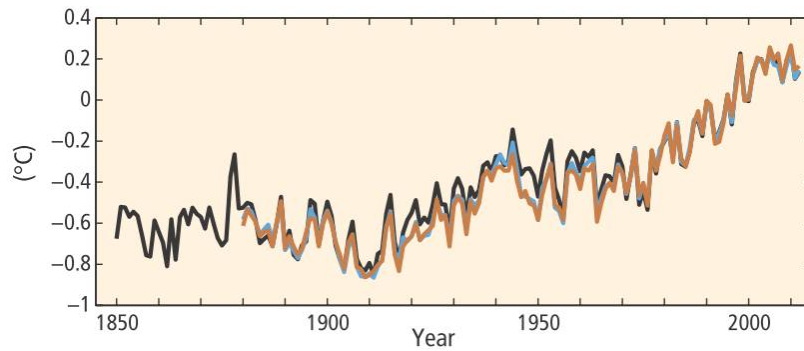


Figure 2-1 Temperature anomaly trends in the combination of land and ocean surface (Colors indicate different data sets).¹

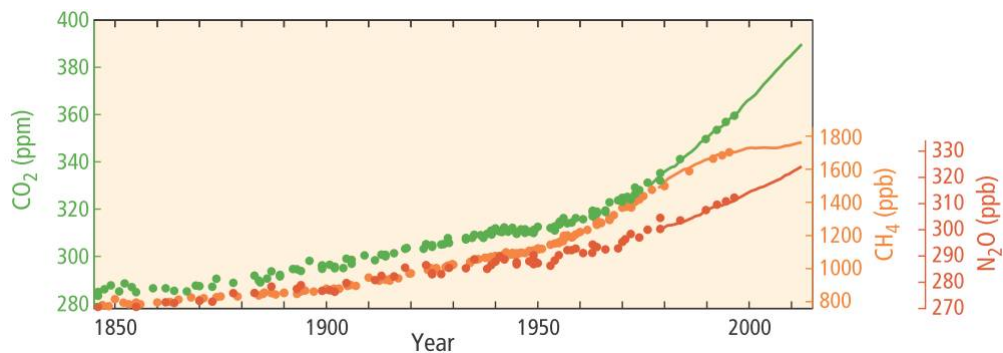


Figure 2-2 Atmospheric concentrations of greenhouse gases.¹

The International Energy Agency (IEA) has described three possible scenarios for energy futures, outlining the measures required for limiting global temperature increase to certain levels and their impacts:^{2,3}

- * 6DS (6°C Scenario): the scenario potentially resulting in devastating future, which the world is now on track.
- * 4DS (4°C Scenario): the scenario, which still has drastic climate impacts ahead, requiring significant improvements in cutting emissions and boosting energy efficiency.
- * 2DS (2°C Scenario): the scenario, which is the main focus of IEA with a vision of a sustainable energy system, requiring reduced GHG emissions.

We have been desperate to meet 2DS, which requires reducing CO₂ emissions by both saving energy in electricity consumption and generating electricity in an efficient way, so called clean energy. One of the famous technologies for saving energy is SSL, and typical clean energy technologies are wind power generation, nuclear power generation, photovoltaic power generation, and so on. Energy storage should be combined with some of those technologies in order to enable the stable supply of electricity.

In March 2015, interesting news came out entitled “Global energy-related emissions of carbon dioxide stalled in 2014”.⁴ According to the special report from IEA, there was a “decoupling” of economic growth and CO₂ emissions in 2014. In other words: the world economy grew, but CO₂ emissions did not. This was “The first time in 40 years in which there was a halt or reduction in emissions of the GHG that was not tied to an economic downturn.” This may indicate that the contribution of technology started to work for reducing CO₂ emissions utilizing clean energy. Striking a balance between reducing CO₂ emissions and economic growth is really important for the reduction of CO₂ emissions as a global action all together. Although developed and developing countries had been taking different positions in consideration of their economic expansions, the data encourages us to reduce CO₂ emissions based on new technologies maintaining their economic growth. It should, however, be noted that the world is still in the difficult situation to achieve 2DS.

IEA proposed the strategy to be taken to catch up with the 2DS, taking immediate actions with ready technologies against long-term impacts and investing in decarbonizing technologies for power generation. Accelerating short-term action is critical to keep the global temperature rise within the range of 2DS. Immediate actions before 2020 are essential to accomplish their post-2020 mitigation targets more easily. While investment and innovative actions may not significantly have an impact on short-term emissions, they are necessary for long-term decarbonization. Primary short-term action can be improvement of energy efficiency, which provides half of the projected energy savings, including lighting and heating/cooling in buildings. SSL based on white LED can significantly contribute to this. As a low carbon technology, power generation is a key factor since electricity generates 25 % of all global GHG emissions. Annual emission from electricity generation could increase to nearly 18 gigatonnes (Gt) by 2030, while in the 2DS they decrease to 8 Gt, 53 % lower.⁵ Reduced demand and cleaner supply could make electricity the largest contributor to emissions savings, in which technologies, solar, wind, nuclear power generation can be considered. Carbon capture and storage (CCS) is also important, as long as fossil fuels are a significant contributor to future energy supply. Energy storage technology needs to be developed in combination with other energy technologies. The recent technology situations for the electricity generation are introduced as follows.

2.2.1 Solar power generation (Photovoltaic power generation)

Since 2010, the world has increased their solar photovoltaic (PV) capacity more than in the previous four decades, led by a few European countries, such as Germany and Italy (Figure 2-3). In 2013, having installed new systems with 100 megawatts (MW) capacity per day, total global capacity exceeded 150 gigawatts (GW) in early 2014. China had the largest capacity followed by Japan and the United States. The share of PV in global electricity is expected to reach 16 % by 2050, which is a notable increase from the target of 11 % in the 2010 roadmap. PV generation would account for 20 % of all renewable electricity. China is predicted to keep leading the global market, contributing about 37 % of global capacity by 2050. It has potential to avoid CO₂ emissions of up to 4 Gt annually, dominating about one third of the total cut target by 2050 from electricity generation.

Commercial silicon modules had an average conversion efficiency of about 16 % in 2013, which has been improved by 0.3 % every year in the last ten years. Modules normally have a lifetime of 25 years at a minimum output rate of 80 % against initial point.⁶ Solar power generation will be a key player for the clean energy.

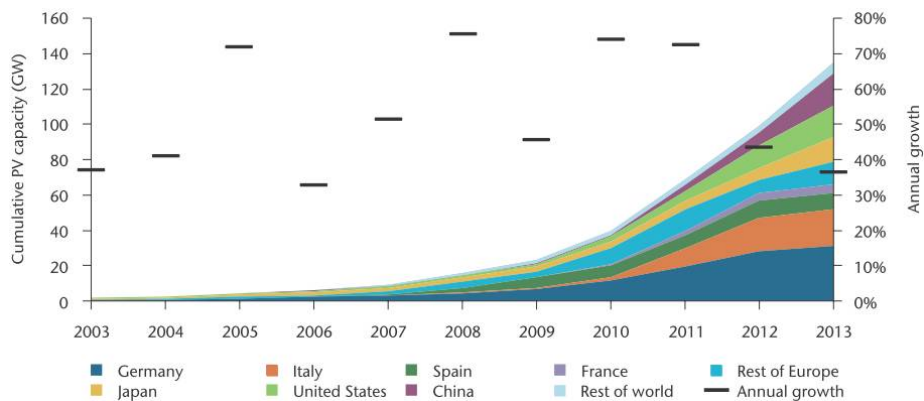


Figure 2-3 Global cumulative growth of PV capacity.⁶

2.2.2 Wind power generation

The cumulative installed capacities of wind power generation are about 300 GW in 2012, which has doubled from 2008. The 75 GW capacity of China is top followed by 60 GW of the United States and 31 GW of Germany (Figure 2-4). Wind power accounts for 2.5 % of global electricity demand. European countries are positively installing wind power generation, providing 30 % electricity of all demand in Denmark, followed by 20 % of Portugal and 18 % of Spain. The IEA 2013 roadmap sets out 15 % to 18 % share in the global electricity from wind power by 2050, which corresponds to 2300 GW to 2800 GW of installed wind power capacity. The design trend of wind turbine has been increasing the height of the tower and the length of the blades, raising the capacity factor, which measures how efficiently the wind turbine generates electricity for the same wind speeds. These designs with higher capacity factor enable the installation of wind turbines in lower speed wind areas, which often allows wind generation sites to get closer to the consumption centers.⁷ Wind power generation will also play an important role as well as solar power generation since these power generation technologies have their own suitable areas to be deployed depending on the climate conditions in each area.

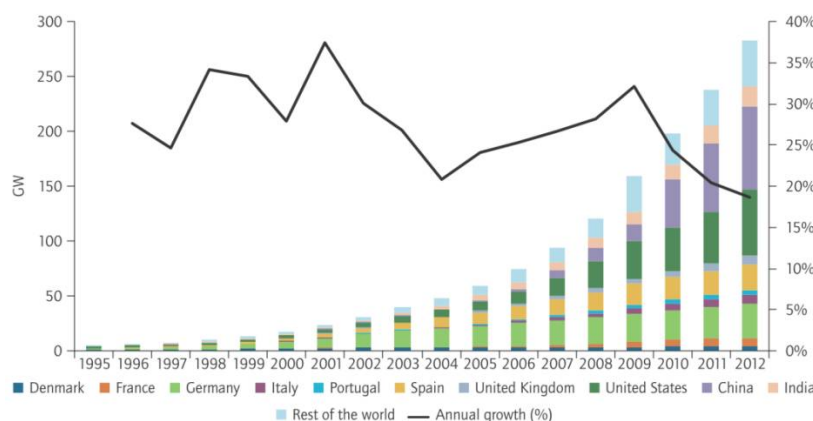


Figure 2-4 Global cumulative growth of wind power capacity.⁷

2.2.3 Nuclear power generation

Nuclear power makes up the largest part of low-carbon electricity in Organization for Economic Co-operation and Development (OECD) countries, accounting for 18 % in electricity production share in 2013. It will keep playing an important role in lowering global GHG emissions from the power generation sector. The global installed capacity of nuclear power is currently 396 GW. To follow the 2DS, it would need to surpass more than double: up to 930 GW by 2050, taking up 17 % of global electricity generation. The Fukushima Daiichi nuclear power plant accident gave a huge impact to public acceptance of nuclear power. Although the accident caused no direct radiation-related casualties, it gave rise to a lot of concerns about the safety of nuclear power plants, especially in Japan. This clearly influenced short term outlook, however, when it comes to the medium to long term, the perspective on nuclear energy remains positive. At the beginning of 2014, there were 72 reactors under construction all over the world, which is the highest in the last 25 years. China will increase capacity most, from 17 GW in 2014 to 250 GW in 2050, representing 27 % of global nuclear capacity. Some developing countries are taking similar positions, including India, the Middle East and the Russian Federation. Most OECD countries will decrease or maintain the current capacity.⁸ Nuclear power plant might be useful for a short term to cut CO₂ emission, but the cost effectiveness of nuclear power generation should be well evaluated considering the cost of gas or renewables since it can be undermined by market conditions.

2.2.4 Carbon capture and storage (CCS)

CCS is comprised of three components with CO₂ capture, transport and storage. All of them are now at commercial scale. Captured CO₂, which is transported to deep underground and stored there, can be utilized for enhanced oil recovery (EOR). 13 large-scale CCS projects were under operation across the world at the end of 2014, and its capacity comes to 26 million tonnes of CO₂ (MtCO₂) per year. The increase of the projects under construction has been slow but steady in the past five years. The United States heads the installation of facilities for CO₂ capture, due to mainly the demand of CO₂ for EOR. The United States holds 7 of 13 operating projects

and 7 of 22 projects under construction or development. The total amount of captured CO₂ by 13 large-scale projects in 2014 accounts for 26 MtCO₂, however it is based on the capacity, and only 5.6 MtCO₂ were monitored and verified since only 5 projects are under operation with monitor to demonstrate CCS performance. The captured CO₂ in eight projects are used for EOR without monitoring the storage performance. There are a total of 35 projects including those currently in operation, in construction or in advanced planning, in which the total potential capture capacity of 63 MtCO₂ per year are expected by 2025. Figure 2-5 shows the total projected capture capacity of large scale CO₂ capture projects. Although CCS is steadily making progress, it is behind the requirement to follow 2DS.⁹

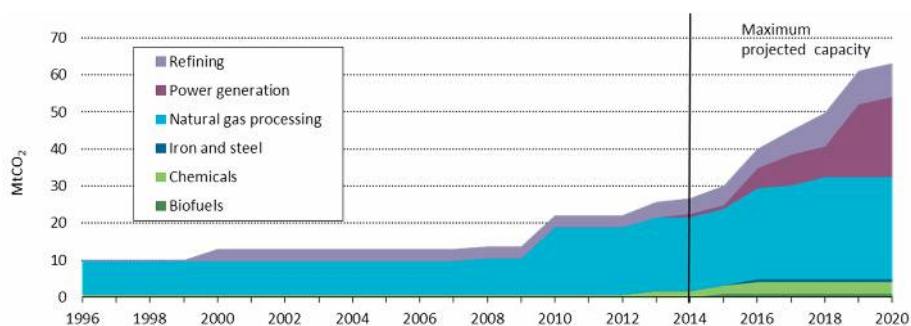


Figure 2-5 Large-scale CO₂ capture projects.¹⁰

2.3 Lighting

2.3.1 A short history of lighting

SSL is one of the technologies for short term reduction of GHG emissions by saving energy consumptions, and is, however, only a recent technology. We have little chance to talk about lighting regardless of receiving huge benefits from it. Harnessing light is one of the privileges of mankind. Light has drastically been changing our lives. In this section, a brief history on the technology of lighting is presented to show how we witnessed the invention of light as summarized by some authors.^{11,12}

Up to the nineteenth century, the only source of an artificial light had been flames produced by the combustion of materials. We could also utilize the flame to cook meals, generate heat and protect ourselves from animal attacks. The light produced within a flame, known as pyroluminescence, mainly occurs due to the incandescence of solids and the recombination of ions into molecules. The first artificial light source was achieved by controlling fires some 500,000 years ago, which were widely used as torches. We were however unable to sustain the flame for a longer period since the torches were burning out themselves. By separating the functions into burning and storing of the flammable items, we could create sustainable lighting.

The oil lamps based on pyroluminescence were invented about 70,000 years ago as a next generation of lighting

and were made out of convenient nonflammable objects such as shells and hollow rocks with wicks dipped in molten fat. Through a lot of improvements, kerosene lamps were finally introduced in the 1850s as widely accessible lighting devices. The introduction of kerosene lamps had a huge impact on changing the after-dark activities of civilized man. The feature of the oil lamp was independent as an isolated device. They are still widely used in Africa and South Asia where electricity is unavailable. On the other hand, it takes a lot of work to fill up the lamp with oil for each street light. This could pose a problem since it requires a lot of labor. The gas lighting system superseded the oil lamp system solving this issue.

Gas lighting was introduced in 1772. William Murdoch of Scotland had started the experiment based on various types of gas, conclusively found out coal gas was the most effective. By the beginning of 20th century, most of the cities in Europe and North America had streets illuminated by gas lamps. The invention of a gas supply system was also inevitable for its success. It reduced the labor required to fill up the lamps with oil on the streets. Gas lighting brought us variation in the shape, size and area of the flame without having a burning core. Now, gas lamps can be seen at places creating historical authenticity. Modern gas lamps are now used for camping. It is well known that Edison followed this gas delivery system when he distributed his electric incandescent lamps in the city. The risk of explosion and unpleasant smell of gas lighting were removed by the appearance of an electric lighting system.

The basic principles of electric lighting were discovered by Sir Humphry Davy of England, at the very beginning of the nineteenth century. He demonstrated arc discharge, which occurs between two carbon rods, and incandescence, which is the glow of a piece of platinum wire being heated by an electric current. When a large electrical potential difference occurs between two conductors spaced very slightly apart, a spark can occur as electrons spontaneously flow from one conductor to the other, producing a bright flash of light, known as arc discharge. The first practical carbon-arc lamp was fabricated by Paul Jablockhoff in 1876 based on this mechanism. Carbon-arc lamps were widely used in street lights until the second decade of the twentieth century.

The evolution of the incandescent light bulb started with the experiment that Sir Humphry Davy performed at the Royal Institution in London in 1802 and a lot of researchers had devoted their time to achieve a bright incandescent lamp with a long lifetime. Joseph Wilson Swan of England and Thomas Alva Edison of the United States, who each worked independently at the early stage, were the most successful inventors of the incandescent lamp. However Edison is the most famous inventor of incandescent lamp since he succeeded in creating the first reliable light bulbs by hiring lots of talented engineers and having managed the world's most famous invention factory. Swan had his experiment in the 1850s and 60s with carbon filaments. He however failed in his early test having difficulties in removing enough air from the lamps. Early in 1879, Swan first demonstrated his incandescent lamp in a lecture in Newcastle. Edison founded the Edison Electric Light Company in 1878,¹³ and demonstrated his lamp at the end of 1879 having obtained a patent for a filament lamp.¹⁴ His lamp contained the major elements seen in Swan's which has platinum lead wires and a carbon filament in an enclosed glass bulb after the removal of some air. Swan was granted the patent for the methods of

evacuation, which prevented the glass seals from fracturing,¹⁵ and started the Swan Electric Light Company in 1881. Since then, the invention of the incandescent filament lamp had been accompanied by famous patent trials including Swan's and Edison's. As both businesses expanded, it had become increasingly difficult for either company to produce a complete lamp. In 1883, they established the joint company named Edison & Swan United Electric Light Company, known commonly as "Ediswan".¹⁶

The colors of the light in their electric filament lamps were yellowish rather than white. To make the filament incandescent lamp white and brighter, a filament must be stable at higher temperature. Carbon has the highest melting point of any element at 3370 °C in a graphite phase and 3550 °C in a diamond phase. However it evaporates at around 1800 °C under vacuum. Metal filaments of osmium and tantalum with higher melting points had been tested and finally tungsten was introduced by Alexander Just and Franz Hanaman of Austria as a stable filament at higher temperature.¹⁷ Yet they are known as non-ductile filaments due to a sintering process: squeezing materials into a dense mass.¹⁸ William D. Coolidge of the United States came up with the idea of a bendable or ductile filament wire, in which the size of grains and impurities were controlled and then processed by drawing heated and sintered tungsten through smaller dies.¹⁹ Even a metal tungsten filament evaporates over 2500 °C under vacuum. Irving Langmuir of the United States, in 1913, found a way to slow down the evaporation of tungsten filaments by filling a lamp with nitrogen gas. He also found that thin filaments radiated heat faster than thick ones, and coiled tungsten wire could maintain the high temperature.²⁰ In 1959, Edward Zubler and Frederick Mosby, added iodine to an argon atmosphere and prevented evaporated tungsten gas from depositing on the inner wall of the lamp, resulting to the so called "tungsten halogen lamps". Their lamp showed practically 100 % lumen maintenance, about 20 % better efficiency than conventional incandescent lamps and an outstanding increase in its lifetime based on the reaction, known as the "halogen cycle".²¹ Thus, the design of the bright white incandescent lamp was established. Although tungsten halogen lamps were widely used replacing the oil lamps and the gas lamps, the worst problem was low energy efficiency. About 90 % of energy is turned into heat and infrared light.

In 1938, GE and Westinghouse Electric Corporation released new colored and white lamps utilizing a low pressure mercury discharge and a light conversion component, which are coated inside the wall of a glass tube by fluorescent powders. This fluorescent lamp is based on the photoluminescence of the phosphor excited by ultraviolet light from mercury. The contribution of phosphors to lighting had begun. Calcium halophosphate activated with trivalent antimony and divalent manganese phosphors, $\text{Ca}_5(\text{PO}_4)_3(\text{F},\text{Cl}):\text{Sb}^{3+},\text{Mn}^{2+}$ were invented by Alfred Mckeag of England, in 1942.²² These were distributed widely as a true white fluorescent lamp thereafter. Fluorescent tubes had been the most efficient way to generate white light for general lighting applications.

The contemporary revolution of lighting started in 1991 by the invention of LEDs based on InGaN semiconductor which was achieved by Nakamura and young engineers of Nichia Corporation.²³ It led to the concept of white LEDs comprised of blue LEDs and color converting phosphors.²⁴ They were first

commercialized in 1996. The explosive development of SSL based on highly bright visible LEDs is today overwhelming the lighting market worldwide.

2.3.2 Global LED lighting market

The recent LED market trend was summarized in detail by the U.S. Department of Energy (DOE) and European Commission.^{25,26} According to a recent DOE report, the total electricity use in the United States for lighting accounted for approximately 18 % of total usage in 2010. IHS estimated that LED products dominated 18 % of lighting revenues all over the world in 2013, corresponding to revenues of \$16 billion. Strategies Unlimited estimated that the market penetration of LED lighting reached about 3 % by the global sales of 400 million LED lamps in 2013. From 2012 to 2014, installations of LEDs have increased to 2.8 % for indoor applications and to 10.1 % for outdoor applications, while total LED penetration increased to 3.0 %.²⁷ As seen in the report from the major lighting manufactures, the trend is shifting clearly from conventional lighting to LED lighting. The largest global lighting company, Philips, reported that in the fourth quarter of 2014, revenues from LED-based lighting increased by 48 % in 2012 and by 20 % in 2013 and represents 37 % of all their lighting sales.^{28,29} Another giant lighting company, OSRAM, in Germany has also reported similar results in the first quarter of 2014. Quarterly revenue for LED-based lighting products increased by 28 % comparing with the prior year, which results in 33 % of OSRAM's total revenue from 26 % in the prior year quarter.³⁰ As indicated in Figure 2-6, shipments of LED-based lamps and luminaires are expected to increase steadily until 2021, dominating about half of total lighting shipments. An eventual decline in sales of LED light can be assumed by the longer period of the replacement cycle since one advantage of LED technology is longer operation life. However it has a huge market potential including off-grid countries mainly in Asia and Africa. Taking a closer look at the situation by sectors, the LED market is pushed forward by different drivers such as Residential, Commercial, Industrial and Outdoor. European countries favor residential and commercial lighting. Asian countries (China, India, etc.) favor Outdoor lighting represented by LED streetlights. Japan favors replacement market of lamps, tube lights, and ceiling lights in any sectors. Country-by-country situation is now described as follows:

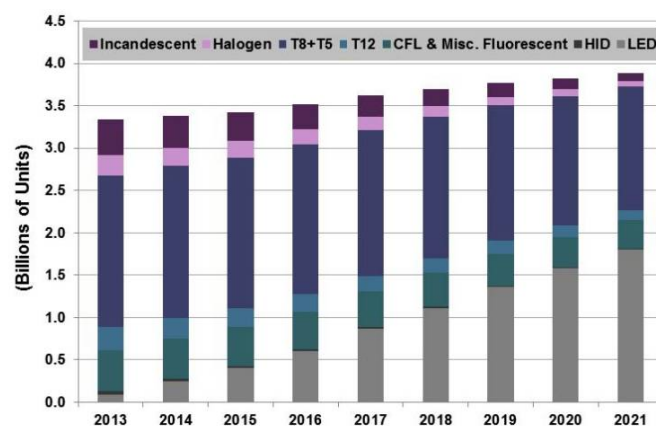


Figure 2-6 Global forecasted shipments of LED lamps and luminaires, 2013-2021.²⁵

The United States

Figure 2-7 presents the lighting energy consumption forecast by sectors. LED lighting is projected to cut energy consumption in lighting by 15 % in 2020 and 40 % in 2030.³¹ LEDs are particularly well suited to street and roadway lighting applications since they are directional light sources with high durability and long lifetimes. With these advantages, many local governments have promoted projects to replace their lighting in these applications to LEDs. The Bureau of Street Lighting, the City of Los Angeles has already completed a four-year-project, which replaced citywide conventional street lighting with more than 140,000 LED streetlights. It has reduced energy usage by 63.3 %.³² The lighting market model expects that LED applications in the street and roadway will expand most rapidly. Figure 2-8 shows the market share forecast in sales of street and roadway section from 2013 to 2030. By the end of 2013, the share in that section is about 14 %, then it will increase up to 83 % by 2020 and reach nearly 100 % by 2030 replacing the metal halide and high pressure sodium (HPS) shares, which account for 28 % of electricity saving. LED lighting is already popular area in the street and roadway market.

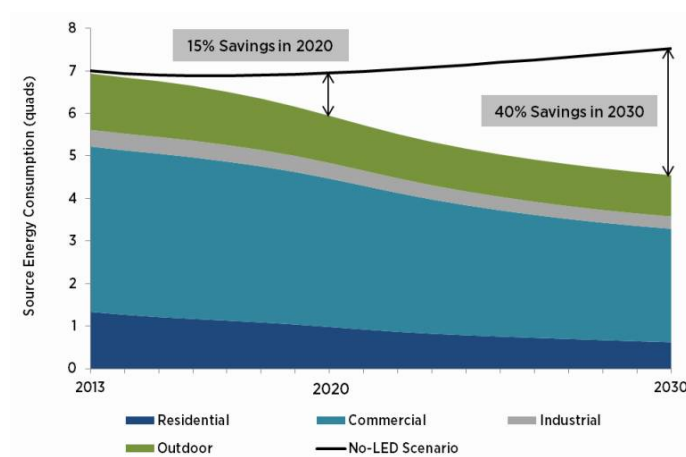


Figure 2-7 Total Energy Consumption Forecast of lighting sector in the United States, 2013 to 2030.³¹

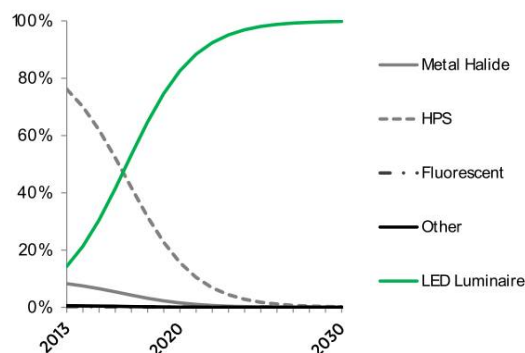


Figure 2-8 Market Share Forecast in Street and Roadway (% of lm-hr sales), 2013 to 2030.³¹

Europe

The share of value-based European LED market is estimated at around 9 % in 2012. However, it is projected to increase to over 45 % by 2016 and more than 70 % by 2020. Although, the shift to LED light in Europe is slower than other regions, it will be accelerated by the government policy of nuclear phase out in Germany and the upcoming regulation on the ban of low-voltage halogen lamps by European Commission.²⁶ The faster penetration of LED will be strongly supported by the price drop of LED and the improvement of LED efficacy. Figure 2-9 shows the projected sales of LED lamps in Europe. The sales of LED lamps were slow from 2008 to 2009, but rapid growth is expected from € 0.3 billion in 2010 up to € 1.9 billion in 2015.³³

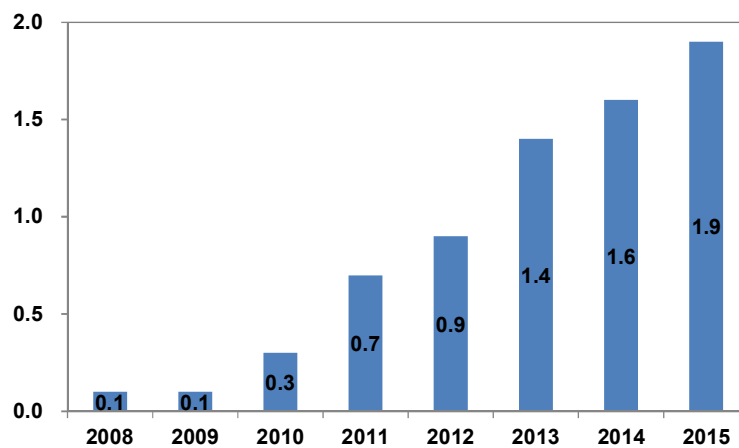


Figure 2-9 Projected sales of LED lamps in Europe (€ billion).³³

Asia

Japan has been a driving force for the penetration of LED lighting products, and been leading the globe with an estimated LED adoption rate of 15 % in 2012 and 19 % in 2013.²⁵ The demand of LED lamps was higher than expected in 2012, largely due to the increased awareness of energy-saving after the Tohoku earthquake disaster in 2011, picking up the prior demand. The Korean government hammered out the “Low Carbon, Green Growth” strategy in 2009 and SSL plays an important part of the plan, pursuing 30 % replacement of LED lamps in public facilities.²⁶ The market penetration of LED lamps in China was just 0.6 % in 2010 but has been growing rapidly and reached up to 8.9 % in 2013 (Figure 2-10). Chinese government has been shifting its support from providing funds for investment in capital equipment to providing subsidies for the purchase of lamps and luminaires.²⁵ China is mainly targeting the street lighting sector and will invest 1.6 billion RMB into it. Subsidies by the government will account for 30 %-50 % of the product prices. The penetration of Indian LED products is currently 4 % and will grow to 35 % in 2018. The government has also been driving initiatives in the distribution of LED lighting combined with solar panels in villages to promote energy-efficient lighting so called solar lanterns.²⁶

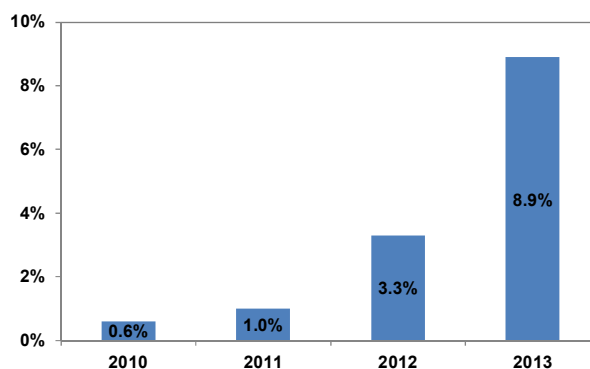


Figure 2-10 Penetration of LED Lighting market in China, 2010-2013.²⁵

2.3.3 Opportunity for access to lighting

Technologies are not just for advanced countries. There is a huge potential for technologies to achieve more rapid social and economic development in developing countries. In this section, the potential contribution of LED lighting is introduced. According to Energy access database from IEA,³⁴ world electrification rate in 2014 is 82 %, which means one out of five people lives without electricity. In particular, the electrification rate of Africa is only 43 %, which is dominated by the rate of 32 % in Sub-Saharan Africa. More than 620 million people live in the area without access to electricity in Sub-Saharan Africa. As seen in a change from 2009 to 2030, Latin America and South Asia will decrease their un-electrified population from 34 million to 13 million and from 809 million to 561 million, respectively. On the other hand, Africa increases it from 589 million to 698 million due to a rapid population growth, mostly in rural area. Africa will then have surpassed Asia to become the largest un-electrified area.³⁵

Approximately more than 290 million people in un-electrified areas employ the use of kerosene lamps as their primary light source.³⁶ A survey, which was reported in 2012 by the Lawrence Berkeley National Laboratory of California's Lumina Project covering the users of kerosene lighting across five Sub-Saharan Africa countries, showed that around a quarter of the sampled population have health and safety concerns related to kerosene lighting. The by-products of kerosene combustion are correlated with higher incidences of diseases like tuberculosis and cataract conditions. According to reports in most hospital studies, unintentional kerosene ingestion is the principal cause of child poisoning in developed countries, which can be related to 7 % of mortality rate.³⁷ In addition to toxic fumes from kerosene combustion, the chance of hazardous fires and ensuing risk of burns on life and property is substantial. As a key to solve these problems, solar portable lights (SPL)s have been introduced covering a range of lighting needs from individual tasks to general household lighting. SPLs are referred to as "pico-solar" or "solar lanterns". The majority of devices are based on LEDs,

equipped with rechargeable batteries and solar panel. Installing SPLs has significant impact on many aspects of life such as environment, business, education and household spending. The barrier for SPL installation is quite low. It needs no utility for the electric power transmission since the power is supplied by solar panel directly or via batteries. The benefits of SPLs are listed below.³⁶

Environment: The total consumption of kerosene in households and in commerce worldwide is 440 million barrels of oil per year with emissions of CO₂ up to 190 million tons into the air annually, which is equivalent to the exhaust gas from 30 million cars. An enormous amount of CO₂ emissions can be reduced by adopting SPLs.

Business: For many rural households, acquiring fuel for lighting can be time-consuming owing to traveling long distances often undertaken by women and children, taking up their available time for productive activities. They can save their time by installing SPLs. Solar lanterns can provide extra business opportunities by allowing more time to work at night. The positive correlation has been seen between the quality of the lighting in commercial enterprises and retail sales. The move from kerosene to LED based lighting that improves the quality of illumination also boosts sales, attracting more attention of customers to the display.

Education: Having introduced SPLs, children can stay up longer each day and use their additional time for studying and reading, which lengthen average study hours of children. The better quality of illumination helps to study a lot.

Household spending: In Africa, the cost for fuel-based lighting is substantial. According to Lighting Africa research, Base of Pyramid African households, which mean households with less than \$3000 annual income, face recurring expenditures on fuels, which dominates in their monthly household budgets up to 10 to 25 %. They can save this cost by utilizing SPLs.

2.4 Assessment Parameters for white LEDs

The potential of SSL is directly related to the performance of white LEDs, and the parameters used to describe a white LED need to be understood. There are five primary parameters in radiometry, photometry and colorimetry.

2.4.1 Efficiency (external quantum efficiency)

The efficiency of LEDs is a dimensionless quantity usually expressed in a percentage. It is a radiant power output of a LED divided by an electrical power input. The spectral response function of the human eye is not considered in this parameter. Driving LEDs at a higher current increases the light output, but results in a commensurate decrease in efficacy, known as efficiency droop. The efficiency of LED is more important for high power LED lights, since the input power of LED is dissipated as heat more at higher operation current. It is directly related to heat management.

2.4.2 Efficacy

The energy efficiency of LED products is normally characterized by efficacy, evaluated in the ratio of electrical power input to light output. Luminous Efficacy is the most important parameter for white LEDs, which is described in emitted flux (lumens) divided by power draw (watts) with the units of lumen per Watt (lm/W). The lumen is a unit of light intensity perceived by the human eye, which is weighted by its visual perception. It should be noted that the efficacy of individual LED packages is different from the efficacy of an LED luminaire or an integrated LED lamp, being stemmed from driver, thermal and optical losses. When you compare the values, it is also important to consider the differences in the procedures and conditions used for the measurement, and whether commercially available lighting products or the laboratory samples. The DOE has set the target for LED package efficacy of 266 lm/W and LED luminaire efficacy to surpass 200 lm/W in their Multi Year Program Plan.³⁸ Figure 2-11 shows a basic comparison of the efficacy for several major types of lamp product as of January 2013. The efficacy of current LED products is in the same range as fluorescent and HID products and importantly LED is the only type of product showing the potential for substantial improvement in efficacy in the near future.³⁹

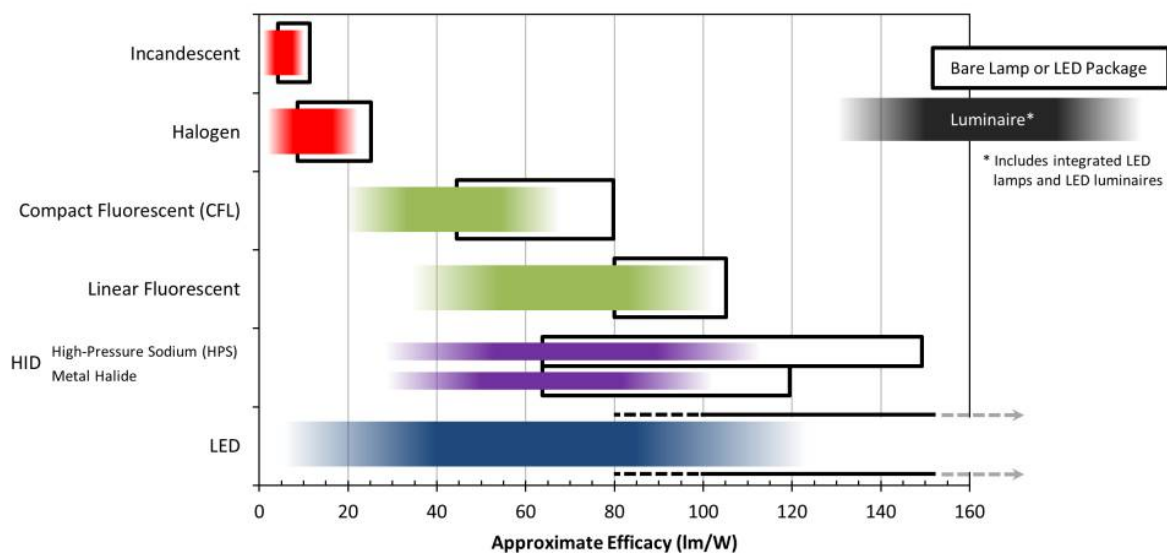


Figure 2-11 Approximate range of efficacy for various common light sources.³⁹

The black boxes show the efficacy of bare conventional lamps or LED packages, which can vary based on construction, materials, wattage, or other factors. The shaded regions show luminaire efficacy, which considers the entire system, including driver, thermal, and optical losses.

2.4.3 Color Coordinates

Color coordinates are measured color locations of the emitted light on the CIE color chromaticity space diagram. The CIE (Commission Internationale de l'Éclairage) is an international organization specializing in the advancement and standardization of lighting knowledge, which is called the International Commission on

Illumination. Many companies and national institutions consider information provided by the CIE for the colorimetric evaluation. In 1931 the CIE established the standard system using X, Y, Z tristimulus functions based on the assumption that every color can be rendered by the combination of the three primary colors, blue, green and red. The color coordinates are specified by the two derived parameters of x and y on the CIE 1931 color chromaticity space diagram, as shown in Figure 2-12. This diagram is widely used for comparing the colors among sources of light as well as the emission from phosphors. The X, Y and Z tristimulus values, which are calculated in the following equations, are obtained by integrating the spectral power distribution of radiation and the three eye response curves $x(\lambda)$, $y(\lambda)$ and $z(\lambda)$ over the wavelength range from 380 nm to 780 nm.⁴⁰

$$X = k \int_{380}^{780} I(\lambda) \bar{x}(\lambda) d\lambda \quad \text{Equation 2-1}$$

$$Y = k \int_{380}^{780} I(\lambda) \bar{y}(\lambda) d\lambda \quad \text{Equation 2-2}$$

$$Z = k \int_{380}^{780} I(\lambda) \bar{z}(\lambda) d\lambda \quad \text{Equation 2-3}$$

The known x, y and z color coordinates are then derived from the tristimulus values.

$$x = \frac{X}{X + Y + Z} \quad \text{Equation 2-4}$$

$$y = \frac{Y}{X + Y + Z} \quad \text{Equation 2-5}$$

$$z = \frac{Z}{X + Y + Z} = 1 - x - y \quad \text{Equation 2-6}$$

Another color space diagram of CIE 1976 UCS (uniform color space) are developed achieving perceptual uniformity, which has an equal distance in the color space corresponding to equal differences in color. Figure 2-13 shows the CIE 1976 UCS diagram. On this diagram the color coordinates are specified by the two derived parameters of u' and v' , which can be calculated by transformation of the X, Y and Z values.

$$u' = \frac{4X}{X + 15Y + 3Z} \quad \text{Equation 2-7}$$

$$v' = \frac{9X}{X + 15Y + 3Z} \quad \text{Equation 2-8}$$

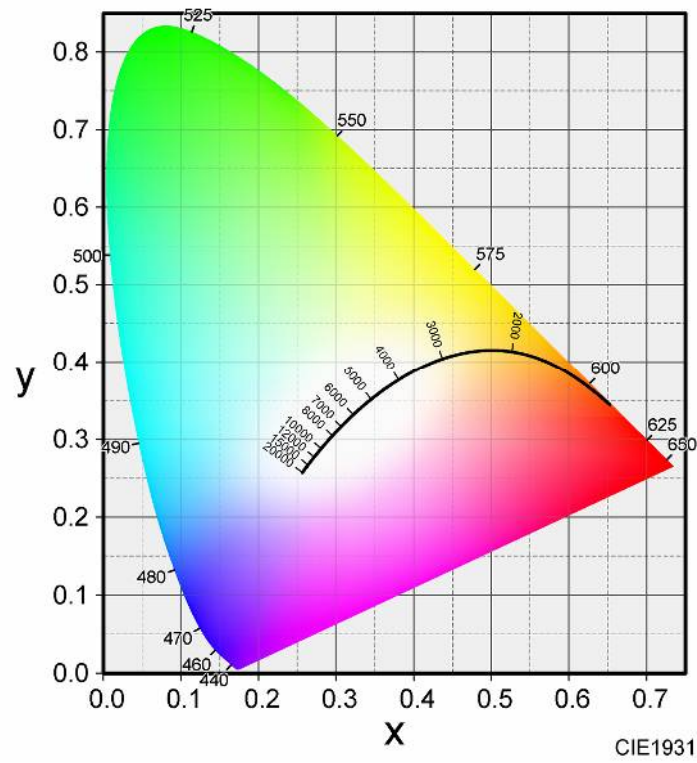


Figure 2-12 CIE 1931 diagram.

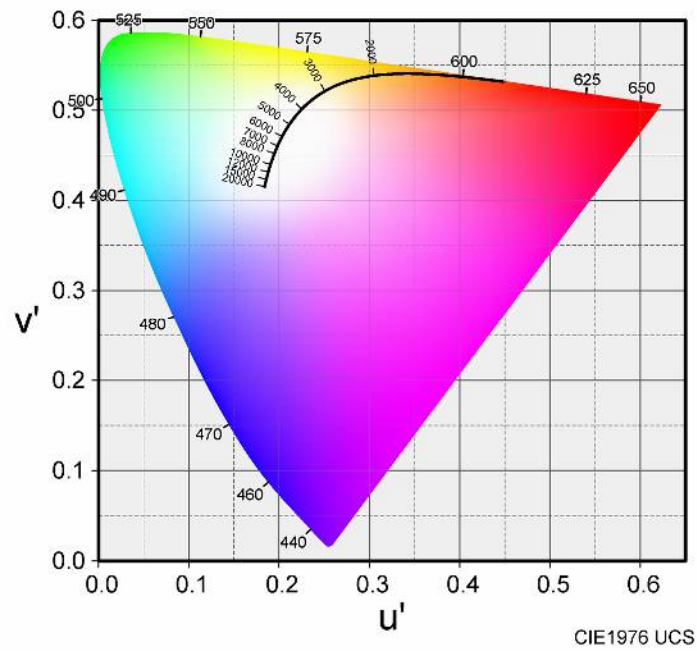


Figure 2-13 CIE 1976 UCS diagram.

2.4.4 Correlated Color Temperature (CCT)

Color temperature is an important aspect for color appearance to relate temperatures to colors, for example how “cool” (bluish) or how “warm” (yellowish) nominally white light appears. Correlated Color Temperature (CCT) is a metric relating to the appearance of a theoretical blackbody, which turns red, orange, yellow, white, and finally blue with increasing its temperature. The CCT, given in Kelvin (K), is defined by the chromaticity position along the Planckian locus (blackbody) of the CIE chromaticity diagram and can be calculated at Planckian temperature that provides the smallest chromaticity difference between the test chromaticity and the Planckian locus on UCS diagram. It characterizes the color of the emitted light, not the color of illuminated objects. As shown in Figure 2-12 (CIE 1931) and Figure 2-13 (CIE 1976 UCS), the Planckian locus is indicated as the black line with various blackbody temperatures.³⁹

2.4.5 Color Rendering Index (CRI)

The CRI describes the ability of a light source to render the colors of objects accurately when they are compared to the reference light source. The CRI is calculated in accordance with the Test-Color Method (CIE 13.3-1995), by measuring the difference between the lamp in question and the reference lamp in terms of how they render the test color samples (TCS). For each color sample, the chromaticity can be compared between under a given light source and under a reference source of equal CCT, enabling measurement of the color difference that is then mathematically adjusted and subtracted from 100 (R_i). The principal metric of the CIE system is the CRI, which is the average of the eight R_i scores (R_1 to R_8) from the standard test colors of TCS01 to TCS08. A score of 100 indicates that the source renders the colors identically to the references. The special color rendering indices, referred to as R_9 through R_{14} , are each based on a single test color (TCS09 to TCS14). They are not considered for the calculation of CRI, but can be used for supplemental analysis. R_9 can be especially useful as an index for strong red color since the rendition of saturated red is particularly important for the appearance of skin tones, among other objects. Color samples for CRI (TCS01-TCS08) and for R_9 - R_{14} (TCS09-TCS14) are shown in Figure 2-14. It is worth noting that when the lamp in question has a CCT of less than 5000 K, a blackbody radiator is used as a reference source and a spectrum of daylight is used for higher CCT sources. By and large, a light source for interior applications with a CRI in the 70s would be considered as acceptable, the 80s as good and the 90s as excellent.³⁹ In general, the higher CRI value lowers the possible luminous efficacy, since the human visual response curve has its peak wavelength at 555 nm. To render objects well, a light source must include light that spans a wider wavelength spectrum, but that the human eye is less sensitive. It should be added that, in CIE Technical Report 177:2007, they concluded that a long-term research and development process of color quality metric is underway. CRI should be considered as one data point in evaluating white LED products, and be noted that CRI cannot predict the visual ranking of a set of lighting products when white LED sources (either PC or RGB) are included. In fact, many RGB-based LED products have CRIs in the 20s, yet the light appears to render colors well.⁴¹

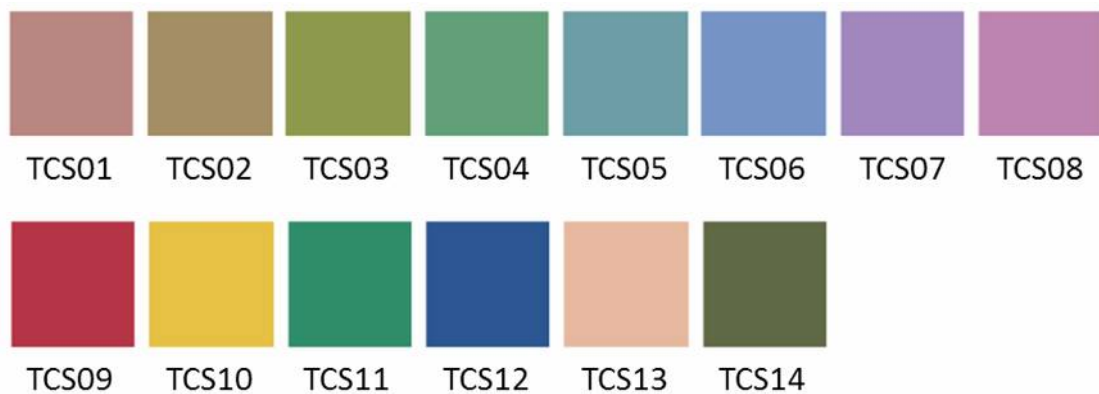


Figure 2-14 Color samples for CRI (TCS01-TCS08) and for R9-R14 (TCS09-TCS14).³⁹

2.5 White light-emitting diodes

There are several variations used to produce white light by combining different colors of LED chips and phosphors. Figure 2-15 shows schematic illustrations of four typical white LED configurations with and without phosphors, which are described below. Figure 2-16 shows the emission spectra from different combinations of LED chips and phosphors corresponding to these configurations.

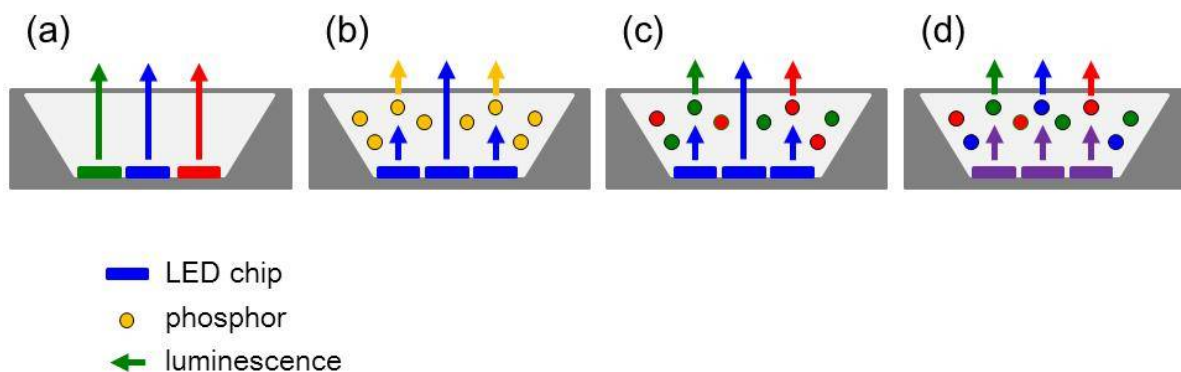


Figure 2-15 Schematic illustrations of various combinations of white LED.

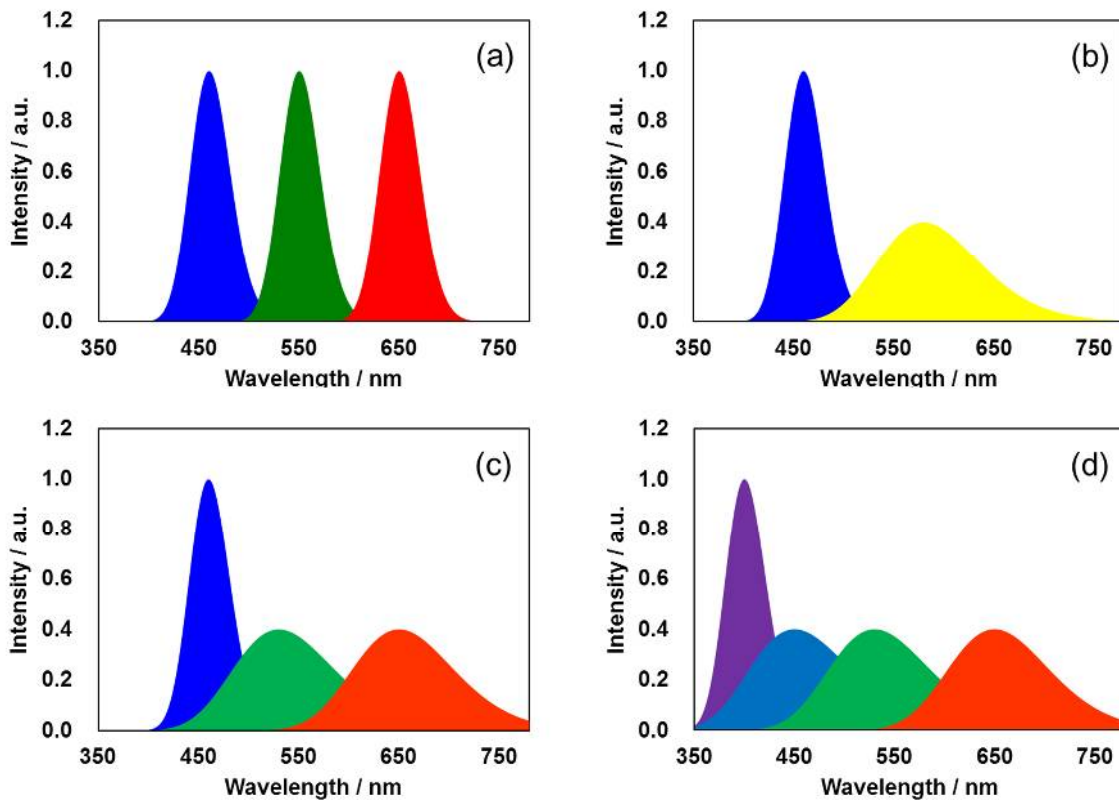


Figure 2-16 Emission spectra image of the white LEDs in the different configurations (Alphabets in the parenthesis correspond to those in Figure 2-15).

- (a) Three LED chips with different colors (red, green and blue) are combined without phosphors, which is called color-mixed LED (cm-LED). This type of device potentially produces higher luminous efficacy, avoiding the loss in luminous flux outside the visible spectrum owing to a sharp emission band with narrower and higher emission peak from each LED chip, and the loss in Stokes Shift unlike phosphor converted LED (pc-LED). Figure 2-17 shows the projected LED package efficacy of pc-LED and cm-LED for warm colors and cool colors, respectively. The key to achieving higher luminous efficacy with this architecture is the improvement of quantum efficiency in green chips, because there is no efficient green LED chip available. Moreover, it tends to have complicated structures in LED luminaires since combined LED chips with different emission color need to be operated at different voltages, which can lose simplicity in the design of electronic circuits, and also have difficulties in managing the color point of LED light within certain deviations. They can have an impact on the production cost.

- (b) As the simplest and the most conventional configuration in the market, a blue LED chip is combined with a yellow phosphor. The yellow phosphor converts absorbed blue light from the LED chip to yellow light. Only a portion of the light from LED is converted by the phosphor, while the remainder contributes as a mixing component of total white light. The combination of blue light from the LED chip and yellow light from the phosphor generates pseudo-white light. This type of device produces higher luminous efficacy compared with other pc-LED, however, applications are limited due to its poor color quality.
- (c) The combination of blue LED with green and red phosphors is getting more popular for balancing the luminous efficacy and color quality. Green and red phosphors convert absorbed blue light from the LED chip to green and red light, respectively. The combination of blue light from the LED chip, and green and red light from the phosphors generates better quality of white light, extending the potential applications. The variation of green and red phosphors with different emission wavelength and emission band width enables fine tuning of white LEDs in versatile applications.
- (d) For special applications, this configuration offers ultra-high quality color. A near-UV LED chip is combined with blue, green and red phosphors. Each phosphor converts absorbed near-UV light from the LED chip to blue, green and red light, respectively. The very wide emission spectrum, which is contributed by three phosphors, covers a broad range of emission wavelengths and achieves a high value in Ra of the color rendering index. The key to balancing color quality and high luminous efficacy strongly relies on the quantum efficiency of the near-UV LED. It is said that the near-UV LED chip-based white LED has the potential to surpass the LED efficacy of blue LED chip-based white LEDs, overcoming the disadvantages of certain loss in conversion efficiency of three phosphors. However, the deterioration of the organic binder by the UV light can also be a problem to be solved.

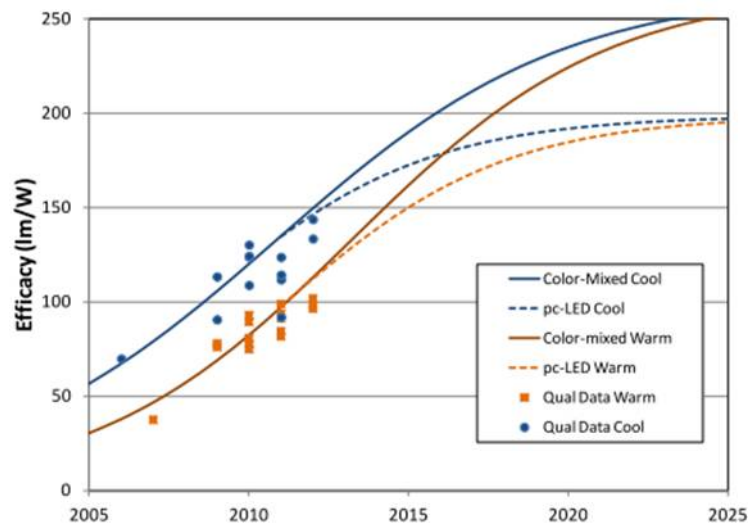


Figure 2-17 Projected LED Package Efficacy (phosphor converted LED and color-mixed LED).⁴²

Photos from Figure 2-18 to Figure 2-21 are adapted from Verbatim-Europe.⁴³ There are varieties of LED bulbs commercially available as shown in Figure 2-18. The basic structure for each bulb is quite common as illustrated in Figure 2-19. The key component of an LED bulb is the LED module, which is comprised of several LED packages (Figure 2-20) fabricated with mainly LED chips, phosphors and silicone paste (Figure 2-21). The phosphors are usually fine grain powders with particle size distributions of over micron-scale having different body color depending on the absorption of light. They are normally used with transparent silicone paste as an encapsulant after mixing.



Figure 2-18 LED based light bulbs.⁴³



Figure 2-19 Schematic illustration of LED light bulb.⁴³



Figure 2-20 LED module comprised of 6 LED packages.⁴³

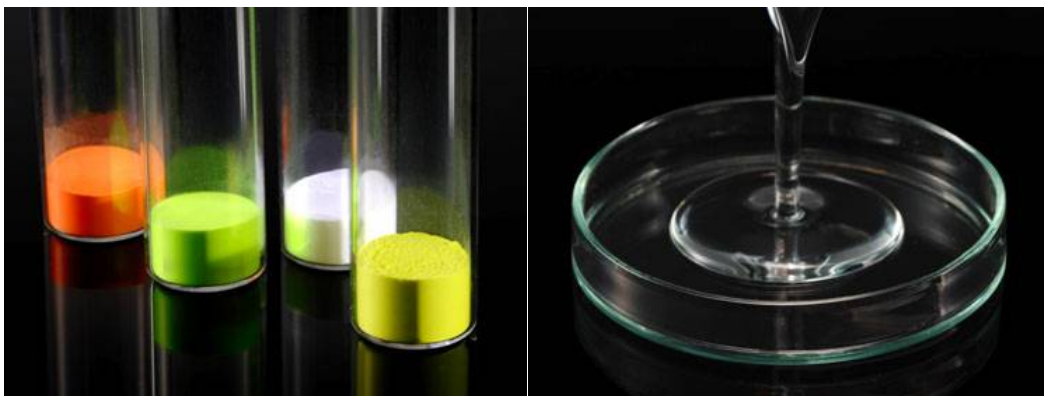


Figure 2-21 Various color of phosphors and silicone paste.⁴³

2.6 References

- 1 IPCC, 2014: Climate Change 2014: Synthesis Report. Contribution of Working Groups I, II and III to the Fifth Assessment Report of the Intergovernmental Panel on Climate Change [Core Writing Team, R.K. Pachauri and L.A. Meyer (eds.)]. IPCC, Geneva, Switzerland, 151 pp.
- 2 Energy Technology Perspectives 2014, International Energy Agency, 2014
- 3 Tracking Clean Energy Progress 2015, International Energy Agency, 2015
- 4 Energy and Climate Change, World Energy Outlook Special Report, International Energy Agency, 2015
- 5 The way forward, International Energy Agency, 2014
- 6 Technology Roadmap, Solar Photovoltaic Energy, International Energy Agency, 2014
- 7 Technology Roadmap, Wind Energy, International Energy Agency, 2013
- 8 Technology Roadmap, Nuclear Energy, International Energy Agency, 2015
- 9 Tracking Clean Energy Progress 2015, International Energy Agency, 2015
- 10 'International Energy Agency (2015), Tracking Clean Energy Progress 2015, OECD/IEA, Paris'
- 11 A. Žukauskas, M.S. Shur and R. Gaska, Introduction to Solid-State Lighting, Wiley Interscience Publication, 2002
- 12 J. Miyahara, 2005, "Innovation of white light" (in Japanese)
- 13 GE HISTORY, 1878-1904, <http://www.ge.com/about-us/history/1878-1904>
- 14 T.A. Edison, U.S. patent No. 223898 of 1879.
- 15 British Patent No.18 and No.250 of 1880.
- 16 Smithsonian, Lamp Inventors 1880-1940, <http://americanhistory.si.edu/lighting/bios/swan.htm>
- 17 A. Just and F. Hanaman, German patent No. 154262 of 1903.
- 18 Non-ductile Tungsten Lamp, http://americanhistory.si.edu/collections/search/object/nmah_1248859
- 19 Lamp Inventors 1880-1940, <http://americanhistory.si.edu/lighting/bios/coolidge.htm>
- 20 Lamp Inventors 1880-1940: Gas-filled, Coiled Tungsten Lamps, <http://americanhistory.si.edu/lighting/bios/langmuir.htm>
- 21 20th Century Inventors: Tungsten Halogen Lamp, <http://americanhistory.si.edu/lighting/bios/thteam.htm>
- 22 S. Kamiya and H. Mizuno, In Phosphor Handbook, W. Yen, S. Shionoya and H. Yamamoto, CRC Press, Boca Raton, 2007, p.452.
- 23 S. Nakamura, *Jpn. J. Appl. Phys.*, 1991, **30**, L1705.
- 24 Y. Shimizu, U.S. patent No.5998925 of 1997.
- 25 Solid-State Lighting Research and Development Multi-Year Program Plan, U.S. Department of Energy, 2014
- 26 2014 Update on the Status of LED market, European Commission, 2014
- 27 Adoption of Light-Emitting Diodes in Common Lighting Applications, U.S. Department of Energy, 2015
- 28 R. Philips, "Q4 2013 Quarterly Report," 28 January 2014.
- 29 R. Philips, "Q4 2014 Quarterly Report," 27 January 2015.
- 30 OSRAM Licht Group, "Interim Report: Q1 FY 2014," 31 December 2013.
- 31 Energy Savings Forecast of Solid-State Lighting in General Illumination Applications, U.S. Department of Energy,

2014

- 32 LED Energy Efficiency program, City of Los Angeles Bureau of Street Lighting, 7 October 2015
- 33 Wolfgang Gregor (ELC Vice-President), “LED Market Overview and Forecast Europe”, TILS Forum Taiwan, March 13, Taipei, 2012
- 34 World Energy Outlook 2014, International Energy Agency, 2015
- 35 Lighting Africa Market Trends Report 2012, Lighting Africa, 2013
- 36 Solar Lighting for the Base of the Pyramid - Overview of an Emerging Market -, Lighting Africa, 2010
- 37 Evan Mills, Health Impacts of Fuel based Lighting, Lawrence Berkeley National Laboratory, University of California, 2012
- 38 Solid-State Lighting Research and Development Multi-Year Program, U.S. Department of Energy, 2012
- 39 Building Technologies Program SOLID-STATE LIGHTING TECHNOLOGY FACT SHEET, U.S. Department of Energy, 2013
- 40 Handbook of LED Metrology Version 1.1, INSTRUMENT SYSTEMS GmbH
- 41 LED Measurement Series: Color Rendering Index and LEDs, U.S. Department of Energy, 2008
- 42 Solid-State Lighting Research and Development Multi-Year Program Plan, U.S. Department of Energy, 2012
- 43 Verbatim-Europe, www.verbatim-europe.co.uk

Chapter 3 Phosphors for white LED applications

3.1 Introduction

Inorganic phosphors are comprised of host materials with a small quantity of dopant ions activating luminescence. Typical dopant ions for phosphors have been rare earths, and either Ce^{3+} or Eu^{2+} are normally used for the LED applications since their absorptions can match LED light in certain environmental conditions of host crystals. Host materials of phosphors have been oxides, fluorides, halides and oxysulfides, while commercially available hosts for SSL have mostly been oxides. However recent trends have shifted towards oxy-nitride or nitride materials, which have advantages in their large red shift and in smaller thermal quenching by the stronger bonding in nitrides. In this chapter, fundamentals of photoluminescence in LED phosphors are explained, which originate from the energy transition between the energy level locations of lanthanide ions in the crystallographic environment of host materials, and characteristics of some phosphors for SSL are described focusing on the practical phosphors with commercial availability.

3.2 Photoluminescence processes in phosphors

The photoluminescence of LED phosphors mostly relies on lanthanide ions. The lanthanides contain 15 elements from La with atomic number 57 to Lu with 71, in which different electronic configurations of $4f$ orbitals determine a variety of luminescence properties. The luminescence from lanthanide ions originate from electric dipole, magnetic dipole and electric quadrupole effects, but that of electric dipole is much stronger than others. Electric dipole $4f-5d$ transitions are parity allowed resulting in strong luminescence, and electric dipole $4f-4f$ transitions are parity forbidden, which however becomes partially allowed by mixing with orbitals of opposite parity. The lifetime of the $4f-5d$ transitions is the order of 10^{-7} to 10^{-8} s because of their parity allowed nature and the $4f-4f$ transitions is the order of 10^{-5} to 10^{-3} s owing to their parity forbidden nature, respectively.¹ Although the $4f-4f$ transitions are generally weak in intensity, they can be strong enough due to the high absorption rate in the excitation process via charge transfer states. $4f-4f$ transitions have contributed to cathode ray excitation and UV excitation applications for decades and $4f-5d$ transitions mainly contribute to SSL applications. The differences between them are explained in the following sections.

3.3 Luminescence from $4f-4f$ transitions

An atomic orbital is described with the three terms of the principal quantum number (n), the orbital quantum number (l) and the magnetic quantum number (m). The number of n determines the size of shell and dominant energy levels. The number of l represents the shape of the atomic orbital and the orbital angular momentum. Lastly, the number of m gives the directional information of an atomic orbital having integrated values between

$+l$ and $-l$. The different types of atomic orbital s , p , d , and f have the l value of 0, 1, 2 and 3, respectively, differentiating the orbital in $2l+1$ ways. The determining orbitals for lanthanide ions are $4f$, which have 7 orbitals in accordance with the orbital quantum number $l=3$, and accommodate 14 electrons considering the spin. The 14 lanthanide ions from Ce^{3+} to Lu^{3+} have one to fourteen $4f$ electrons, respectively, in the inner subshells with the core shell structure of Xe. The $4f$ electrons are well shielded by the outer $5s$ and $5p$ subshells and little affected by the coordination environment, which causes the similarity of lanthanide ions. The ions from Ce^{3+} to Yb^{3+} have certain energy level characteristics owing to partially filled $4f$ orbitals, whereas La^{3+} and Lu^{3+} have no electronic energy levels due to none or fully filled $4f$ orbitals as listed in the Table 3-1.

Table 3-1 Electronic configuration of trivalent lanthanide ions in the ground state.

Ions	Atomic Number	4f electrons							S Σs	L Σl	J $\Sigma(L+S)$	$2S+1L_J$
		3	2	1	0	-1	-2	-3				
La^{3+}	57								0	0	0	1S_0
Ce^{3+}	58	↑							1/2	3	5/2	$^2F_{5/2}$
Pr^{3+}	59	↑	↑						1	5	4	3H_4
Nd^{3+}	60	↑	↑	↑					3/2	6	9/2	$^4I_{9/2}$
Pm^{3+}	61	↑	↑	↑	↑				2	6	4	5I_4
Sm^{3+}	62	↑	↑	↑	↑	↑			5/2	5	5/2	$^6H_{5/2}$
Eu^{3+}	63	↑	↑	↑	↑	↑	↑		3	3	0	7F_0
Gd^{3+}	64	↑	↑	↑	↑	↑	↑	↑	7/2	0	7/2	$^8S_{7/2}$
Tb^{3+}	65	↑↓	↑	↑	↑	↑	↑	↑	3	3	6	7F_6
Dy^{3+}	66	↑↓	↑↓	↑	↑	↑	↑	↑	5/2	5	15/2	$^6H_{15/2}$
Ho^{3+}	67	↑↓	↑↓	↑↓	↑	↑	↑	↑	2	6	8	5I_8
Er^{3+}	68	↑↓	↑↓	↑↓	↑↓	↑	↑	↑	3/2	6	15/2	$^4I_{15/2}$
Tm^{3+}	69	↑↓	↑↓	↑↓	↑↓	↑↓	↑	↑	1	5	6	3H_6
Yb^{3+}	70	↑↓	↑↓	↑↓	↑↓	↑↓	↑↓	↑	1/2	3	7/2	$^2F_{7/2}$
Lu^{3+}	71	↑↓	↑↓	↑↓	↑↓	↑↓	↑↓	↑↓	0	0	0	1S_0

The energy levels of $4f$ orbitals are described with $^{2S+1}L_J$ notation. The value of $2S+1$ represents the spin multiplicity by the total spin of S . The values of L and J give the total orbital angular momentum and total angular momentum, respectively. The value of L corresponds to the term symbols as follows.

L	0	1	2	3	4	5	6
Term symbol	S	P	D	F	G	H	I

The value of J is given by

$$J = L - S \quad (\text{for a shell less than half full})$$

$$J = L + S \quad (\text{for a shell more than half full})$$

S , L , J and $^{2S+1}L_J$ notations for each lanthanide ion are listed in Table 3-1.

The electronic energy levels of trivalent lanthanide ions were precisely investigated by Dieke, and they are schematically represented in a Dieke diagram (Figure 3-1). The luminescence from $4f - 4f$ transitions are well described on this diagram and spin – orbit coupling is more important than crystal field splitting for $4f - 4f$ transitions.

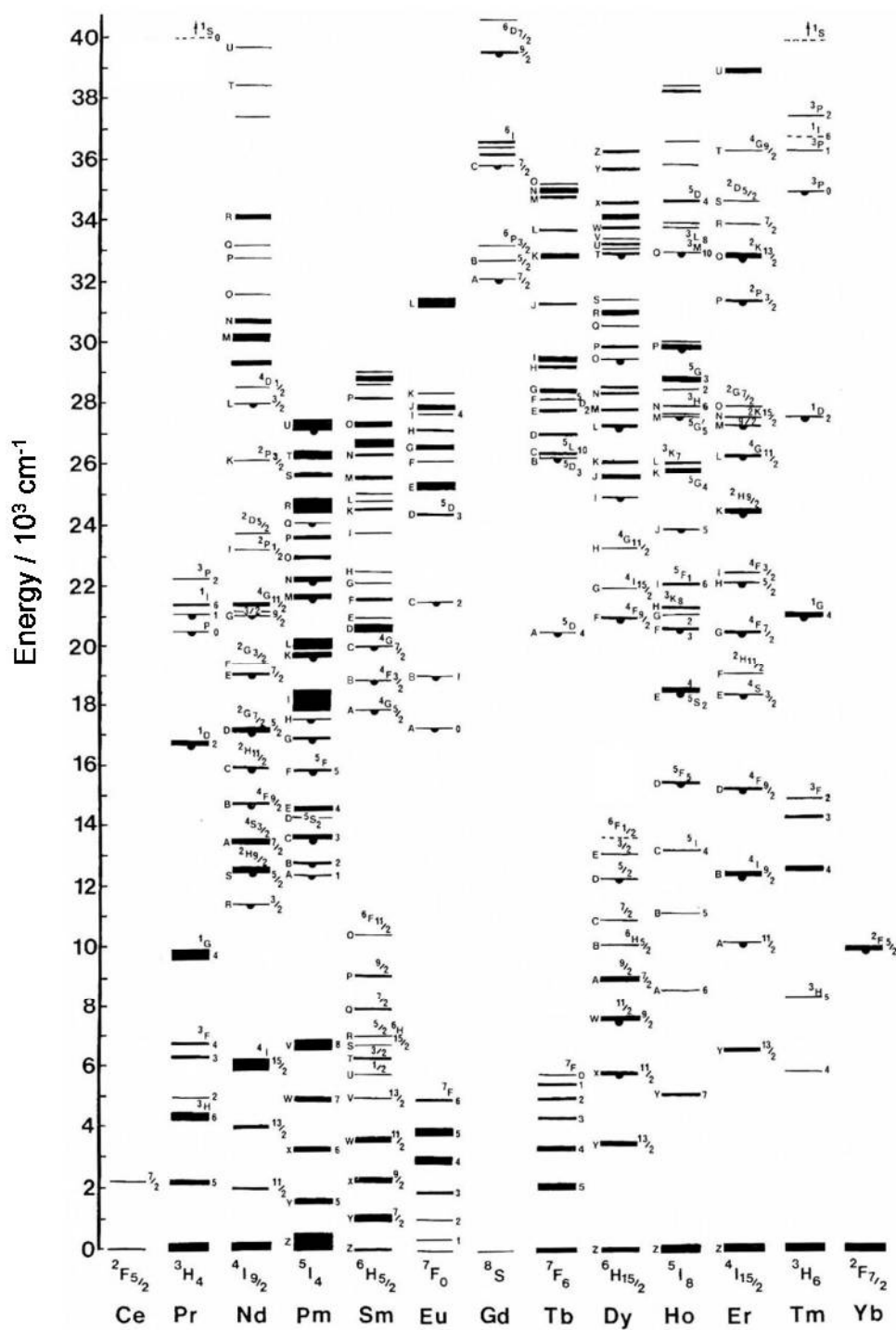


Figure 3-1 Energy levels of trivalent lanthanide ions.²

3.4 Luminescence from 5d – 4f transitions

In contrast with 4f – 4f transitions, 4f – 5d transitions are parity allowed resulting in strong absorption and luminescence. These transitions show relatively short lifetimes, 10^{-7} to 10^{-8} s for Ce^{3+} and 10^{-5} to 10^{-6} s for Eu^{2+} .¹ The 5d states are strongly influenced by the coordination environment in the host compounds, and crystal field splitting is more important than spin – orbit coupling for 4f – 5d transitions. The 4f – 5d transition energies in Ce^{3+} , Pr^{3+} and Eu^{2+} are relatively smaller than the energies in other lanthanide ions and potentially show luminescence determined by the energy level relation between the 4f and 5d levels. When 5d energy levels are lowered below 4f energy levels by the red shift in the compounds, direct intense luminescence between these levels can be seen. The red shift, which is the energy shift of 5d states from free gaseous level, is comprised of centroid shift and crystal field splitting. The schematic diagram of the energy shift is illustrated in Figure 3-2. When a Ce^{3+} ion is in a crystal, the 5d levels of Ce^{3+} are lowered by the centroid shift related with covalency and polarizability of the anions around it, then its 5 orbitals are split by the crystal field splitting related with the shape and the size of the coordination polyhedron, making some of the 5d levels even lower. These lower energy levels enable intense absorption of lower energy light in the visible region such as blue LED lights. This mechanism is the key for the LED phosphors. Ce^{3+} ions have a doublet energy level split by about 2000 cm^{-1} on the 4f ground state that widens the emission spectra, which can be an advantage for general lighting applications.

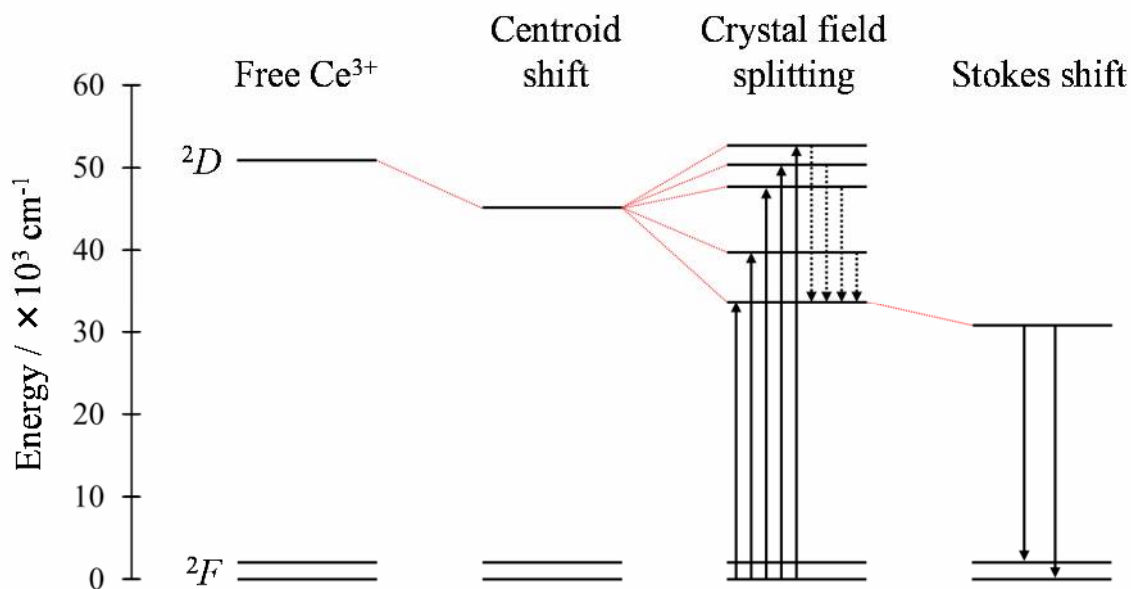
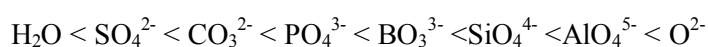


Figure 3-2 Energy shift of 5d states of Ce^{3+} in LiLuF_4 compound affected by centroid shift, crystal field splitting and Stokes shift. Solid arrows show absorption and emission, and dashed arrows represent phonon relaxations.³

Figure 3-3 shows the degree of red shift in the case of Ce^{3+} and Eu^{2+} doped in a variety of compounds.^{4,5} It is clear that the degrees of centroid shift vary in different types of host compounds and Ce^{3+} and Eu^{2+} have quite similar trends, especially relating to the type of anions. It is well matched to the order of anion types so called *nephelauxetic series*.⁶



What should be noted here is the degree of centroid shift in the oxide. It has a relatively wide range in centroid shift compared with the others. In fact, the oxide contains many types of compounds such as phosphate, silicate, simple oxide and so on, and the determining factor of the centroid shift is complicated. It normally follows another *nephelauxetic series*, which agrees well with the degrees of centroid shift for Ce^{3+} in different types of oxides as shown in Figure 3-4.



The *nephelauxetic* effect is usually referred to as the covalency in the interaction between the lanthanide ions and the anions or as the polarizability of the coordinating anions. The stronger the covalent interaction between them or the more polarizable the anions around the lanthanide ions, the larger the centroid shift. The polarizability was found to have a linear relation with the inverse square of the average electronegativity of the cations in the lattice.⁷ The smaller electronegativities of the cations in the host lattice can increase the polarizability of the anions around the lanthanide ions, leading to better orbital overlap between the lanthanide ions and ligands. It eventually increases the degree of centroid shift.

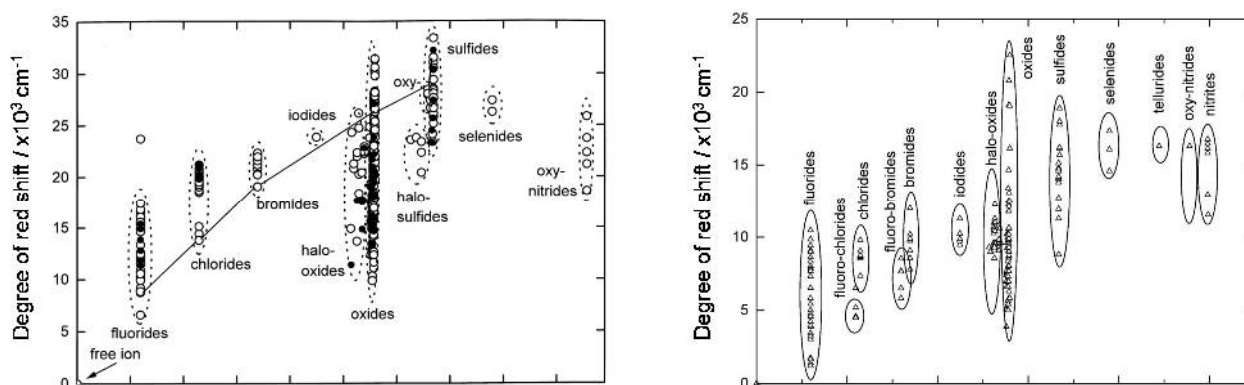


Figure 3-3 Degree of red shift for Ce^{3+} (left) and Eu^{2+} (right) in various compounds.^{4,5}

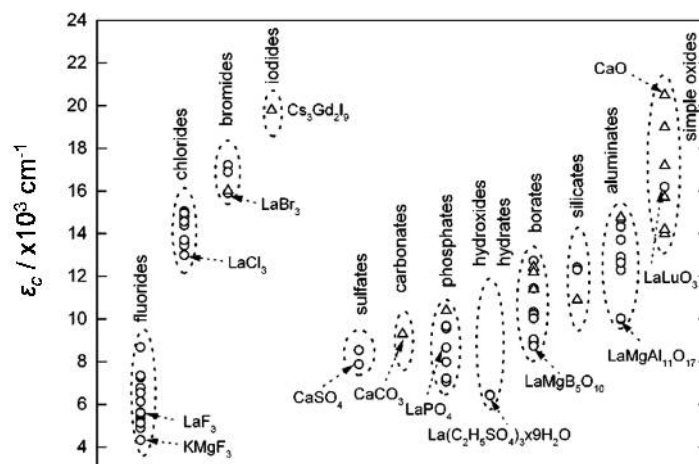


Figure 3-4 Degree of centroid shift, ϵ_c , for Ce^{3+} in various compounds, including different type of oxides.⁷

Another factor for the red shift is crystal field splitting, which originates from the coulombic repulsion between lanthanide anions and ligands, and is related to the spatial environment in the crystal lattice dominated by the size and shape of the coordination polyhedra around the lanthanide ions. The degrees of crystal field splitting are plotted in Figure 3-5 in the case of Ce^{3+} and Eu^{2+} .⁸ $R_{av}-0.5\Delta R$ represents the average distance to the ligands where $0.5\Delta R$ was introduced to roughly correct for lattice relaxation. Their trends are very similar, showing a clear relation between the energy of crystal field splitting and the bond length around Ce^{3+} or Eu^{2+} . The shorter the bond length around the lanthanide ions or the smaller the coordination number, the larger crystal field splitting. In the following sections, the practical phosphors, which have larger red shifts suitable for SSL applications, are introduced.

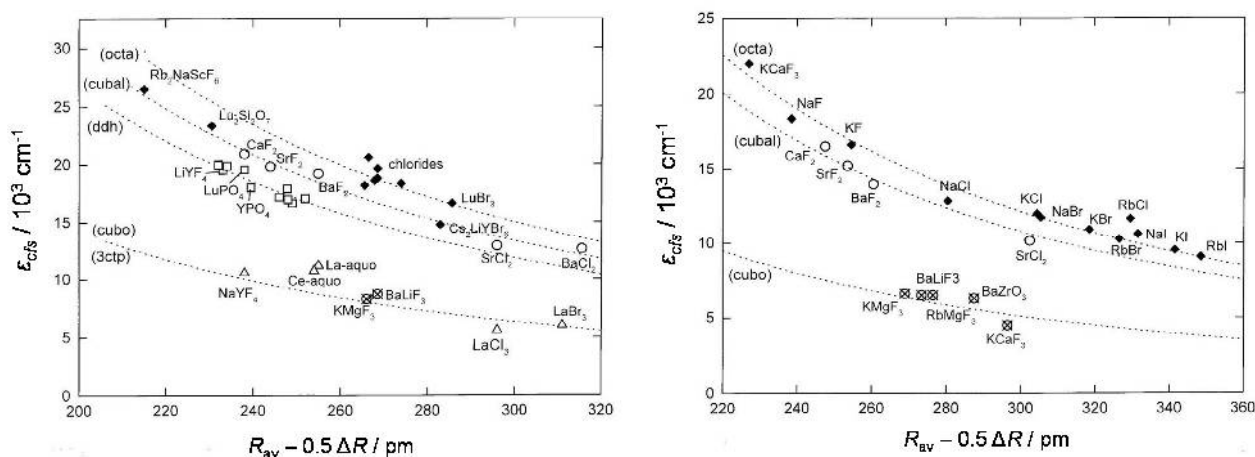


Figure 3-5 Degree of crystal field splitting, ϵ_{cfs} , for Ce^{3+} (left) and Eu^{2+} (right) in various compounds.⁸

3.5 Oxide phosphors

The white LED boom started with oxide phosphors based on the strong luminescence from $4f-5d$ transitions of Ce^{3+} or Eu^{2+} , which are still very competitive in the market. Many phases based on oxide systems had been studied for decades, however new discoveries rarely happened for LED use and nitride based phosphors have been focused on as a new research field for LED phosphors. The oxide still has certain advantages, particularly in stability under ambient atmosphere and simplicity of manufacturing. The key for finding new oxide phosphors is the proper understanding of the mechanism achieving large red shift by the crystal environment in the oxide hosts.

$\text{Y}_3\text{Al}_5\text{O}_{12}:\text{Ce}^{3+}$

Ce^{3+} doped $\text{Y}_3\text{Al}_5\text{O}_{12}$ with the garnet structure ($\text{YAG}:\text{Ce}^{3+}$) is a yellow emitting oxide phosphor, which has been dominating the white LED market with certain advantages as follows.

1. High quantum efficiency originating from highly crystalized particles, with suitable flux.
2. Broad luminescence spectrum comprised of the doublet emission band corresponding to the $5d \rightarrow 4f$ transition from $5d$ to ${}^2\text{F}_{5/2}$ or ${}^2\text{F}_{7/2}$, separated by 2000 cm^{-1} .
3. Availability of fine color tuning by substituting Y atoms with Gd atoms for longer wavelength shift in the emission peak, and Y atoms with Lu atoms or Al atoms with Ga atoms for shorter shift.
4. Chemical stability owing to rigid garnet-type crystal structure.
5. Competitiveness in productivity based on well-established process methods and inexpensive starting materials.

The crystal structure of $\text{Y}_3\text{Al}_5\text{O}_{12}$ is a cubic garnet with the space group $I\bar{a}3d$, in which the Y atom is located in the center of a dodecahedron coordinated by eight oxygen atoms. Al has two atomic positions: one is in the center of an octahedron coordinated by six oxygen atoms and the other is in the center of a tetrahedron coordinated by four oxygen atoms. Ce^{3+} ions occupy the position for Y atoms. $\text{YAG}:\text{Ce}^{3+}$ is synthesized by a solid-state reaction of the fine powder mixture of Y_2O_3 , Al_2O_3 and CeO_2 by firing at about 1500°C under reducing atmosphere. Figure 3-6 shows emission and excitation spectra of $\text{YAG}:\text{Ce}^{3+}$ in various Ce^{3+} concentrations.

Ce^{3+} in YAG absorbs the blue light from LEDs well, whereas it does not match the near-UV LED. $\text{YAG}:\text{Ce}^{3+}$ with partial substitution of Y atoms and Al atoms covers wavelengths from 510 nm to 590 nm in emission peak position maintaining high quantum efficiency, which is explained in section 4.4.3. The emission band has 130 nm of FWHM.⁹

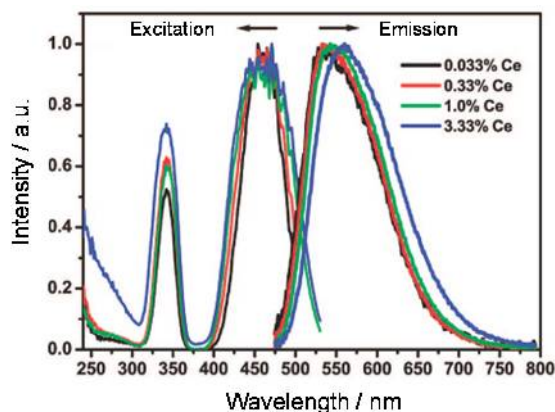


Figure 3-6 Emission and excitation spectra of YAG:Ce³⁺ with different Ce concentrations excited at 450 nm and monitored at each maximum emission.¹⁰

(Ba,Sr)₂SiO₄:Eu²⁺

(Ba,Sr)₂SiO₄:Eu²⁺ shows bright green emission when excited by near UV or blue LED and has been contributing to white LEDs as non-garnet oxide phosphor despite its disadvantages (strong thermal quenching and a worse reliability of a long lasting operation). (Ba,Sr)₂SiO₄ has an orthorhombic lattice with the space group *Pmnb*, in which two cation sites are distinguishable: one site is coordinated by ten oxygen atoms and the other site is coordinated by nine oxygen atoms.¹¹ The starting materials of BaCO₃, SrCO₃, SiO₂ and Eu₂O₃ powder are mixed and reacted at about 1250 °C under reducing atmosphere. When Eu²⁺ is doped in (Ba,Sr)₂SiO₄, the emission color varies depending on the composition of divalent cation: Ba emits at 505 nm and Sr emits at 575 nm, while a mixture of Ba atom and Sr atom comes between them.¹² Figure 3-7 shows the emission and excitation spectra of (Ba,Sr)₂SiO₄:Eu²⁺ in various Ba/Sr ratios.

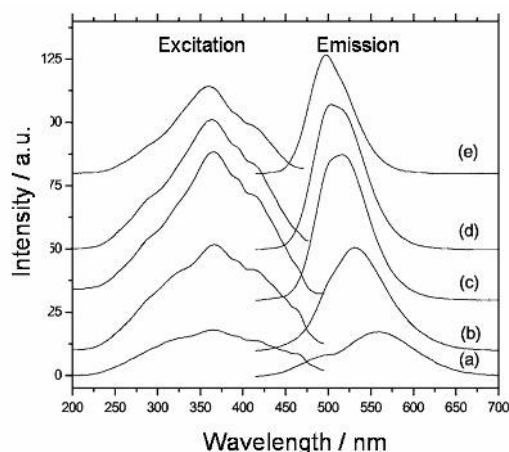


Figure 3-7 Emission and excitation spectra of (a):Sr₂SiO₄:Eu²⁺ (b):(Ba_{0.25}Sr_{0.75})₂SiO₄:Eu²⁺ (c):(Ba_{0.5}Sr_{0.5})₂SiO₄:Eu²⁺ (d):(Ba_{0.75}Sr_{0.25})₂SiO₄:Eu²⁺ (e):Ba₂SiO₄:Eu²⁺ excited at 365 nm and monitored at each maximum emission.¹²

3.6 Nitride and oxy-nitride phosphors

Covalent nitrides are suitable for phosphor host lattices that have wide band gaps behaving as insulators or semiconductors. Due to a higher charge of N^{3-} compared with O^{2-} , a large red shift is expected, which is a result of lowering the $5d$ energy states, known as nephelauxetic effect, and enlarging the crystal field splitting of $5d$ energy states in Eu^{2+} or Ce^{3+} . A smaller Stokes shift is also expected in a more rigid crystal lattice forming a more extended network of SiN_4 with increasing N^{3-} ratio to O^{2-} . The oxy-nitride and nitride phosphors have significant advantages in optimizing the absorption spectra for the blue light from LEDs. Recently they have been getting more attention as phosphor host materials for SSL. Some characteristics of typical oxy-nitride and nitride phosphors are introduced as follows.

$CaAlSiN_3:Eu^{2+}$

Eu^{2+} -activated $CaAlSiN_3$ is a deep red emitting nitride phosphor. $CaAlSiN_3$ has an orthorhombic lattice with the space group $Cmc2_1$, containing six-membered rings formed by linking the corners of $[SiN_4]$ and $[AlN_4]$ tetrahedra around the continuous channels for Ca atoms parallel to the c direction in the lattice. Two-thirds of N atoms are surrounded by three Si or Al atoms and the rest of the N atoms are surrounded by two Si or Al atoms. Increasing the ratio of three coordinated N atoms compared with other nitride phosphors, $CaAlSiN_3$ has a more rigid structure, achieving less thermal quenching and chemical stability. The $CaAlSiN_3:Eu^{2+}$ phosphors are prepared from a solid-state reaction by firing the powder mixture of Ca_3N_2 , $\alpha-Si_3N_4$, AlN and EuN_x at around 1600 °C under a 1.0 MPa nitrogen atmosphere.¹³ When Eu^{2+} ions are doped in $CaAlSiN_3$, $CaAlSiN_3:Eu^{2+}$ shows an extremely broad excitation band, which is enough to be efficiently excited by blue LED light. The emission band is also broad, having an emission peak position at 650 nm. Figure 3-8 shows the emission and the excitation spectra of $Ca_{0.90}Eu_{0.10}AlSiN_3$.

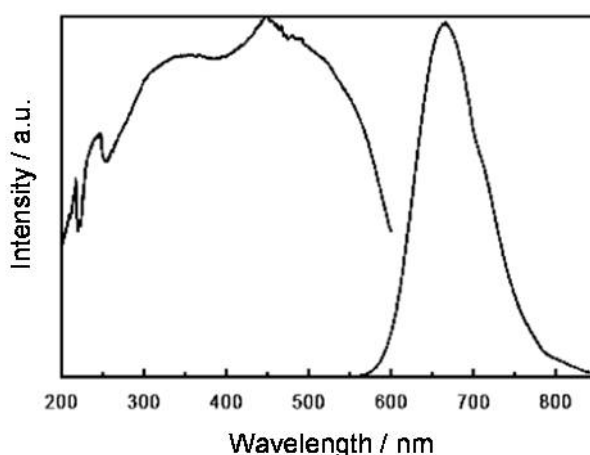


Figure 3-8 Emission and excitation spectra of $Ca_{0.90}Eu_{0.10}AlSiN_3$ excited at 450 nm and monitored at 650 nm.²⁰

α -SiAlON:Eu²⁺, α -SiAlON:Ce³⁺

The structure of α -SiAlON is isostructural with α -Si₃N₄, in which Si–N bonds are partially replaced by Al–N and Al–O bonds, having a hexagonal crystal structure with the *P31c* space group. α -SiAlON has the composition M_xSi_{12-m-n}Al_{m+n}O_nN_{16-n} (*x* is the solubility of M metal), where *m* is the substitution rate for Al–N and *n* for Al–O. The numbers *m* and *n* are optimized for improving the solubility of Eu²⁺ activator. In the case of Ca- α -SiAlON, M cations are Ca atoms occupying the interstitial sites coordinated by seven N/O anions. Eu²⁺ ions or Ce³⁺ ions share the site with Ca²⁺ ions. Ca- α -SiAlON is synthesized by solid-state reaction at around 1700 °C under a nitrogen gas pressure of 0.5-1.0 MPa, which prevents the powder from oxidation or decomposition. The powders of α -Si₃N₄, AlN, Ca₃N₂ (or CaCO₃), and Eu₂O₃ (or CeO₂) are used as starting materials.

Ce³⁺-activated Ca- α -SiAlON presents a blue emission with peak position from 485 nm to 503 nm depending on the Ce concentration from 5 mol% to 25 mol% under the 389 nm excitation, which matches near-UV LED applications.^{14,15} When Ca- α -SiAlON is activated by Eu²⁺, it shows a broad yellow emission with a peak at 590 nm and a broad excitation band having a peak position around 400 nm and a shoulder peak on the longer wavelength side. This enables Ca- α -SiAlON Eu²⁺ to be excited by near-UV or blue LEDs.¹⁶ Figure 3-9 shows the emission and excitation spectra measured at room temperature.

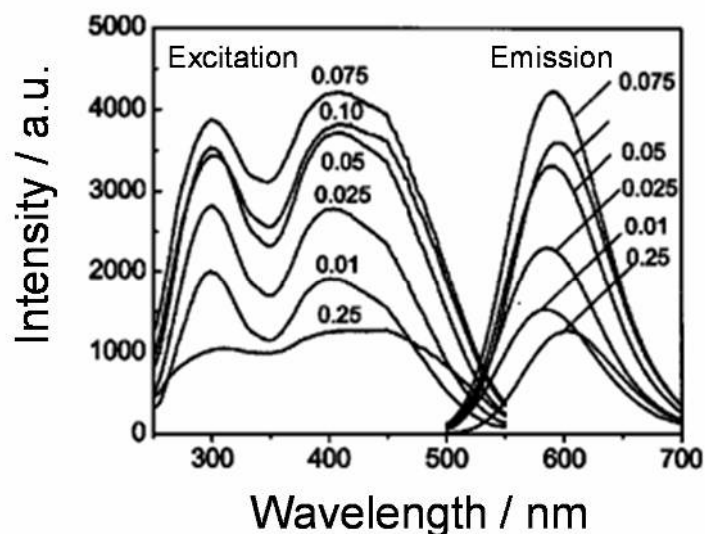


Figure 3-9 Emission and excitation spectra of Ca- α -SiAlON:Eu²⁺ excited at 450 nm and monitored at 590 nm.¹⁶

β -SiAlON:Eu²⁺

Eu²⁺-activated β -SiAlON is a green emitting oxy-nitride phosphor for white LEDs combined with near-UV or blue LEDs. Its structure is a derivation of β -Si₃N₄ by the substitution of Si-N with Al-O, which has a hexagonal crystal lattice and the space group $P6_3$ or $P6_3/m$. β -SiAlON has the chemical composition of Si_{6-z}Al_zO_zN_{8-z}, where z is the number of Al-O pairs replacing the Si-N pairs. β -SiAlON:Eu²⁺ is synthesized from a powder mixture of α -Si₃N₄, AlN, Al₂O₃ and Eu₂O₃ at around 1900 °C under a nitrogen gas pressure of 1.0 MPa. Optimization of z value and Eu²⁺ concentration is required to synthesize the pure phase of β -SiAlON:Eu²⁺ since the solubility of Eu²⁺ ion is strongly related to the z value and an impurity phase appears with higher z value.¹⁷ When Eu²⁺ ions are doped in β -SiAlON, they can occupy the continuous channels parallel to c direction in the lattice, which results in intense green emission ascribed to the $5d-4f$ transition of Eu²⁺ ions. The emission peak position shifts to longer wavelength when the z value increases, accompanied by the expansion of the unit cell. With the z value of 0.17, it shows an emission peak at around 535 nm and a full width at half maximum of 55 nm at room temperature.¹⁸ However measuring photoluminescence at 6 K reveals that the emission band of β -SiAlON is comprised of several sharp peaks those peak positions are independent of the z value.¹⁹ Figure 3-10 shows the emission and excitation spectra measured at room temperature.

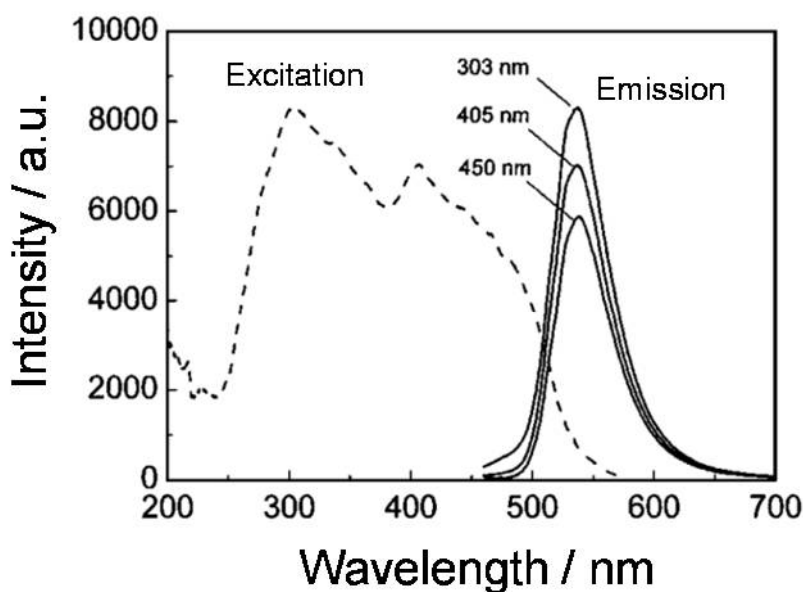


Figure 3-10 Emission and excitation spectra of β -SiAlON:Eu²⁺ excited at 303, 405 and 450 nm and monitored at 535 nm.¹⁷

(Ca,Sr,Ba)Si₂O₂N₂:Eu²⁺

Eu²⁺-activated MSi₂O₂N₂ (M=Ca, Sr, Ba) are blue-green to yellow phosphors tuned by varying the composition of Ca, Sr and Ba. MSi₂O₂N₂ compounds have same crystal lattices, but different space groups: *P2₁/c* for Ca, *P2₁/m* for Sr and *Cmcm* for Ba.²⁰ CaSi₂O₂N₂ and SrSi₂O₂N₂ have analogous structures containing the layers of [Si₂O₂N₂]²⁻, in which the N atom bridges three Si atoms forming corner sharing SiON₃ tetrahedra, and the O atoms terminate the tetrahedral layers by bonding to Si. There are four different sites for Ca or Sr ions, each coordinated by six O atoms in a distorted trigonal prism cage.²¹ The MSi₂O₂N₂:Eu²⁺ phosphors are prepared with a powder mixture of α-Si₃N₄, SiO₂, Eu₂O₃ and alkali earth carbonates (BaCO₃, SrCO₃ or CaCO₃) by firing at around 1600 °C under a nitrogen gas pressure of 0.5 MPa.²² When 2 mol% of Eu²⁺ is doped in MSi₂O₂N₂ with respect to M sites, it shows a different color of emission for each cation of Ba, Sr and Ca. BaSi₂O₂N₂:Eu²⁺, SrSi₂O₂N₂:Eu²⁺ and CaSi₂O₂N₂:Eu²⁺ emit blue-green light having a peak at 494 nm with a FWHM of 24 nm, green light having a peak at 537 nm with a FWHM of 54 nm and yellow light having a peak at 560 nm with a FWHM of 74 nm, respectively. Figure 3-11 shows emission and excitation spectra measured at 6 K, however it should be noted that the emission characteristics described above are at room temperature.²³

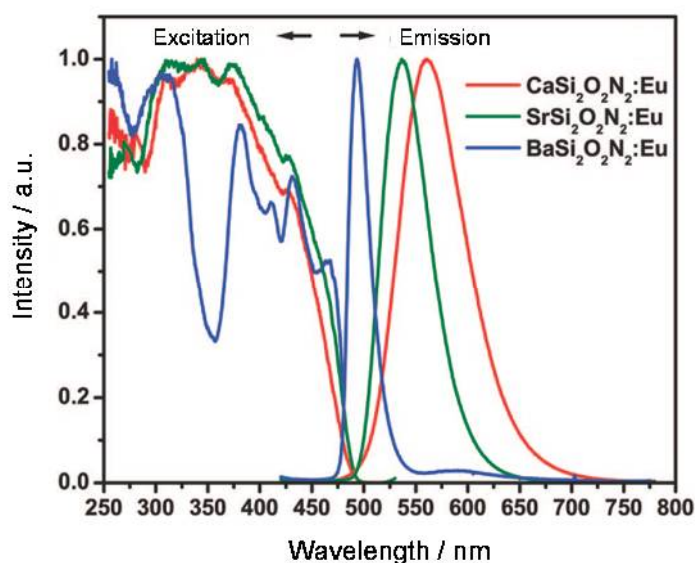


Figure 3-11 Emission and excitation spectra of BaSi₂O₂N₂:Eu²⁺, SrSi₂O₂N₂:Eu²⁺ and CaSi₂O₂N₂:Eu²⁺ with 2 mol% doping excited at 450 nm and monitored at each maximum emission.²³

(Ca,Sr,Ba)₂Si₅N₈:Eu²⁺

Eu²⁺-activated M₂Si₅N₈ (M=Ca, Sr, Ba) are orange or red emitting phosphors depending on the type of cation. Ba₂Si₅N₈ and Sr₂Si₅N₈ have orthorhombic lattice systems with the space group *Pmm2*₁, while Ca₂Si₅N₈ has a monoclinic system with the *Cc* space group. On the other hand, three M₂Si₅N₈ systems have quite similar local coordination, in which half of the N atoms bridge three Si atoms and rest of the N atoms bridge two Si atoms linking the SiN₄ tetrahedra. The coordination of Ba atoms and Sr atoms in their systems are eight or nine, whereas Ca atoms are coordinated by seven nitrogen atoms. M₂Si₅N₈ has two crystallographic sites for Ba, Sr or Ca atoms, in which Eu²⁺ ions are located. The M₂Si₅N₈:Eu²⁺ phosphors are synthesized by a solid-state reaction from the ground powder mixture of α-Si₃N₄, EuN_x and alkali earth nitrides (Ca₃N₂, SrN_x or BaN_x), heated in the furnace at around 1600 °C under 0.5 MPa nitrogen atmosphere.²² The emission peak wavelength of Ba₂Si₅N₈:Eu²⁺ shifts from 570 to 680 nm by increasing the Eu²⁺ concentration. Sr₂Si₅N₈:Eu²⁺ from 609 to 680 nm and Ca₂Si₅N₈:Eu²⁺ from 605 to 615 nm, respectively. Their excitation band is similar with a maximum around 400 nm followed by a shoulder peak on the longer wavelength side, which matches to the light from near UV and blue LEDs.^{22,24} Figure 3-12 shows the emission spectra of Ba₂Si₅N₈:Eu²⁺ with different Eu concentrations from x=0.02 to 2.00.

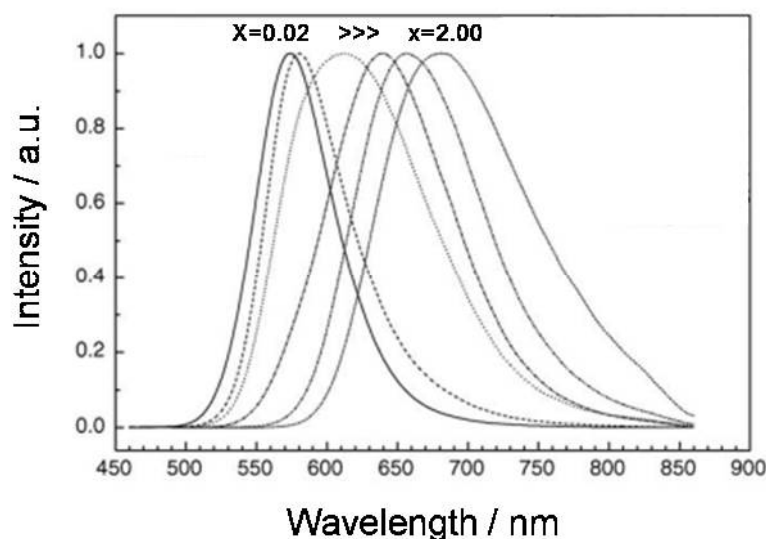


Figure 3-12 Emission spectra of Ba_{2-x}Eu_xSi₅N₈.²⁴

La₃Si₆N₁₁:Ce³⁺

Ce³⁺-activated La₃Si₆N₁₁ is an unusual yellow emitting nitride phosphor with small thermal quenching. La₃Si₆N₁₁ has a tetragonal lattice with the space group *P4bm*, forming three-dimensional networks with large voids by linking the corners of [SiN₄] tetrahedra around the two distinguishable La atoms, which are arranged into continuous channels parallel to the *c* direction in the lattice. One quarter of the N atoms are surrounded by three Si atoms and the rest are surrounded by two Si atoms. The La₃Si₆N₁₁:Ce³⁺ phosphors are synthesized by solid-state reaction with the ground mixture of LaN, α-Si₃N₄, CeN powders, fired at around 1600 °C under a nitrogen gas pressure of 1.0 MPa. With the doping of Ce³⁺ ions into La₃Si₆N₁₁, La₃Si₆N₁₁:Ce³⁺ shows intense yellow emission comprised of two emission peaks located at 543 nm and 585 nm, which corresponded to the energy transitions from *5d* to ²F_{5/2} and ²F_{7/2}, respectively.²⁵ Figure 3-13 shows the emission and the excitation spectra of La_{2.94}Ce_{0.06}Si₆N₁₁.

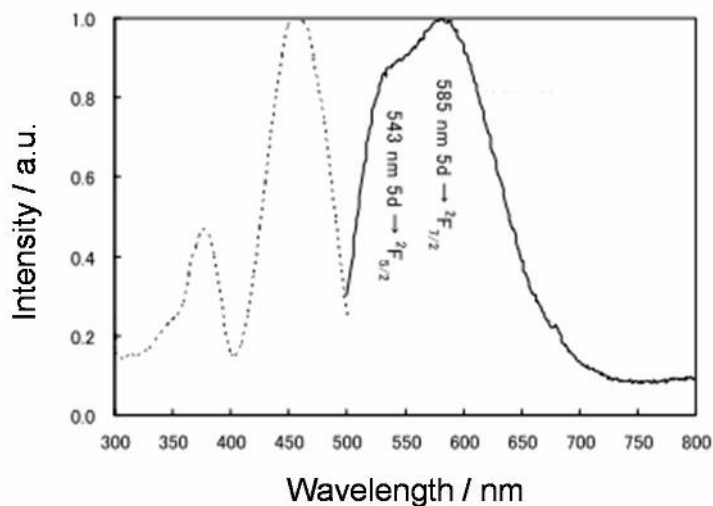


Figure 3-13 Emission (solid line) and excitation (dotted line) spectra of La_{2.94}Ce_{0.06}Si₆N₁₁ excited at 455 nm and monitored at 585 nm.²⁵

3.7 References

- 1 T. Kano, In Phosphor Handbook, W. Yen, S. Shionoya and H. Yamamoto, CRC Press, Boca Raton, 2007, p.191.
- 2 Dieke, G. H., Spectra and Energy Levels of Rare Earth Ions in Crystals, Interscience Publishers: New York, 1968.
- 3 P. Dorenbos, In Phosphor Handbook, W. Yen, S. Shionoya and H. Yamamoto, CRC Press, Boca Raton, 2007, p.139.
- 4 P. Dorenbos, *J. Lumin.*, 2000, **91**, 155.
- 5 P. Dorenbos, *J. Lumin.*, 2003, **104**, 239.
- 6 P. Dorenbos, J. Andriessen, and C.W.E. van Eijk, *J. Solid State Chemistry*, 2003, **171**, 133.
- 7 P. Dorenbos, *Phys. Rev. B*, 2002, **65**, 235110.
- 8 P. Dorenbos, *J. Alloys Compounds*, 2002, **341**, 156.
- 9 K. Murakami, In Phosphor Handbook, W. Yen, S. Shionoya and H. Yamamoto, CRC Press, Boca Raton, 2007, p.502.
- 10 V. Bachmann, C. Ronda and A. Meijerink, *Chem. Mater.*, 2009, **21**, 2077.
- 11 J. S. Kim, Y. H. Park, J. C. Choi and H. L. Park, *J. Electrochem. Soc.*, 2005, **152**, H135.
- 12 T. L. Barry, *J. Electrochem. Soc.: SOLID STATE SCIENCE*, 1968, **115**, 1182.
- 13 K. Uheda, N. Hirosaki, Y. Yamamoto, A. Naito, T. Nakajima, and H. Yamamoto, *Electrochem. & Sol. State Lett.* 2006, **9**, H22.
- 14 R.-J. Xie, N. Hirosaki, M. Mitomo, Y. Yamamoto, T. Suehiro and N. Ohashi, *J. Am. Ceram. Soc.*, 2004, **87**, 1368.
- 15 R.-J. Xie, N. Hirosaki, M. Mitomo, T. Suehiro, X. Xin and H. Tanaka, *J. Am. Ceram. Soc.*, 2005, **88**, 2883.
- 16 R.-J. Xie and N. Hirosaki, *Appl. Phys. Lett.*, 2004, **84**, 28.
- 17 N. Hirosaki, R.-J. Xie and K. Kimoto, *Appl. Phys. Lett.*, 2005, **86**, 211905.
- 18 Y. Q. Li, N. Hirosaki, R.-J. Xie, T. Takeda and M. Mitomo, *J. Solid State Chem.*, 2008, **181**, 3200.
- 19 K. Takahashi, K. Yoshimura, M. Harada, Y. Tomomura, T. Takeda, R.-J. Xie and N. Hirosaki, *Sci. Technol. Adv. Mater.*, 2012, **13**, 015004.
- 20 M. Seibald, T. Rosenthal, O. Oeckler, W. Schnick, *Crit. Rev. Solid State and Mater. Sci.*, 2014, **39**, 215.
- 21 H. A. Hoppe, F. Stadler, O. Oeckler and W. Schnick, *Angew. Chem. Int. Ed.*, 2004, **43**, 5540.
- 22 R.-J. Xie, In Phosphor Handbook, W. Yen, S. Shionoya and H. Yamamoto, CRC Press, Boca Raton, 2007, p.334.
- 23 V. Bachmann, C. Ronda, O. Oeckler, W. Schnick and A. Meijerink, *Chem. Mater.*, 2009, **21**, 316.
- 24 Y.Q. Li, J.E.J. van Steen, J.W.H. van Krevel, G. Botty, A.C.A. Delsing, F.J. DiSalvo, G. de With and H.T. Hintzen, *J. Alloys Compounds*, 2006, **417**, 273.
- 25 T. Seto, N. Kijima and N. Hirosaki, *ECS Trans.*, 2009, **25**, 247.

Chapter 4 Experimental

4.1 Introduction

The structural, spectroscopic and topographical characterization techniques in this study are described in this chapter, including sample preparation. The characterization method for LEDs is also introduced as an evaluation for practical application.

4.2 High-temperature ceramic synthesis

The phosphors are typically synthesized via solid-state reaction at high temperature using solid chemicals as starting materials. In LED phosphors, a reducing or inert atmosphere (e.g. N₂ or H₂/N₂ gas mixture) is prepared for the reaction to reduce the activator of Ce³⁺ or Eu²⁺.

The reactants for oxide phosphors are usually metal oxides and carbonates, while nitride compounds are used for nitride phosphors. The glove box with inert atmosphere is used for moisture sensitive nitride chemicals. The raw materials are mixed well together in a mixer or ball mill and placed in crucibles made from materials such as alumina, zirconia or boron nitride. Smaller particle size of the reactants with larger surface area helps the reaction since these reactions rely on diffusion of ions between solid particles. The diffusion can be promoted using fluxes, which are usually halide compounds of alkali metal or alkaline earth metals with lower melting points, in order to obtain well crystalized particles. The typical synthesis temperatures are in the range from 1000 to 1600 °C. However when nitrides are synthesized, higher temperatures around 2000 °C and higher pressure are often required to prevent the decomposition and enhance the reaction of nitrides.¹

4.3 Structural characterization

The crystallographic characterizations in this work were performed on powder samples using powder diffraction techniques. Laboratory powder X-ray diffraction (PXRD) was applied as a first characterization to identify the main and impurity phases contained in the sample. Synchrotron PXRD was performed to refine the crystal structure parameters including lattice parameters and atomic positions. Neutron powder diffraction was used, when precise refinement for the oxygen atoms was required since neutrons are more sensitive to the lighter elements. The Rietveld method was used to refine the structures using the powder diffraction data. When an unknown phase was discovered in this work, electron diffraction was used to estimate the crystal system, synchrotron PXRD was utilized to obtain the precise diffraction profile and the direct-space method was used to determine the unknown crystal structure.

Basic theory of XRD

X-rays incident to the sample are diffracted by electrons of atoms and elements with high atomic numbers (i.e. with more electrons) interact with X-rays more leading to higher intensity of diffraction peaks. All X-rays are reflected in the same direction are superposed. The repetition of units in crystalline material (the crystal lattice) gives rise to strong reflections of the X-ray in special conditions. By constructive and destructive interference of the scattered X-rays, sharp strong maxima emerge only at special angles, which follow the Bragg's Law. The condition is given by the Bragg equation:

$$n\lambda = 2d_{hkl} \sin \theta \quad \text{Equation 4-1}$$

where n is an integer, λ is the wavelength of the X-rays, d is the interplanar spacing of parallel lattice planes, which are characterized by the triplet Miller indices hkl , and θ is the diffraction angle. 2θ is the angle between incoming and outgoing X-rays.²

Laboratory PXRD

Laboratory PXRD data were collected using a Bruker D8 diffractometer (Bragg-Brentano geometry, fixed sample). Cu-K α ($\lambda \alpha_1 = 1.54056 \text{ \AA}$, $\lambda \alpha_2 = 1.54439 \text{ \AA}$) was used as the source of incident X-rays, generated in a X-ray tube with electric power settings of 40 kV and 40 mA. The incident X-ray optics settings were: primary and secondary Soller slits: 2.5° , divergence and anti-scatter slits: 0.5° . Scattered X-rays were detected by a position sensitive detector (LynxEye) in a continuous scan mode with the step-size in the range of $0.02 - 0.04^\circ$. The patterns were obtained in the 2θ range of $10 - 70^\circ$. Well ground samples were placed into sample holders, which were prepared from single crystal silicon substrates cut parallel to the (911) plane, removing the background scatter.

Synchrotron PXRD

The use of a synchrotron X-ray source has several major advantages over laboratory sources. Synchrotron sources are extremely intense, helping to collect the data rapidly and to suppress the noise, which allows precise refinement of the collected data. It is highly collimated, enabling lower divergence of the X-rays with much higher 2θ resolution. The tuning of the synchrotron radiation in wavelength is also an important aspect. Shorter wavelengths permit the access to much smaller d -spacings. These advantages allow us to collect data that enables us to solve and/or refine the crystal structure. In a synchrotron, electrons pass through a storage ring guided by magnetic fields. Synchrotron radiation is emitted from the curved sections, when they are steered by bending in the magnetic fields. The synchrotron X-ray radiation is nearly polarized.³ Synchrotron PXRD data were obtained on beamline I11 at the Diamond Light Source facility, Harwell Research Laboratories, Oxford in

the UK.⁴ The wavelength of synchrotron X-rays was 0.82713 Å and scattered X-rays were detected by a 45 multi-analyzer Si(111) crystal (MAC) array detector at room temperature in Debye-Scherrer geometry. The well ground samples were placed in 0.3 mm glass capillaries and spun continuously during the measurement to suppress preferred orientation effects. Data points were recorded in the 2θ range of 1 – 150° at 0.001° step-size.

Neutron Powder Diffraction

Owing to the uncharged nature of neutrons, they are scattered by the nuclei of atoms rather than the electron clouds in contrast with X-rays. The scattering factor of neutrons does not rely on atomic number and neutrons can be scattered by lighter atoms as strongly as by heavier atoms. For that reason, neutron diffraction is more sensitive than X-rays to some lighter elements, such as nitrogen (^{14}N) and oxygen (^{16}O), which makes neutron diffraction useful to refine the oxygen and nitrogen positions in many oxides and nitrides including oxy-nitrides.

The time-of-flight technique is often used for data collection with a pulsed source of neutrons. Combining the De Broglie relationships and Bragg's law, d-spacing is calculated by the following equation.

$$\lambda = h/m_n v = ht/m_n L = 2d \sin \theta \quad \text{Equation 4-2}$$

where λ is the wavelength of neutrons, h is the Planck's constant, m_n is the mass of neutron, v is the velocity of the particle, t is the time of flight and L is the length of the flight path. The diffraction angle is fixed by the position of detectors.

Time of flight powder neutron diffraction data in this work were recorded on the diffractometer HRPD, ISIS, Rutherford Appleton Laboratory, in the UK. The high resolution powder diffractometer HRPD is equipped with a very long flight path of about 100 m. A ^3He gas tube detector is used for 30° (low angle) scattering and ZnS scintillators are used for 90° and 168° back scattering. The d -spacing range achieved on the HRPD diffractometer is 2.2 - 16.5 Å for low angle, 0.9 - 6.6 Å for 90° and 0.6 - 4.6 Å for back scattering.⁵

Electron diffraction

One of the best benefits of electron diffraction is the facility in the electron microscope, which enables selection of a particular area of the specimen and variation of the beam diameter to collect diffraction patterns at the same time from those phases of interest. The accelerating voltage of the electron microscope, V , and electron wavelength, λ , are related by this equation:

$$\lambda = \frac{h}{(2m_0 e V)^{1/2}} \quad \text{Equation 4-3}$$

where m_0 is electron mass and e is the charge of one electron. When electrons are accelerated by 300 kV, the

resulting λ value is 1.97 pm and this is the basis of the high resolving power of the electron microscope. Transmission electron microscope (TEM) has mainly two modes, Diffraction mode and Image mode. By inserting an objective aperture and removing a selected-area-diffraction (SAD) aperture, an image of a thin specimen can be seen on the viewing screen (Image mode). In contrast, by inserting a SAD aperture and removing an objective aperture, a diffraction pattern can be projected from the thin specimen (Diffraction mode).

The primary process of electron diffraction patterns analysis is identifying the reciprocal lattice sections, by a given lattice parameter, type of unit cell and the electron beam direction. The first step in analyzing electron diffraction patterns is measuring the d -spacing (d_{hkl}), which is calculated by the equation

$$d_{hkl} = \lambda L / R \quad \text{Equation 4-4}$$

where λL is known as the camera constant, which varies with lens settings in the microscope, and R is the distance between the diffracted spot and the center spot. Hence the electron diffraction method gives several % deviation in the unit cell parameters owing to a limitation of a determination in camera constant, which needs to be supported by the x-ray diffraction method to determine the unit cell parameters (Figure 4-1).^{6,7}

TEM samples were made using the standard procedure (grinding in ethanol before dropping onto a holey carbon support film). The powder dispersed easily, forming small fragments. A set of diffraction patterns was collected under precession conditions, each from a different fragment of the material, and at or close to low index zone axes. A pair of base vectors was identified for each diffraction pattern: the lengths of the two vectors and the angle between them were recorded.

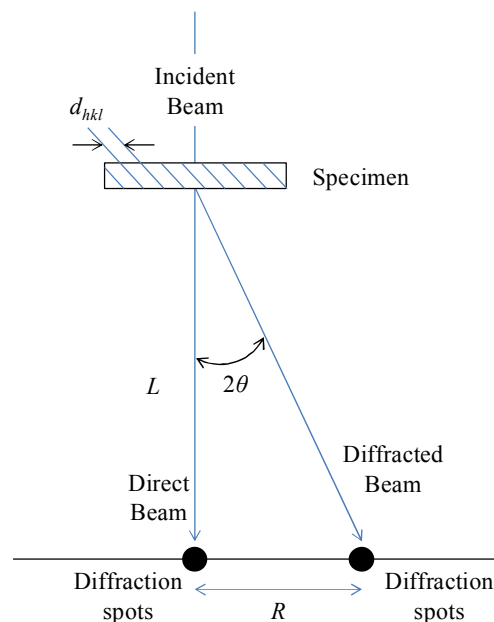


Figure 4-1 Spacing R between the direct beam and a scattering maximum in relation to L .

4.3.1 Rietveld Method

Rietveld refinement is based on the fitting between the observed diffraction profile from the sample and the calculated profile by adjusting the parameters for the structure model using least-squares minimization.⁸ There are various parameters to be refined such as atomic coordinates, thermal displacements and site occupancies for crystal structure parameters, unit cell and peak profile broadening for diffraction experiment parameters. The simulated diffraction profile is derived from the crystal structure model and normally crystallographic information file (CIF) is used. The calculated intensity of powder diffraction profile, Y_c , is proportional to square of structure factor, which is given by

$$Y_c \propto |F(\mathbf{h})|^2 \quad \text{Equation 4-5}$$

Structure factor $F(\mathbf{h})$ is:

$$F(\mathbf{h}) = \sum_{i=1}^N f_i(s_h) e^{2\pi i(\mathbf{h} \cdot \mathbf{x}_i)} \quad \text{Equation 4-6}$$

where h describes the triplet Miller indices hkl , $f_i(s_h)$ is a scattering factor and x_i is a fractional coordinates, for each of atoms with index i . The quality of the fit is evaluated in some factors as residues, being described in R_p , R_{wp} and reduced χ^2 , which are called profile factor, weighted profile factor and goodness-of-fit, respectively. The equations are given by

$$R_p = \frac{\sum |Y_o - Y_c|}{\sum Y_o} \quad \text{Equation 4-7}$$

$$R_{wp} = \sqrt{\frac{\sum w(Y_o - Y_c)^2}{\sum w Y_o^2}} \quad \text{Equation 4-8}$$

$$\chi^2 = \frac{\sum w(Y_o - Y_c)^2}{(N_{\text{obs}} - N_{\text{var}})} \quad \text{Equation 4-9}$$

When integrated intensity from the diffraction data is so high, R_p , R_{wp} can get smaller. In this case, χ^2 is useful corrected by the data points difference between observed (N_{obs}) and variance (N_{var}). However these values should not be discussed as just number. They need to be combined with other characterization containing physical meanings.

4.3.2 Structure determination for new phases

Ab initio structure determination is more complicated from powder diffraction data than from single-crystal

diffraction data, due to the projection of the three-dimensional diffraction pattern on a single dimension. A precise diffraction pattern is necessary for structure determination, such as Synchrotron X-ray diffraction data, to differentiate the overlapped peaks. The methods for structure determination are categorized into mainly two groups of Reciprocal-space methods: so-called direct methods and Direct-space methods. In direct methods, low intensity reflections from diffraction patterns are important since diffraction peaks are strongly overlapping, which is responsible for the extraction of structure-factor amplitudes from the powder pattern. In Direct-space methods, building units (molecules, polyhedra, atoms) are located in the unit cell and compared between calculated and observed diffraction patterns. In this study, the model for the crystal structure of the sample was obtained by the ab initio structure determination software FOX (free objects for crystallography). The direct-space method is adopted and the reverse Monte Carlo approach is used for the algorithms in FOX.⁹ The resulting structure was refined by GSAS (software for Rietveld Refinement) and depicted in VESTA (Three-Dimensional Visualization software).¹⁰

4.3.3 Effective coordination number (ECoN)

The idea of Effective Coordination Number (ECoN) was introduced by R. Hoppe in 1979 to deal with structures containing highly distorted coordination polyhedra.¹¹ The ECoN is independent of the nature of chemical bonds and relies on only the coordination geometry of bond lengths, whereas bond valence relies on the nature of chemical bond.¹² The ECoN is defined as the sum of w_i , which is the so called ‘bond weight’ of the i th bond:

$$\text{ECoN} = \sum_i w_i \quad \text{Equation 4-10}$$

where w_i is described with l_i (i th bond length) and l_{av} (weighted average bond length):

$$w_i = \exp\left[1 - \left(\frac{l_i}{l_{av}}\right)^6\right] \quad \text{Equation 4-11}$$

in which l_{av} is calculated with l_{min} (the smallest bond length in the coordination polyhedron) by the following equation:

$$l_{av} = \frac{\sum_i l_i \exp\left[1 - (l_i/l_{min})^6\right]}{\sum_i \exp\left[1 - (l_i/l_{min})^6\right]} \quad \text{Equation 4-12}$$

4.4 Spectroscopic characterization

Phosphors are luminescent materials and spectroscopic characterization is very important as a direct measure of their properties. There are several characterizations for phosphors, in which UV-vis reflectance spectroscopy, photoluminescence spectroscopy and photoluminescence quantum efficiency measurement are introduced as

follows. The temperature dependence of each measurement is also important.

4.4.1 UV-vis reflectance spectroscopy

When a powder layer has a semi-infinite thickness, the reflectance R_∞ , the absorption coefficient K and the scattering coefficient S follow next equation;

$$\frac{K}{S} = \frac{(1 - R_\infty)^2}{2R_\infty} \equiv F(R_\infty) \quad \text{Equation 4-13}$$

$F(R_\infty)$ is called remission function or Kubelka-Munk function. When S is independent of wavelength, $F(R_\infty)$ is in proportion to K . By measuring reflectance spectrum of the sample, the absorption of luminescence activators and host materials can be evaluated.¹³

In this work, UV-vis reflectance spectra were measured using a PerkinElmer Lambda 750 spectrophotometer, equipped with a deuterium and tungsten-halogen lamp as a light source, and double holographic grating monochromators for ultra-low stray light. The signals were detected by a standard R928 photomultiplier tube (PMT) UV-vis detector through a 6 mm diameter integrating sphere with Spectralon coating inside. The sample was placed in a holder with a quartz silica glass window and loaded into the sampling compartment blocking the terminal port of the integrating sphere for the optical path. A certified reflectance standard (Spectralon, Labsphere) was measured as a standard for the reflectance in a same configuration. Reflectance spectra were collected in the 200 – 800 nm range at 1 nm intervals with a scan rate of 200 nm/min.

4.4.2 Photoluminescence spectroscopy

Photoluminescence (PL) spectra are measured as intensity of emitted light against wavelength by fixing the excitation monochromator and scanning the emission monochromator, which gives a measurement of how many and what wavelength of photons are emitted. On the other hand, photoluminescence excitation (PLE) spectra are measured by fixing the emission monochromator and scanning the excitation monochromator, describing what wavelength of light can excite the material efficiently.¹⁴

PL and PLE spectra at room temperature and 77 K were mainly measured using a Horiba FluoroLog-3 spectrometer, and some PL and PLE data were obtained secondarily using a JASCO FP-6500 spectrometer. The temperature dependence of PL was measured by a multichannel spectrophotometer (model MCPD7000; Otsuka Electronics) above room temperature and by a multichannel spectrophotometer (model USB2000+, Ocean Optics) below room temperature.

Figure 4-2 shows a schematic of the Horiba FluoroLog-3 spectrometer, for which labels are given in the following text, Xenon lamp (A), monochromator (B), sample chamber (C), double-monochromator (D), PMT

detector (E) and Ar gas flow meter (F). The samples were placed in a holder with a quartz silica glass window. An sample holder built in-house was used to measure PL and PLE at 77 K (liquid nitrogen temperature) for Horiba FluoroLog-3 spectrometer and Argon gas was introduced into the sample holder to prevent water condensation. Figure 4-3 shows the configuration for temperature dependent PL measurement below room temperature.

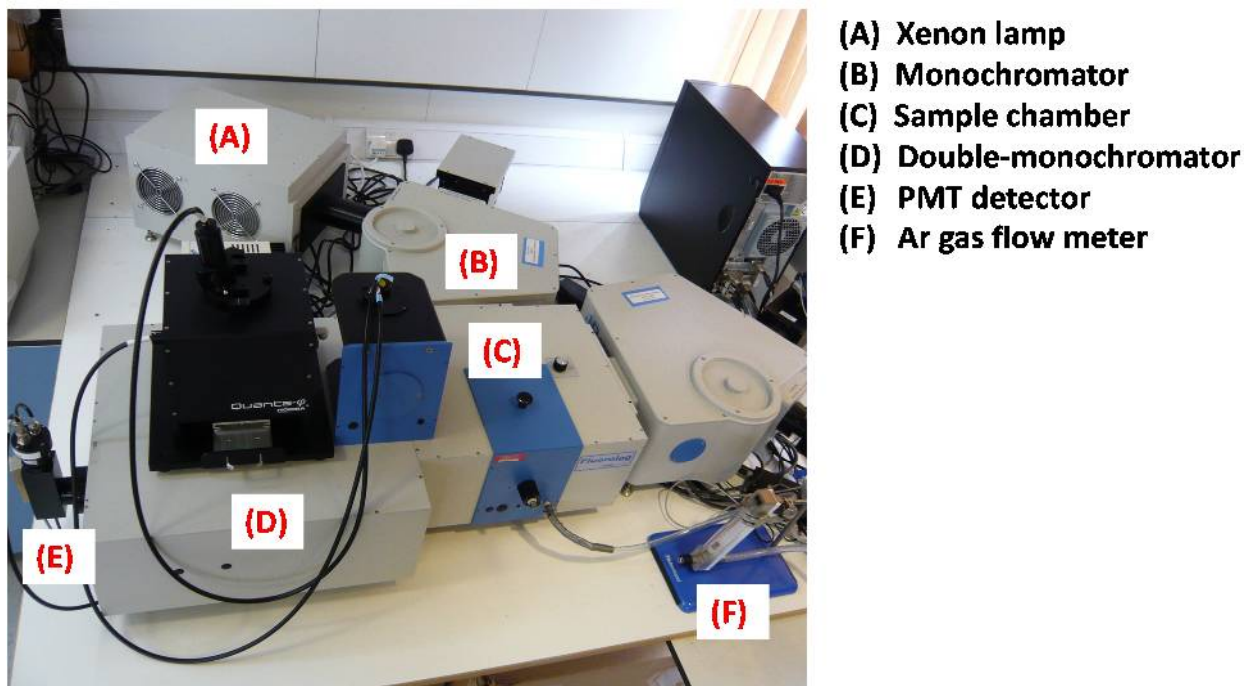


Figure 4-2 Schematic of modular Fluorolog-3 spectrofluorimeter used for PL and PLE measurements at room temperature and 77 K.

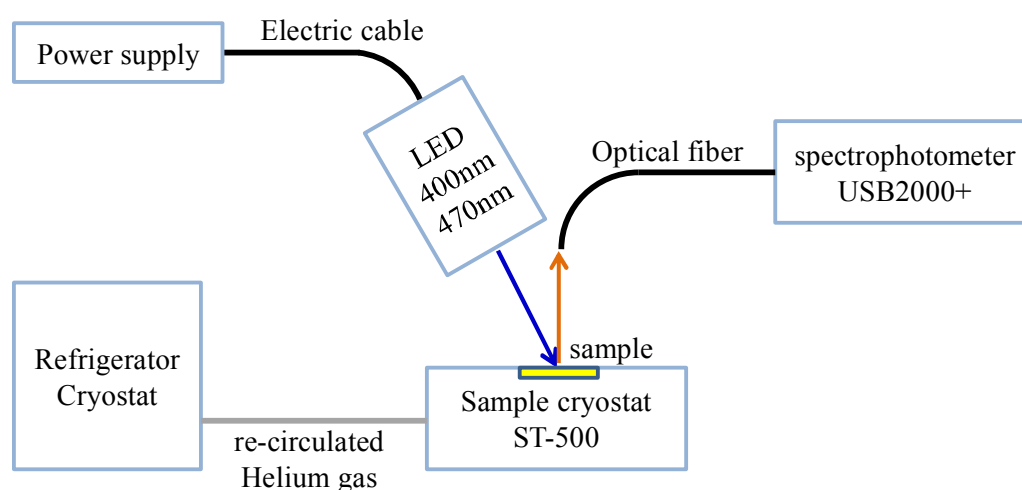


Figure 4-3 Measurement system configuration for temperature dependent PL below room temperature.

4.4.3 Photoluminescence Quantum Efficiency measurement

Quantum Efficiency (QE) characterizes how efficiently the phosphor converts light from excitation to emission. The conversion efficiencies of a phosphor are the ratios between photons in excitation light, in light absorbed by the phosphor and in light emitted by the phosphor. All photons involved in light conversion by the phosphor need to be collected and measured by the detector. Figure 4-4 presents the configuration of the QE measurement system. Monochromatic excitation light with the wavelength of either 400 nm or 455 nm is guided through the optical fiber into the integrating sphere, and all the photons are collected by the spectrophotometer via optical fiber. A 150 W Xenon lamp and USB2000+ spectrophotometer were used as a light source and a detector, respectively. To calculate the conversion efficiency of a phosphor, two spectra need to be collected. The first is a blank without phosphor (Spectralon was used as a certified reflectance standard in this work), which gives a measure of all photons in the excitation light (I_{EX}). The second is measured with the phosphor comprised of all reflected photons (I_R) and all emitted photons (I_{EM}). The wavelength between 385 nm and 415 nm was considered as an excitation, and from 416 nm to 780 nm as an emission in the test with 400 nm excitation. Likewise, they are from 440 nm to 470 nm as an excitation and from 471 nm to 780 nm as an emission in the test with 455 nm excitation. The efficiencies of Abs. (absorbance), iQE (internal quantum efficiency) and eQE (external quantum efficiency) are calculated as follows:

$$\text{Abs.} = \frac{I_{EX} - I_R}{I_{EX}} \quad \text{Equation 4-14}$$

$$\text{iQE} = \frac{I_{EM}}{I_{EX} - I_R} \quad \text{Equation 4-15}$$

$$\text{eQE} = \text{Abs.} \times \text{iQE} = \frac{I_{EM}}{I_{EX}} \quad \text{Equation 4-16}$$

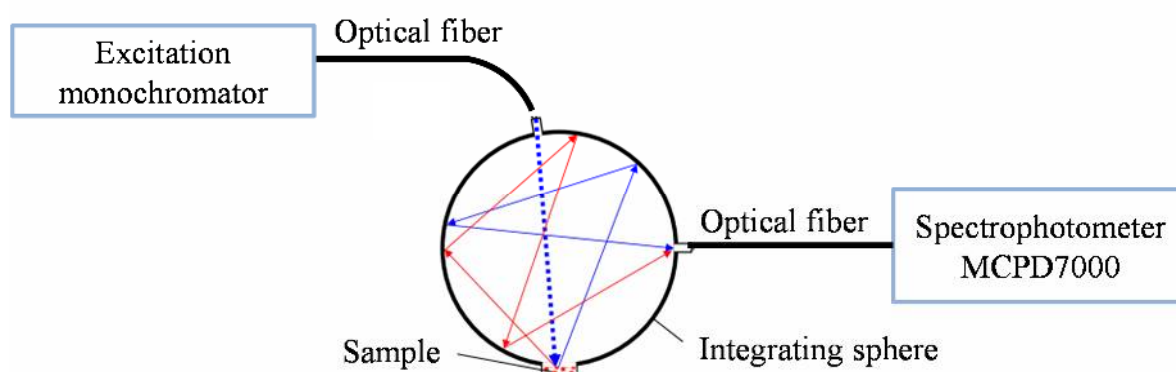


Figure 4-4 Configuration for QE measurement. The arrows indicate excitation light (dotted blue), reflected excitation light (solid blue) and phosphor emission light (solid red).

4.5 Topographical and elemental analysis (SEM and EDX)

The scanning electron microscope (SEM) is used for observing the particle shape, size and surface of phosphors. When a specimen is irradiated with an accelerated electron beam, secondary electrons are emitted from the surface of specimen and are detected by the PMT detector. The display synchronized to the electron-probe scan shows an SEM image.

The specimen of phosphors was prepared for SEM / EDX (energy dispersive X-ray spectroscopy) by attaching to an aluminum stub as a thin layer of powders using adhesive carbon tapes. To prevent charging up, the samples were coated with palladium in an Emitech K575X Turbo Sputter Coater. SEM images were taken using a JEOL 5800LV microscope with an acceleration voltage of 20 kV. X-ray Spectra were collected for EDX chemical analysis using an INCA Penta FETx3 system, Oxford Instruments, UK. In order to calibrate the acquisition rate, a pure silicon standard sample was used.

4.6 Characterization in LED

LED samples were prepared with an InGaN LED chip in a 1 W package. The test samples of phosphor were mixed with silicone resin and placed in the LED packages. The mixing ratio was adjusted to the color point to be targeted. The wavelength of the LED was chosen either 400 nm or 445 nm for the purpose of the evaluations. The operation voltage was about 3.2 V at the operation current of 350 mA, which were varied to check the operation current dependences of LED performance. Spectral data were collected by the multichannel spectrometer with integrating sphere. LED efficacy, external quantum efficiency, color coordinates, CCT and CRI were evaluated with the method, which is explained as assessment parameters for white LEDs in section 2.4.

4.7 References

- 1 K. Narita, In Phosphor Handbook; Yen, W.; Shionoya, S.; Yamamoto, H., Eds.; CRC Press: Boca Raton, 2007, p. 341.
- 2 R. E. Dinnebier and S. J. L. Billinge, In Powder Diffraction : Theory and Practice, RSC Publishing, Cambridge, UK, 2008, p. 1.
- 3 J. K. Cockcroft and A. N. Fitch, In Powder Diffraction : Theory and Practice, RSC Publishing, Cambridge, UK, 2008, p. 25.
- 4 S. P. Thompson, J. E. Parker, J. Potter, T. P. Hill, A. Birt, T. M. Cobb, F. Yuan, and C. C. Tang, *Rev. Sci. Instrum.*, 2009, **80**, 075107.
- 5 J. K. Cockcroft and A. N. Fitch, In Powder Diffraction : Theory and Practice, RSC Publishing, Cambridge, UK, 2008, p. 46.
- 6 The Basic of Crystallography and Diffraction, Second Edition, Christopher Hammond, Oxford University press, 2001, p.228.
- 7 D. B. Williams and C. B. Carter, Transmission Electron Microscopy, A text book for materials science, Second Edition, Springer, New York, 2009
- 8 R. B. Von Dreele, In Powder Diffraction : Theory and Practice, RSC Publishing, Cambridge, UK, 2008, p. 266.
- 9 V. F. Nicolin and R. Cerny, *J. Appl. Crystallogr.*, 2002, **35**, 734.
- 10 K. Momma and F. Izumi, *J. Appl. Crystallogr.*, 2011, **44**, 1272.
- 11 R. Hoppe, *Zeitschrift für Kristallographie*, 1979, **150**, 23.
- 12 M. Nespolo, G. Ferraris, G. Ivaldi and R. Hoppe, *Acta Crystallogr., Sect. B: Struct. Sci.*, 2001, **57**, 652.
- 13 K. Narita, In Phosphor Handbook; Yen, W.; Shionoya, S.; Yamamoto, H., Eds.; CRC Press: Boca Raton, 2007, p. 923.
- 14 T. Yoshioka and M. Ogawa, In Phosphor Handbook; Yen, W.; Shionoya, S.; Yamamoto, H., Eds.; CRC Press: Boca Raton, 2007, p. 843.

Chapter 5 Red luminescence of $\text{Ca}_4(\text{PO}_4)_2\text{O}:\text{Eu}^{2+}$

The unique emission characteristics and the crystal structure of $\text{Ca}_4(\text{PO}_4)_2\text{O}:\text{Eu}^{2+}$ were studied. Considerably broad emission from 500 nm to 800 nm was measured at 77 K when the material was excited at 365 nm. Its crystal structure was refined using neutron diffraction, allowing precise and accurate oxygen positions to be determined. This enabled a relationship between the optical properties and the crystal structure crucial for achieving a large redshift of the $5d$ level of Eu^{2+} to be established, which is important to match the excitation energy band with near-UV or blue LED used for SSL. The importance of the high anion polarizability and the heavy distortion of the coordination polyhedron were also discussed.

5.1 Introduction

The optimum absorption of Eu-doped phosphate phosphors rarely matches the emission of blue LEDs. For example a series of $\text{ABPO}_4:\text{Eu}^{2+}$ type phosphors was reported, where in A is alkali metal and B is alkali earth metal.¹ While most of these are excited at UV and some at near-UV, none of them can be excited by blue light. Another series of alkali earth metal based on orthophosphate and pyrophosphate such as $(\text{Ca},\text{Sr})_2\text{P}_2\text{O}_7:\text{Eu}^{2+}$ and $(\text{Ca},\text{Sr})_3(\text{PO}_4)_2:\text{Eu}^{2+}$ were reported,² but again they were only excited in the UV. It was found out that the $\text{Ca}_4(\text{PO}_4)_2\text{O}:\text{Eu}^{2+}$ phosphor (hereafter referred to as $\text{TTCP}:\text{Eu}^{2+}$) showed red emission at room temperature being excited by blue light and considerably broad emission from 500 nm to 800 nm at 77 K by 365 nm UV light.³ It is important to understand the key factor which allows Eu^{2+} to have a large redshift in this material. Therefore neutron diffraction was conducted on this compound to determine the exact oxygen positions in its structure so that the crystal structure can be related to emission characteristics. It is reported that the importance of the high anion polarizability and the distortion of the coordination polyhedra around Eu^{2+} ion to tune the redshift of its $5d$ energy level. Figure 5-1 shows the $\text{CaO} - \text{SrO} - \text{P}_2\text{O}_5$ system phase diagram. The divalent metal of Ca and Sr forms solid solution phases in pyrophosphate of $(\text{Ca},\text{Sr})_2\text{P}_2\text{O}_7:\text{Eu}^{2+}$ or orthophosphate of $(\text{Ca},\text{Sr})_3(\text{PO}_4)_2:\text{Eu}^{2+}$. Pink colored area shows the phase coverage, which potentially contain isolated oxide ion such as oxy-apatite and tetra calcium (strontium) phosphate. It is unlikely that the phases in this area form solid solution phases.

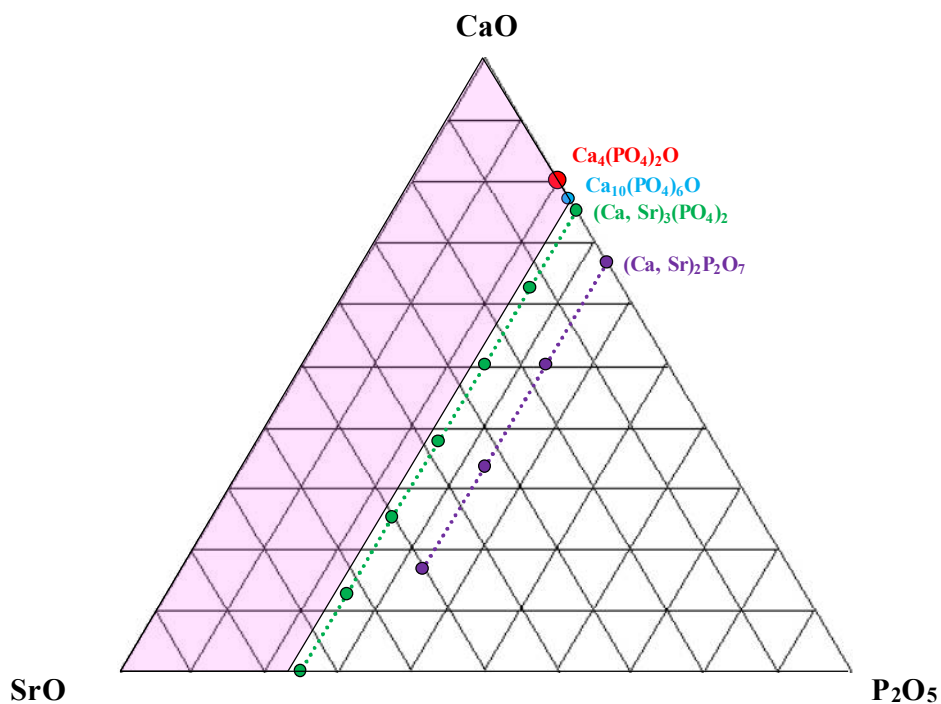


Figure 5-1 Phase diagram in $\text{CaO} - \text{SrO} - \text{P}_2\text{O}_5$ system with some phosphate phases.

5.2 Experimental

A phase pure sample of $\text{TTCP}:\text{Eu}^{2+}$ was synthesized by conventional solid-state reaction of CaCO_3 (Hakushin Chemicals), CaHPO_4 (Alfa Aesar) and Eu_2O_3 (Alfa Aesar). The ground mixtures of the raw materials were placed in alumina crucibles and heated in a reducing atmosphere of 5 % H_2 + 95 % N_2 in the temperature range of 1250-1300 °C for 10hrs. After the synthesis, the samples were ground into fine powders for characterization. Laboratory powder X-ray diffraction (PXRD) data were collected on a Bruker D8 diffractometer (Bragg – Brentano geometry) using $\text{Cu-K}\alpha$ radiation and a position-sensitive detector (LynxEye). Time of flight powder neutron diffraction data were recorded on the diffractometer HRPD, ISIS, Rutherford Appleton Laboratory. Structure refinement was performed by the Rietveld method using program GSAS.^{4,5} The crystal structure of $\text{TTCP}:\text{Eu}^{2+}$ was depicted in VESTA, in which the effective coordination number (ECoN) are also calculated.⁶ PL and PLE spectra at room temperature and 77 K were measured using a Horiba FluoroLog-3 spectrometer. The UV-vis reflectance spectra were measured using a PerkinElmer Lambda 750 spectrophotometer. To evaluate the band gap of TTCP, density functional theory (DFT) calculations with hybrid nonlocal exchange-correlation functional (HSE) were performed by applying the Vienna Ab initio Simulation Package (VASP) code. The electron-ion interaction was described by the projector augmented wave (PAW) method. The basis set cutoff was 400 eV.^{7,8,9}

5.3 Results

5.3.1 The structure refinement of $\text{Ca}_4(\text{PO}_4)_2\text{O}:\text{Eu}^{2+}$

The laboratory PXRD pattern agreed with JCPDS-ICDD-PDF no. 25-1137(space group: $P2_1$) for the tetra calcium phosphate. The crystal structure of TTCP was previously studied using single crystal X-ray diffraction by Dickens.¹⁰ The unit cell parameters were similar to that obtained in the previous work on the TTCP confirming the same phase had formed. In this work, neutron diffraction studies of $\text{TTCP}:\text{Eu}^{2+}$ has enabled us to refine more precise and accurate oxygen positions. Figure 5-2 shows the high quality of the Rietveld fits to the pattern obtained of $\text{TTCP}:\text{Eu}^{2+}$ using the monoclinic $P2_1$ structure. Table 5-1 shows structural parameters for $\text{TTCP}:\text{Eu}^{2+}$, including R indexes of $R_{wp} = 3.0$ % and $R_p = 4.2$ % by comparison with the value from previous work.¹⁰ The crystal structure is illustrated in Figure 5-3 and the atomic coordinates of TTCP are shown in Table 5-2.

The $\text{TTCP}:\text{Eu}^{2+}$ phosphor has eight Ca sites, all Ca sites are coordinated by seven oxygen atoms with an average bond length from 2.44 Å to 2.52 Å. Bond valence sums were calculated to confirm the proper coordination number (Table 5-3).¹¹ The four P sites are in PO_4 tetrahedra which are isolated from other PO_4 tetrahedra. The structure also contains two distinct oxide anions that are not part of a PO_4 tetrahedron (labeled O1 and O2).

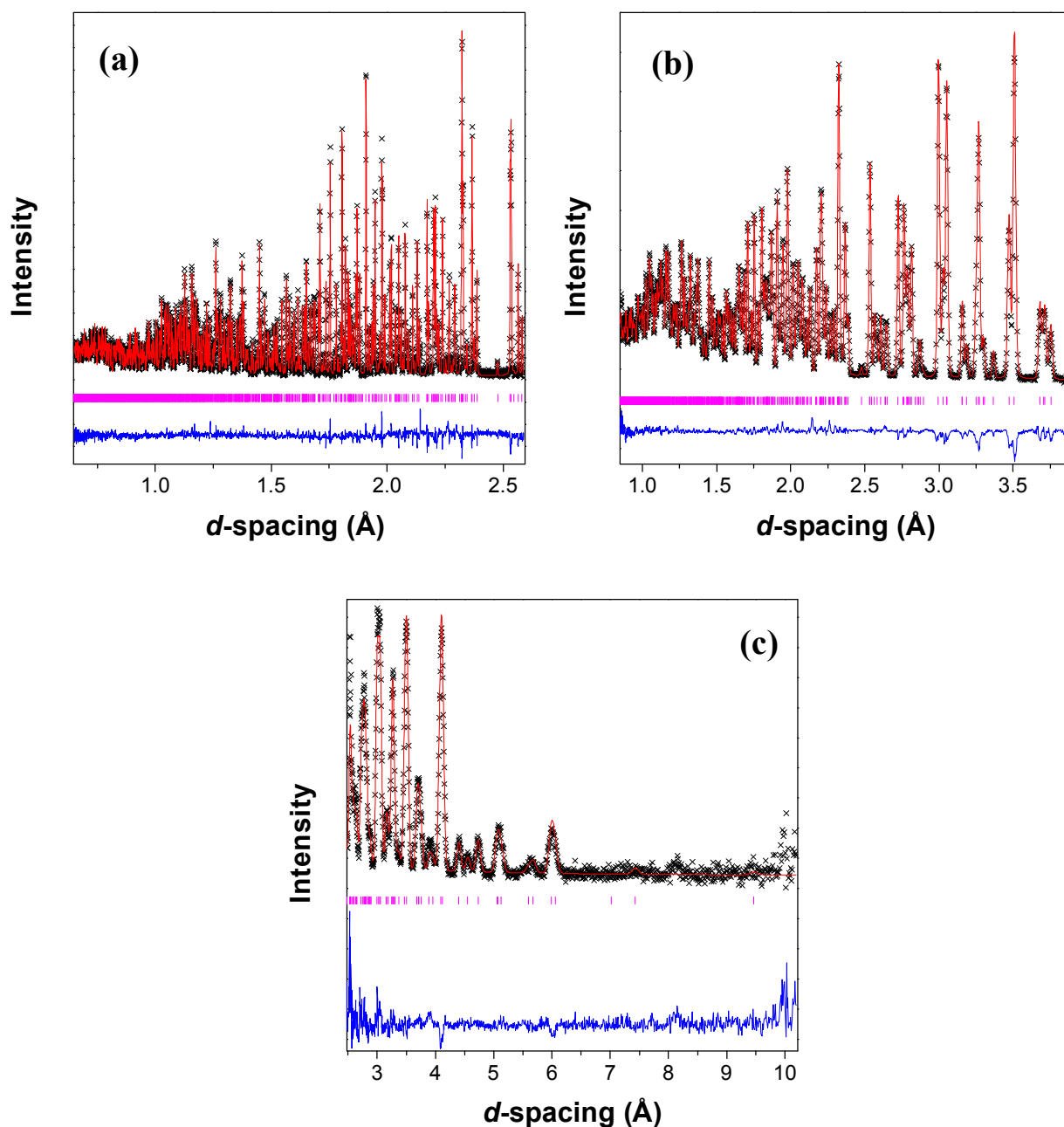


Figure 5-2 Diffraction patterns from the (a) backscattering, (b) 90° and (c) low angle banks of the HRPD diffractometer, fitted by the Rietveld method using the program GSAS. The crosses, and upper and lower continuous lines are the experimental, calculated and difference profiles, respectively. The vertical markers indicate the allowed Bragg reflections and the overall R_p , R_{wp} and χ^2 values are 4.2 %, 3.0 % and 6.1.

Table 5-1 Crystallographic data and structure refinement.

	This work	Previous work
Unit cell dimensions	$a = 7.01444(5) \text{ \AA}$ $b = 11.9792(1) \text{ \AA}$ $c = 9.46490(7) \text{ \AA}$ $\beta = 90.8915(4)^\circ$	$a = 7.023(1) \text{ \AA}$ $b = 11.986(4) \text{ \AA}$ $c = 9.473(2) \text{ \AA}$ $\beta = 90.90(1)^\circ$
Cell volume	$V = 795.22(1) \text{ \AA}^3$	$V = 797.3 \text{ \AA}^3$
Space group	$P2_1$	$P2_1$
R indexes	$R_{wp} = 3.0\%$	$R_p = 4.2\%$

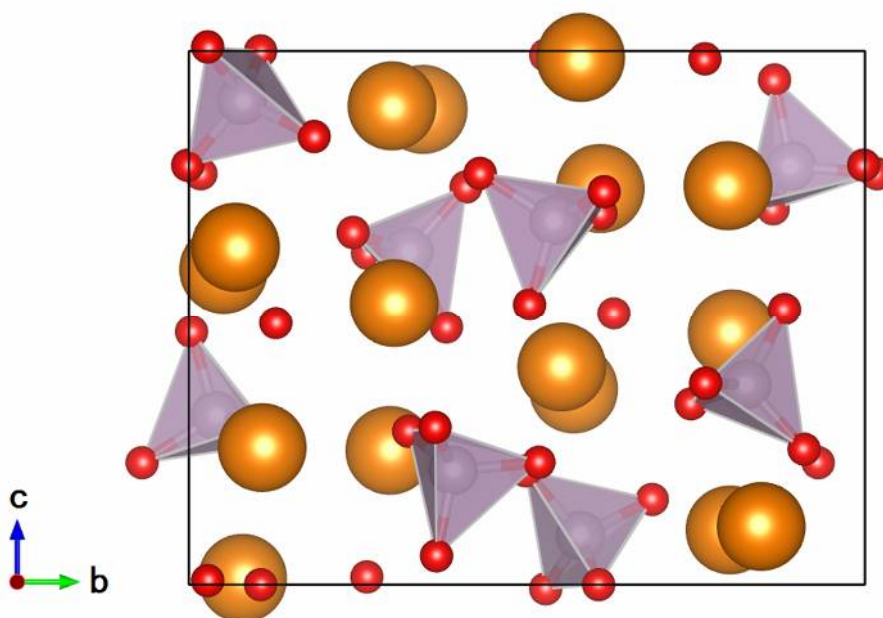


Figure 5-3 Schematic crystal structure illustration of $\text{TTCP}:\text{Eu}^{2+}$ projected onto the (100) plane. Ca, P and O atoms are shown as brown, mauve and red spheres.

Table 5-2 Atomic parameters of $\text{Ca}_4(\text{PO}_4)_2\text{O}$ with all sites in the refinement being set to be fully occupied.

Atom	Site	x	y	z
Ca1	2a	0.0284(4)	0.34615(28)	0.89136(36)
Ca2	2a	0.5330(4)	0.30061(26)	0.89780(35)
Ca3	2a	0.7641(5)	0.30377(26)	0.52772(32)
Ca4	2a	0.2672(5)	0.29716(26)	0.25170(37)
Ca5	2a	0.7429(5)	0.10839(29)	0.25671(32)
Ca6	2a	0.2503(6)	0.07927(27)	0.01167(36)
Ca7	2a	-0.0118(5)	0.06895(26)	0.63326(36)
Ca8	2a	0.5123(5)	0.05127(27)	0.59247(35)
O11	2a	0.7321(4)	0.51763(21)	0.22907(29)
O12	2a	0.6151(4)	0.32498(25)	0.28698(31)
O13	2a	0.9544(4)	0.36425(23)	0.29451(29)
O14	2a	0.7707(4)	0.36601(20)	0.05393(29)
O21	2a	0.2853(4)	0.40968(23)	0.74661(30)
O22	2a	0.0945(5)	0.26408(25)	0.62265(30)
O23	2a	0.4541(4)	0.24313(24)	0.66132(29)
O24	2a	0.3317(4)	0.38090(24)	0.48253(28)
O31	2a	0.2181(4)	0.00388(23)	0.47359(28)
O32	2a	0.0751(4)	0.11368(26)	0.26259(28)
O33	2a	0.4171(4)	0.10949(27)	0.30343(29)
O34	2a	0.2469(4)	-0.06924(23)	0.22820(30)
O41	2a	0.5874(4)	0.10649(24)	0.99957(29)
O42	2a	0.8375(4)	0.18523(22)	0.84083(30)
O43	2a	0.7161(4)	-0.00175(22)	0.78653(31)
O44	2a	0.9198(4)	0.02781(23)	1.00808(31)
O1	2a	0.2629(4)	0.26301(23)	0.01466(29)
O2	2a	0.7637(4)	0.12852(22)	0.49039(28)
P1	2a	0.7684(5)	0.39105(26)	0.21379(34)
P2	2a	0.2891(4)	0.32527(27)	0.62543(33)
P3	2a	0.2380(5)	0.03977(25)	0.31618(32)
P4	2a	0.7638(5)	0.07878(27)	0.90817(34)

Table 5-3 Bond valence sums of TTCP.

Bond	Distance (Å)	Bond Valence	Bond	Distance (Å)	Bond Valence
Ca1_O1	2.236(5)	0.483	Ca5_O2	2.227(4)	0.495
Ca1_O42	2.391(4)	0.318	Ca5_O32	2.331(5)	0.374
Ca1_O44	2.401(4)	0.309	Ca5_O33	2.334(5)	0.371
Ca1_O14	2.404(5)	0.307	Ca5_O21	2.389(5)	0.320
Ca1_O21	2.405(5)	0.306	Ca5_O41	2.651(4)	0.157
Ca1_O34	2.443(5)	0.276	Ca5_O12	2.761(5)	0.117
Ca1_O22	2.773(4)	0.113	Ca5_O44	2.846(4)	0.093
Total		2.113	Total		1.927

Bond	Distance (Å)	Bond Valence	Bond	Distance (Å)	Bond Valence
Ca2_O1	2.254(5)	0.460	Ca6_O1	2.203(4)	0.528
Ca2_O14	2.345(4)	0.360	Ca6_O41	2.392(5)	0.317
Ca2_O23	2.398(4)	0.312	Ca6_O44	2.398(5)	0.312
Ca2_O34	2.509(4)	0.231	Ca6_O11	2.400(4)	0.310
Ca2_O41	2.544(4)	0.210	Ca6_O14	2.633(4)	0.165
Ca2_O21	2.587(5)	0.187	Ca6_O34	2.714(4)	0.133
Ca2_O42	2.608(4)	0.177	Ca6_O32	2.722(4)	0.130
Total		1.938	Total		1.895

Bond	Distance (Å)	Bond Valence	Bond	Distance (Å)	Bond Valence
Ca3_O2	2.129(4)	0.645	Ca7_O2	2.180(5)	0.562
Ca3_O31	2.400(4)	0.310	Ca7_O31	2.360(4)	0.346
Ca3_O12	2.505(5)	0.234	Ca7_O11	2.418(4)	0.296
Ca3_O22	2.518(5)	0.226	Ca7_O22	2.456(5)	0.267
Ca3_O23	2.635(4)	0.164	Ca7_O43	2.559(5)	0.202
Ca3_O13	2.696(4)	0.139	Ca7_O13	2.576(4)	0.193
Ca3_O34	2.768(4)	0.115	Ca7_O42	2.642(4)	0.161
Total		1.833	Total		2.026

Bond	Distance (Å)	Bond Valence	Bond	Distance (Å)	Bond Valence
Ca4_O1	2.280(4)	0.429	Ca8_O2	2.225(5)	0.498
Ca4_O13	2.378(4)	0.329	Ca8_O43	2.395(5)	0.315
Ca4_O43	2.439(4)	0.279	Ca8_O31	2.403(4)	0.308
Ca4_O24	2.440(4)	0.278	Ca8_O23	2.425(5)	0.290
Ca4_O12	2.480(4)	0.250	Ca8_O24	2.427(4)	0.288
Ca4_O33	2.527(5)	0.220	Ca8_O11	2.459(4)	0.265
Ca4_O32	2.581(4)	0.190	Ca8_O33	2.891(5)	0.082
Total		1.977	Total		2.046

5.3.2 Optical properties of $\text{Ca}_4(\text{PO}_4)_2\text{O}:\text{Eu}^{2+}$

Figure 5-4 shows the PL and PLE spectra of TTCP: Eu^{2+} at 1 mol% doping with respect to Ca, excited at 465 nm and monitored at 700 nm at room temperature and 77 K. The sample obtained in this work showed red emission at room temperature. However further investigation revealed it emitted shorter wavelength of light when excited at 465 nm at 77 K. The obvious change in the emission spectrum shape was caused by a tremendous increase in the shoulder peak around 600 nm. Significant increased excitation at 350 nm is also observed, presumably due to different contributions from Eu^{2+} in the various coordination environments. Figure 5-5 displays the photograph of the body color and emissions of TTCP: Eu^{2+} . The photographs were taken under ambient light at room temperature, under 365 nm UV light at room temperature and 365 nm UV light at 77 K. The samples showed clear yellow emission colors at 77 K. The optimized PL and PLE spectra were measured for yellow emission at 550 nm and for red emission at 700 nm (Figure 5-6) at 77 K.

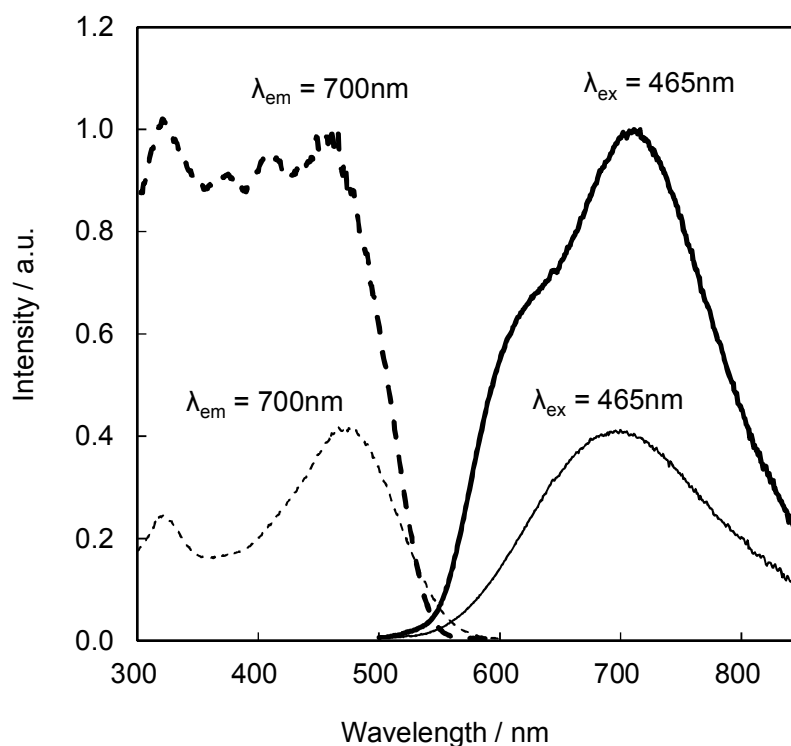


Figure 5-4 PL (solid line) and PLE (dashed line) spectra of TTCP activated with 1 mol% of Eu^{2+} , excitation for 700 nm emission at room temperature (thin curve) and 77 K (thick curve).

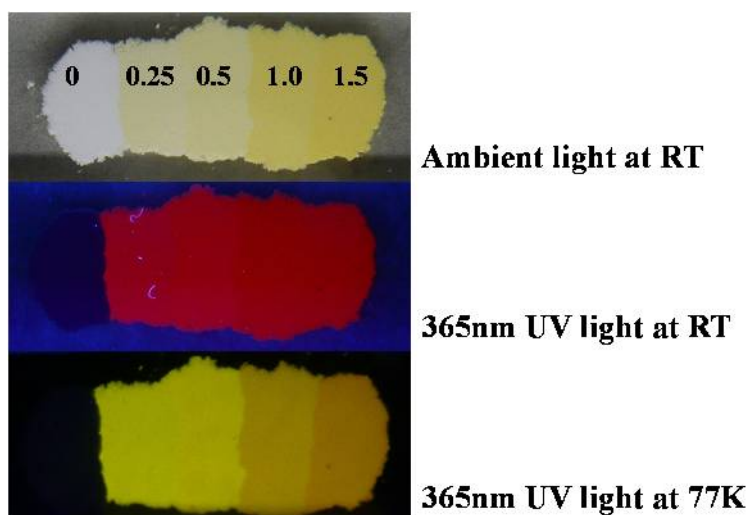


Figure 5-5 Series TTCP phosphor samples with different Eu doping levels viewed at room temperature and at 77 K. Eu contents are labelled in mol%.

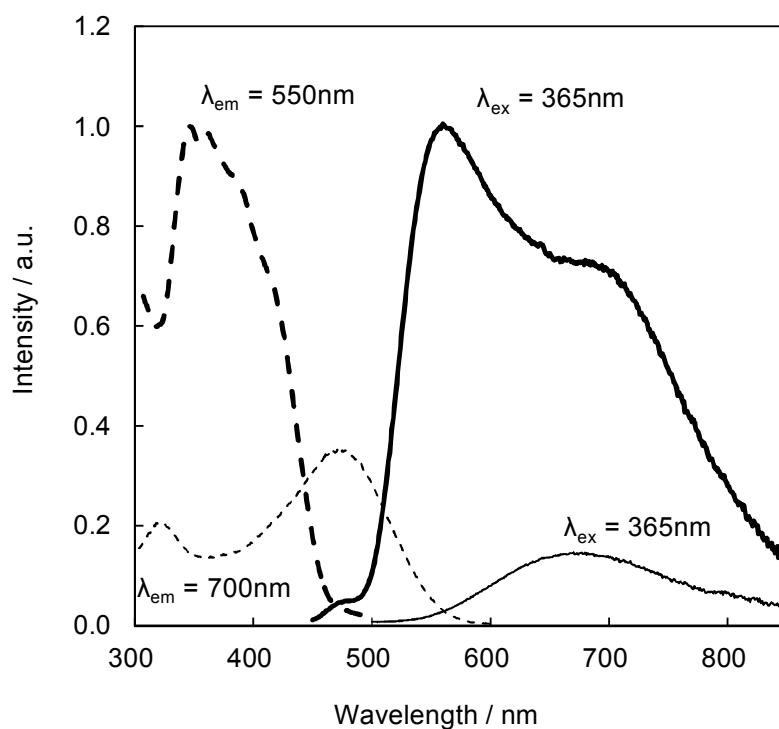


Figure 5-6 PL (solid line) and PLE (dashed line) spectra of TTCP activated with 1 mol% of Eu^{2+} , excited by 365 nm UV light at room temperature (thin curve) and 77 K (thick curve).

5.3.3 The absorption of $\text{Ca}_4(\text{PO}_4)_2\text{O}$

The diffuse reflection spectra of undoped and Eu-doped TTCP were measured, and their absorption spectra (K/S) derived with the Kubelka - Munk function is shown in the Figure 5-7. The Kubelka - Munk function, which is introduced as Equation 4-10 in chapter 4. The value of the optical band gap can be calculated by extrapolating the Kubelka - Munk function $F(R_\infty)$ to $K/S = 0$.¹² This gave a value of the optical band gap in the undoped TTCP, E_g , of about 6.2 eV, which appears sufficiently close to the computed band gap of 6.12 eV. The Calculated Density of States (DOS) is shown in Figure 5-8. According to Ref. 13, the calculation of the bandgaps based on the HSE agreed well with the experimental value up to around 6 eV, and within 0.5 eV deviation can be expected from the calculation.

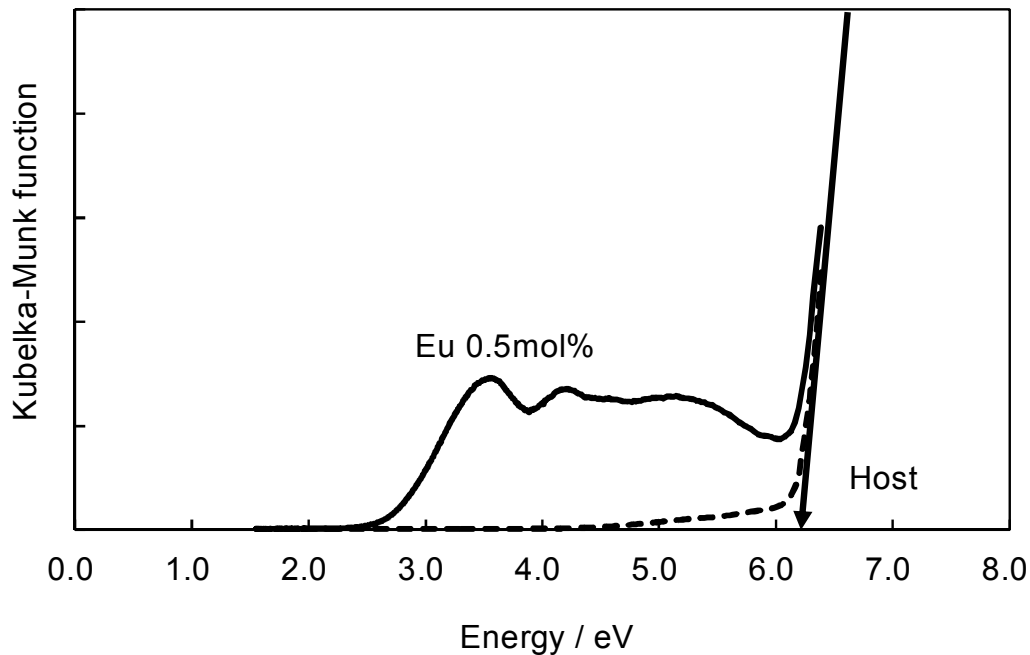


Figure 5-7 Absorption spectra of an undoped sample (dashed line) and a sample doped with 0.5 mol% of Eu (solid line).

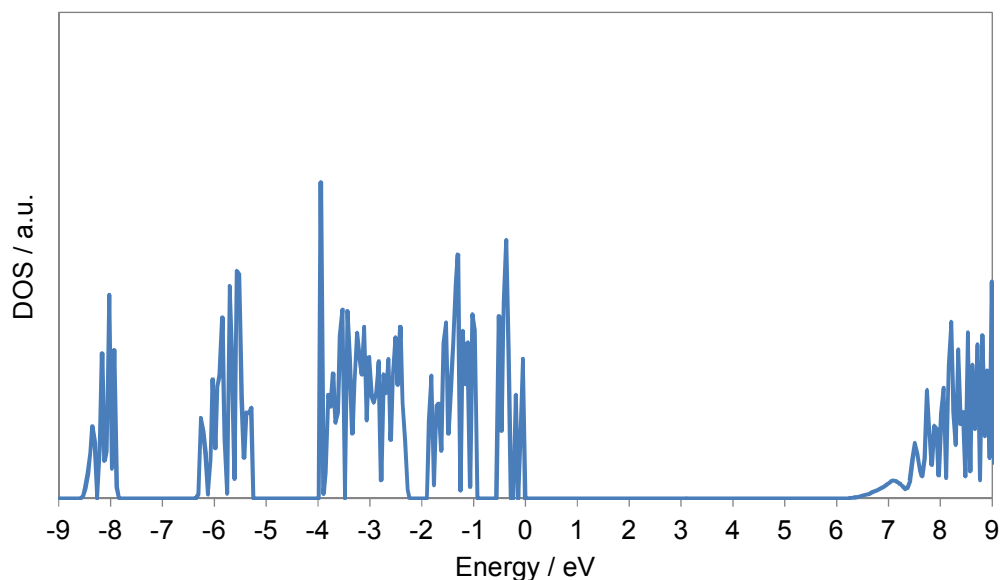


Figure 5-8 Calculated DOS of TTCP. The vertical dashed bars indicate the end of the fundamental band gap.

5.4 Discussion

It is crucial to understand the relation between crystal structures and emission characteristics to develop new phosphors for SSL, since a large redshift of the $5d$ level of $\text{Ce}^{3+}/\text{Eu}^{2+}$ enables to match excitation bands of phosphors for near-UV/blue LED excitation. A variety of Eu^{2+} doped phosphors were reanalyzed in terms of their redshift, centroid shift and crystal field splitting.¹⁴ The redshift is the combined effect of the centroid shift and the crystal field splitting. The centroid shift is a downward shift of an average energy of the five $5d$ levels of Eu^{2+} ion relative to the degenerated $5d$ states of the isolated Eu^{2+} ion. The crystal field splitting is the energy difference between the lowest and highest $5d$ level. Doping Eu^{2+} into a crystal lattice lowers the energy of the $5d$ levels through the centroid shift, which can be large when the polarizability of the anions becomes large (so-called, *nephelauxetic effect*).¹⁵ This means that the silicates, aluminates and simple oxides are mostly promising host candidates. As seen in Ref.14, this is the reason why there are few examples of phosphate phosphors for blue LEDs.

When $\text{TTCP}:\text{Eu}^{2+}$ is excited by 365 nm light at 77 K, its emission lies over 300 nm range from green to deep red. It is of great interests to know why $\text{TTCP}:\text{Eu}^{2+}$ has a large redshift unlike other phosphate phosphors and how eight Ca sites for Eu^{2+} can be differentiated in $\text{TTCP}:\text{Eu}^{2+}$. In order to compare the emission between $\alpha\text{-Ca}_3(\text{PO}_4)_2:\text{Eu}^{2+}$ and $\text{TTCP}:\text{Eu}^{2+}$, the emission of $\text{TTCP}:\text{Eu}^{2+}$ under the 365 nm excitation at 77 K was deconvoluted into eight Gaussian components based on the energy scale, then converted it into wavelength scale

as shown in Figure 5-9. $\alpha\text{-Ca}_3(\text{PO}_4)_2:\text{Eu}^{2+}$ has a emission peak at 488 nm,² whereas TTCP: Eu^{2+} appears to have sites emitting up to 824 nm. Since it is known that deep red emission can be seen in $\text{CaO}:\text{Eu}^{2+}$,¹⁶ the isolated oxide ion can be more polarizable than oxygen in PO_4 . $\text{Ca}_4(\text{PO}_4)_2\text{O}$ contains isolated O^{2-} ions whereas $\text{Ca}_3(\text{PO}_4)_2$ does not and it is likely that this is responsible for the large centroid shift which enables $\text{Ca}_4(\text{PO}_4)_2\text{O}$ to emit deep red light. Structure comparison between $\alpha\text{-Ca}_3(\text{PO}_4)_2$ and $\text{Ca}_4(\text{PO}_4)_2\text{O}$ are shown in Figure 5-10 indicating isolated oxide ion.

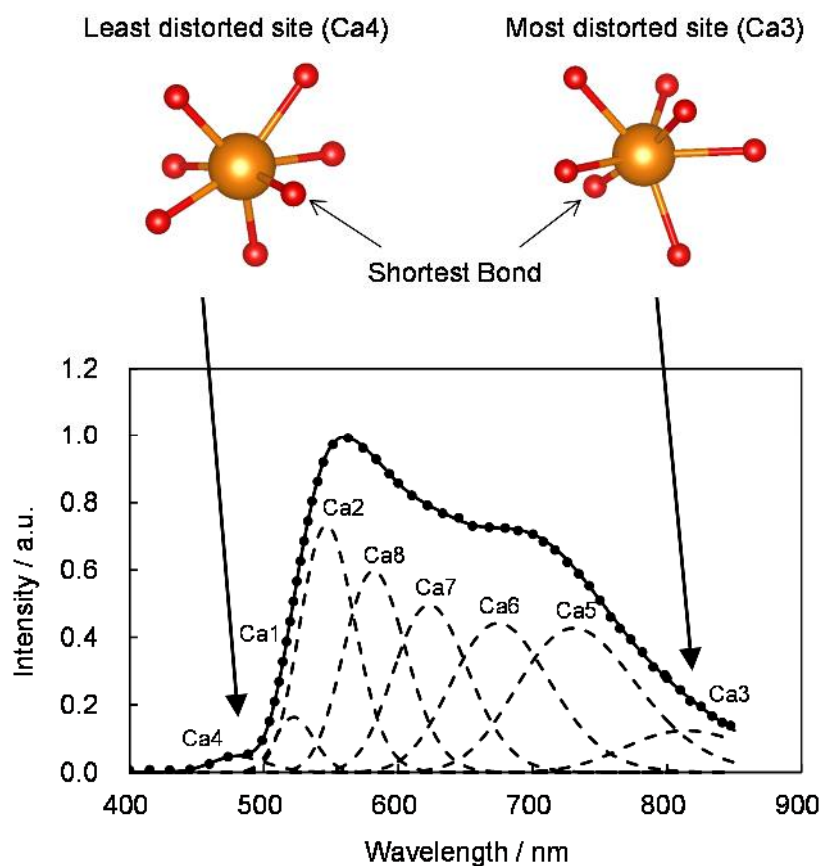


Figure 5-9 Deconvoluted emission spectra of TTCP: Eu^{2+} . Observed (dotted line), fitted curve (solid line) and deconvoluted Gaussian components for 8 Ca sites (dashed line) with the coordination geometries representing least and most distorted Ca sites.

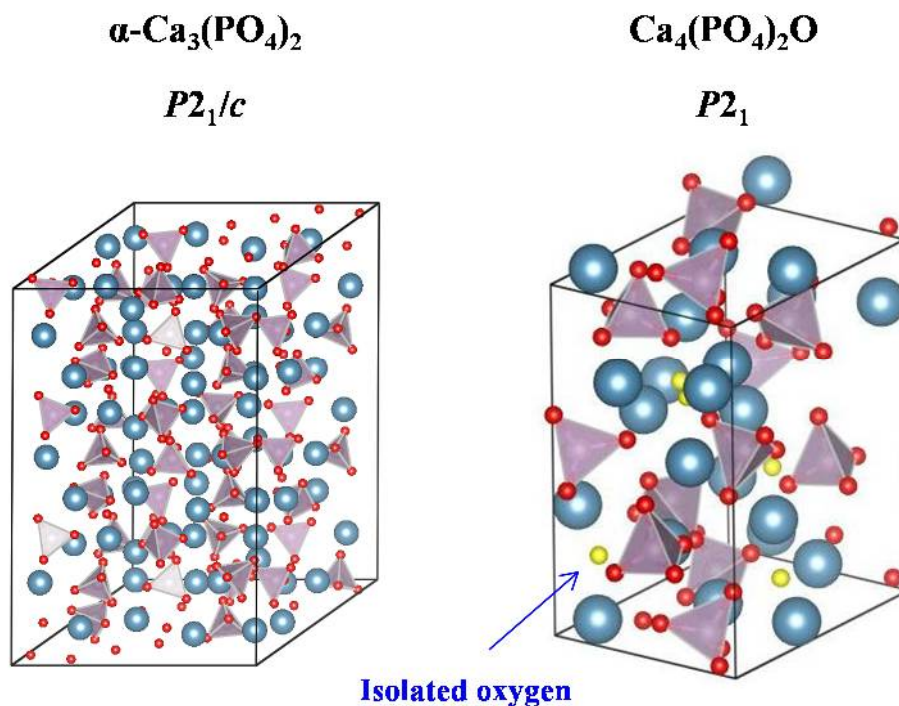


Figure 5-10 Structure comparison between $\alpha\text{-Ca}_3(\text{PO}_4)_2$ and $\text{Ca}_4(\text{PO}_4)_2\text{O}$ indicating isolated oxygen.

The other major effect on reducing the $4f\text{-}5d$ gap is the crystal field splitting. This is dictated largely by the type and size of anion coordination polyhedron around Eu^{2+} .¹⁷ The all eight Ca sites in $\text{TTCP}:\text{Eu}^{2+}$ are coordinated by seven oxygen atoms with an average bond length from 2.44 Å to 2.52 Å. The average bond lengths and formal coordination number seem not to vary much between the eight Ca sites. However the smallest bond lengths from the each Ca site to the closest anion vary from 2.13 Å to 2.28 Å, which are significantly smaller than the average. It is noted that all the Ca sites have an isolated O^{2-} ion as the closest anion. Being coordinated by an isolated O^{2-} ion is apparently not enough to emit deep red light since all eight Ca sites have isolated O^{2-} ion as a ligand. However isolated O^{2-} ion can get closer to the doping site enabling the Eu-O_x polyhedron to distort. The distortion around Eu and the polarizability of O^{2-} ion can be crucial to determine the emission color. Some models were suggested to explain the different emissions on phosphate phosphors such as $\text{Ba}_{(3-x)}\text{Sr}_x\text{Lu}(\text{PO}_4)_3:\text{Eu}^{2+}$ and $\text{Ca}_{3-x}\text{Sr}_x(\text{PO}_4)_2:\text{Eu}^{2+}$.^{18,19} In their discussions, larger neighbouring-cation decreases Eu-O bond lengths as a result of higher stress from larger cations when larger cations replaced smaller ions. That results in strengthening the Eu^{2+} crystal field splitting, generating the red-shifts. This idea can then be extended to TTCP phosphor. When comparing neighbouring-cations between Ca3 and Ca4 site, Ca3 site has two Ca atoms and three P atoms within 3.5 Å range, whereas Ca4 has one Ca atom and one P atom. The Ca3 site can therefore be considered to be more compressive than Ca4 site.

Analyzing the detailed link between structure and the emission performance of $\text{TTCP}:\text{Eu}^{2+}$ deeply enhances our understanding of the unique properties of this material. When discussing metal sites heavily distorted from ideal

symmetry, the idea of ECoN is useful.²⁰ To deal with structures containing highly distorted coordination polyhedron, ECoN is defined as the sum of the bond weights, which is calculated from the each bond length and smallest bond length in the coordination polyhedron.^{20,21} ECoN decreases its value as the shortest bond length becomes short. The following discussion is based on the assumption that eight Ca sites are radiative for Eu^{2+} since a significant emission color change was not observed under even shorter excitation wavelength of 254 nm at 77 K.

Normally the site with smaller value in coordination number is more compressed and places higher chemical pressure on the dopant. Taking into account of the deviation in bond length from the average, ECoN can indicate the degree of distortion and stress in the polyhedron. When one Ca site has smaller ECoN in TTCP, the Eu in that site can feel stronger crystal field than in larger ECoN sites. It can be linked to the site that can show longer wavelength emission. Thus, the calculated ECoNs on eight Ca sites were assigned to deconvoluted emission peak positions as shown in Figure 5-11. A clear, close to linear, trend was observed between the ECoNs and the peak positions. The trend between the emission peak positions and the shortest bond lengths on each Ca site was further from linear behavior than that with respect to the ECoN numbers and was therefore not considered as an accurate guide to this behavior. It should be noted that eight Ca sites have significantly different ECoNs regardless of their formal coordination numbers of seven or eight by taking into account the distortion of the coordination polyhedron attributed to less uniform charge distributions.

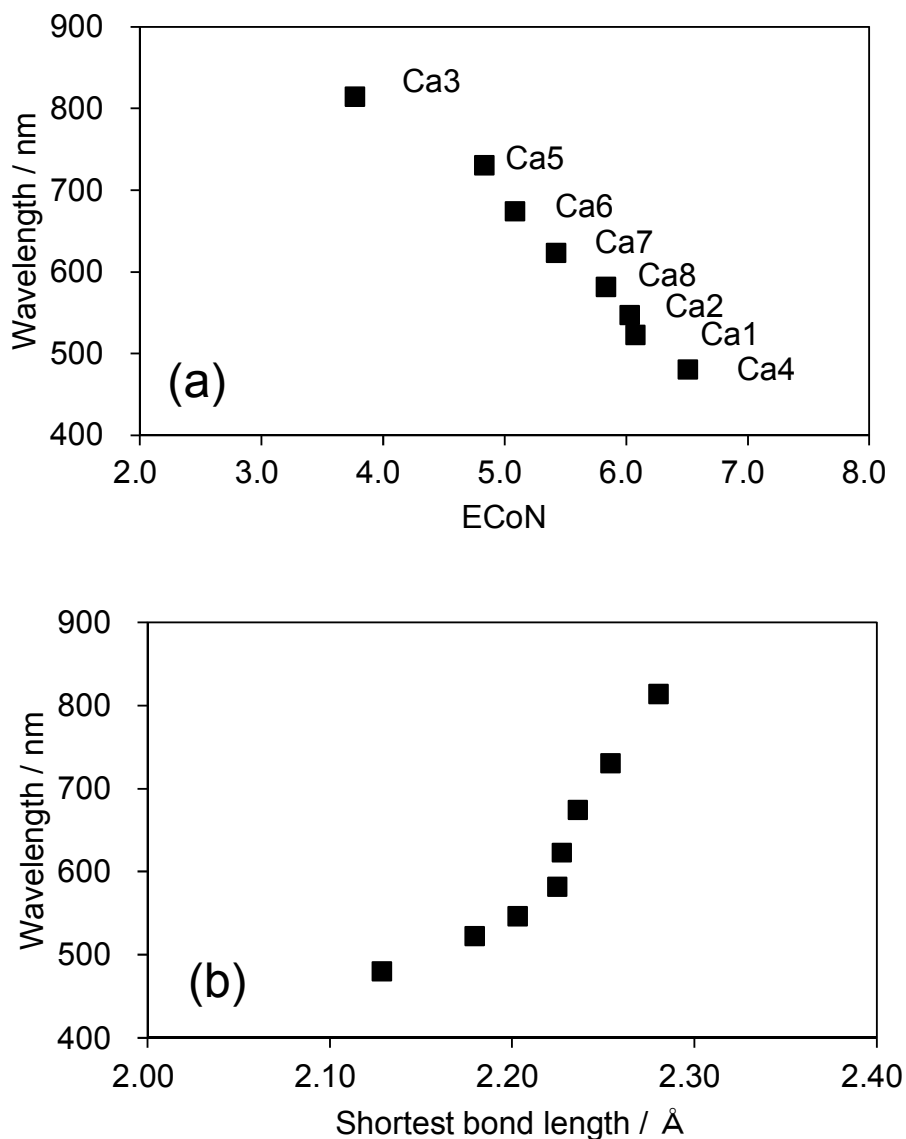


Figure 5-11 Plot of the assigned emission peak positions for the eight Ca sites and their calculated ECoNs, showing a nearly linear relationship (a) and the same plot against the shortest bond length (b).

The different thermal quenching on each Ca site is another interesting feature of $\text{TTCP}:\text{Eu}^{2+}$. As shown in Figure 5-6, $\text{TTCP}:\text{Eu}^{2+}$ has a higher emission peak intensity at 560 nm than at 670 nm, being excited by the 365 nm light at 77 K. However, as the temperature increases to ambient conditions the emission peak at 560 nm decreases its peak intensity rapidly showing much stronger thermal quenching than at 670 nm. This is the opposite of what would be expected from the conventional idea on configurational coordinate diagram (CCD), wherein thermal quenching of PL become stronger when the transversal offset between the ground-state parabola and the excited state parabola becomes larger, leading to stronger thermal quenching of longer emission wavelengths.²²

The stronger thermal quenching of shorter wavelength emission can be explained on the basis of auto-ionization from the $5d$ level of Eu^{2+} to the conduction band, as discussed in $\text{SrAl}_2\text{O}_4:\text{Eu}^{2+}$, Dy^{3+} phosphor,²³ wherein blue emission have stronger thermal quenching (little luminescence at room temperature) than green emission. Similarly, the degree of auto-ionization can be considered on each Ca site. The schematic energy diagram for $\text{TTCP}:\text{Eu}^{2+}$ is shown in Figure 5-12 representing two typical sites with the yellow emission at the peak position of 560 nm and the red emission at the peak position of 670 nm. The evaluated band gap of $\text{TTCP}:\text{Eu}^{2+}$ from the Kubelka-Munk function is about 6.2 eV. Assuming the inert $4f$ ground states of each Eu^{2+} are much less affected by the crystal field than excited $5d$ levels, the $4f$ ground states lie at more or less the same energy level in the band gap. Taking into account the excitation peaks at 346 nm and 466 nm, the $5d$ energy level of Eu^{2+} on the 560 nm emission site can be located at a much shallower level than that of 670 nm. A smaller energy gap between the $5d$ energy level of Eu^{2+} and the bottom of conduction band on the 560 nm emission site should therefore be expected compared to the 670 nm emission site. These energy gaps between the $5d$ energy level of Eu^{2+} and the bottom of conduction band on each emission site can affect the degree of auto-ionization. As shown in Dorenbos' empirical formula, $\Delta E = T_{0.5}/680$ eV, where $T_{0.5}$ is the quenching temperature at which the emission intensity has dropped to 50 % of the low temperature value and ΔE is the energy barrier, a several sub-eV difference may be significant for thermal quenching. Thus, the energy difference value of 0.92 eV between 346 nm excitation (3.58 eV) and 466 nm excitation (2.66 eV) can be crucial to determining the degree to quenching observed.²⁴

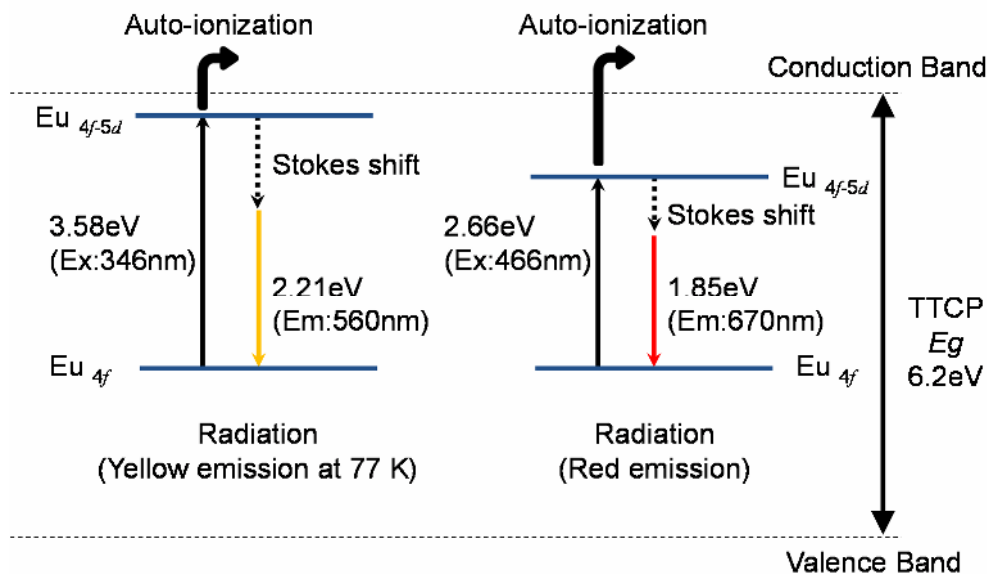


Figure 5-12 Schematic energy diagram of $\text{TTCP}:\text{Eu}^{2+}$ representing yellow emission (560 nm) and red emission (670 nm).

5.5 Summary

The unique emission spectra of the TTCP: Eu^{2+} phosphor at 77 K was reported, which is considerably broad covering from 500 nm to 800 nm. Powder neutron diffraction was fitted to precisely locate the oxygen position in the crystal structure of TTCP: Eu^{2+} , and quite distorted coordination polyhedron around Ca sites were revealed. The relation between the crystal structure and emission spectra was discussed and the importance of the anion status and the distortion of the coordination polyhedron were highlighted. The idea of the ECoN was introduced for differentiating the eight Ca sites in the TTCP: Eu^{2+} structure relating to the broad emission spectra. The different thermal quenching on the representing two Ca sites was discussed and attributed to the degree of auto ionization.

5.6 References

- 1 M. E. Hannah, A. Piquette, M. Anc, J. McKittrick, J. Talbot, J. K. Han and K. C. Mishra, *ECS Trans.*, 2012, **41**, 19.
- 2 C. C. Lagos, *J. Electrochem. Soc.: SOLID STATE SCIENCE*, 1970, **117**, 1189.
- 3 N. Komuro, M. Mikami, P. J. Saines and A. K. Cheetham, *J. Lumin.*, 2015, **162**, 25.
- 4 A.C. Larson and R. B. Von Dreele, "General Structure Analysis System (GSAS)", Los Alamos National Laboratory Report LAUR 86-748, 1994.
- 5 B. H. Toby, *J. Appl. Crystallogr.*, 2001, **34**, 210.
- 6 K. Momma and F. Izumi, *J. Appl. Crystallogr.*, 2011, **44**, 1272.
- 7 G. Kresse and J. Furthmuller, *Phys. Rev. B*, 1996, **54**, 11169.
- 8 G. Kresse and D. Joubert, *Phys. Rev. B*, 1999, **59**, 1758.
- 9 A. V. Krukau, O.A. Vydrov, A. F. Izmaylov and G. E. Scuseria, *J. Chem. Phys.*, 2006, **125**, 224106.
- 10 B. Dickens, W. E. Brown, G. J. Kruger and J. M. Stewart, *Acta Crystallogr., Sect. B: Struct. Sci.*, 1973, **B29**, 2046.
- 11 R. E. Brese and M. O'Keeffe, *Acta Crystallogr., Sect. B*, 1991, **B47**, 192.
- 12 C. J. Duan, A. C. A. Delsing and H. T. Hintzen, *Chem. Mater.*, 2009, **21**, 1010.
- 13 F. Tran and P. Blaha, *Phys. Rev. Lett.*, 2009, **102**, 226401.
- 14 P. Dorenbos, *J. Lumin.*, 2003, **104**, 239.
- 15 M. Mikami, *ECS J. Solid State Sci. Technol.*, 2013, **2**, R3048.
- 16 N. Yamashita, *J. Electrochem. Soc.*, 1993, **140**, 840.
- 17 P. Dorenbos, *J. Alloys Compounds*, 2002, **341**, 156.
- 18 Z. Wang, Z. Xia, M. S. Molokeev, V. V. Atuchin and Q. L. Liu, *Dalton Trans.*, 2014, **43**, 16800.
- 19 H. Ji, Z. Huang, Z. Xia, M. S. Molokeev, V. V. Atuchin and S. Huang, *Inorg. Chem.*, 2014, **53**, 11119.
- 20 M. Nespolo, G. Ferraris, G. Ivaldi and R. Hoppe, *Acta Crystallogr., Sect. B: Struct. Sci.*, 2001, **57**, 652.
- 21 R. Hoppe, S. Voigt, H. Glaum, J. Kissel, H. P. Muller and K. Bernet, *J. Less-Common. Met.*, 1989, **156**, 105.
- 22 G. Blasse and B. C. Grabmaier, *Luminescent Materials*, Springer, Berlin, 1994.
- 23 J. Ueda, T. Nakanishi, Y. Katayama and S. Tanabe, *Phys. Status Solidi C*, 2012, **9**, 2322.
- 24 P. Dorenbos, *Condens. Matter.*, 2005, **17**, 8103.

Chapter 6 Red luminescence of $\text{Sr}_4(\text{PO}_4)_2\text{O}:\text{Eu}^{2+}$

The deep red phosphor $\text{Sr}_4(\text{PO}_4)_2\text{O}:\text{Eu}^{2+}$, which has an excitation peak around 450 nm for blue LED applications, is reported. This behavior is unusual for most phosphate phosphors. The crystal structure of $\text{Sr}_4(\text{PO}_4)_2\text{O}:\text{Eu}^{2+}$ is found to be monoclinic $P2_1$ and isotypic with $\text{Ca}_4(\text{PO}_4)_2\text{O}:\text{Eu}^{2+}$, which was discussed in Chapter 5. $\text{Sr}_4(\text{PO}_4)_2\text{O}:\text{Eu}^{2+}$ has a larger lattice volume than $\text{Ca}_4(\text{PO}_4)_2\text{O}:\text{Eu}^{2+}$, but their emission and excitation spectra at room temperature are very similar. The key factors are discussed for achieving a large redshift of the $5d$ levels of Eu^{2+} ion in order to emit red light. In particular, the importance of the high anion polarizability and the heavy distortions of the metal coordination polyhedra are reconfirmed, including the effective coordination number. Importantly, $\text{Sr}_4(\text{PO}_4)_2\text{O}:\text{Eu}^{2+}$ lacks the yellow emission at 77 K, which is found in $\text{Ca}_4(\text{PO}_4)_2\text{O}:\text{Eu}^{2+}$. The differences in thermal quenching behavior for Eu^{2+} dopants in $\text{Sr}_4(\text{PO}_4)_2\text{O}:\text{Eu}^{2+}$ and $\text{Ca}_4(\text{PO}_4)_2\text{O}:\text{Eu}^{2+}$ are attributed to the degree of auto/photo-ionization due to differences in the band gaps of these compounds. The importance of the large band gap of the host lattice in avoiding non-radiative processes of energy relaxation was confirmed.

6.1 Introduction

The optimum absorption of Eu-doped phosphate phosphors rarely matches the emission of blue LEDs. Lagos reported the behavior of $\alpha\text{-Sr}_2\text{P}_2\text{O}_7:\text{Eu}^{2+}$ and $\alpha\text{-Sr}_3(\text{PO}_4)_2:\text{Eu}^{2+}$ as blue phosphors and $\alpha\text{-Ca}_3(\text{PO}_4)_2:\text{Eu}^{2+}$ as a green phosphor for UV excitation.¹ $\text{CaZr}(\text{PO}_4)_2:\text{Eu}^{2+}/\text{Eu}^{3+}$ was also reported for deep UV excitation.² However these materials are poorly matched to blue LEDs. In Chapter 5, $\text{TTCP}:\text{Eu}^{2+}$ was introduced, which has the longest excitation wavelength amongst phosphate systems, emitting deep red light at room temperature and considerably broad emission from 500 nm to 800 nm at 77 K. The relationship between the crystal structure and the unique emission characteristics of $\text{TTCP}:\text{Eu}^{2+}$ was discussed, differentiating the eight Ca sites. The importance of the high anion polarizability and the heavy distortions of the coordination polyhedra were also highlighted. In this chapter, the crystal structure and the emission characteristics of $\text{Sr}_4(\text{PO}_4)_2\text{O}:\text{Eu}^{2+}$ (hereafter referred to as $\text{TTSP}:\text{Eu}^{2+}$) were discussed as a new red phosphor well matched to blue LEDs. Despite previously reported difficulties in the synthesis of $\text{Sr}_4(\text{PO}_4)_2\text{O}$ leading to the formation of an apatite phase,³ $\text{Sr}_4(\text{PO}_4)_2\text{O}:\text{Eu}^{2+}$ was obtained somehow by optimizing synthesis condition in this work. $\text{Sr}_4(\text{PO}_4)_2\text{O}$ is chemically stable under ambient condition without reacting with moisture. The crystal structure of $\text{TTSP}:\text{Eu}^{2+}$ is isotopic with the structure of $\text{TTCP}:\text{Eu}^{2+}$. The emission efficiency of $\text{Sr}_4(\text{PO}_4)_2\text{O}:\text{Eu}^{2+}$ is not high due to non-radiative relaxation, which is attributed to photo-ionization, as discussed later in this chapter. However, as the key factors that allow Eu^{2+} to exhibit a large redshift in phosphors, crystallographic environment are discussed by comparing the anion polarizability and the distortions of the coordination polyhedra around Eu^{2+} in $\text{TTSP}:\text{Eu}^{2+}$ and $\text{TTCP}:\text{Eu}^{2+}$. The determining factor for the radiative/non-radiative energy relaxation processes in $\text{TTSP}:\text{Eu}^{2+}$ and $\text{TTCP}:\text{Eu}^{2+}$ was revealed by comparing their band gaps. Figure 6-1 shows the CaO - SrO - P_2O_5 system phase diagram with TTSP phase, which is in the area potentially containing isolated oxide ion.

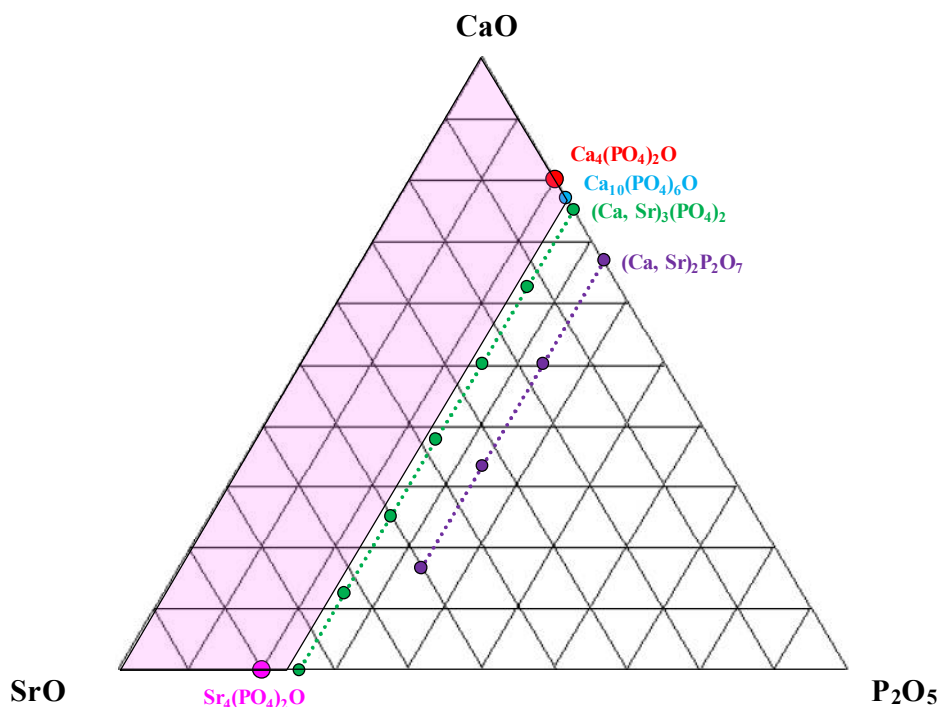


Figure 6-1 Phase diagram in CaO - SrO - P_2O_5 system with TTSP phase.

6.2 Experimental

A sample of $\text{TTSP}:\text{Eu}^{2+}$ was synthesized by conventional solid-state reaction of SrCO_3 (Hakushin Chemicals), SrHPO_4 (Alfa Aesar) and Eu_2O_3 (Alfa Aesar). Stoichiometric mixtures of the raw materials were placed in alumina crucibles and heated in a reducing atmosphere of 5 % H_2 + 95 % N_2 at 1450 °C for 5 hrs. After the synthesis, the samples were ground into fine powders for characterization. Synchrotron X-ray diffraction data were collected on beamline I11 at the Diamond Light Source facility in the UK using a wavelength of 0.82713 Å.⁴ Structure refinement was performed by the Rietveld method using the program GSAS.^{5,6} The crystal structure of $\text{TTSP}:\text{Eu}^{2+}$ was depicted in VESTA, in which the effective coordination numbers (ECoNs) were also calculated.⁷ PL and PLE spectra at room temperature were measured using a JASCO FP-6500 spectrometer and at 77 K using a Horiba FluoroLog-3 spectrometer. The UV-vis reflectance spectra were measured using a PerkinElmer Lambda 750 spectrophotometer. To evaluate the band gap of TTSP, density functional theory (DFT) calculations with a hybrid nonlocal exchange-correlation functional (HSE) were performed using the Vienna Ab initio Simulation Package (VASP) code. The electron-ion interaction was described by the projector augmented wave (PAW) method. The basis set cutoff was 400 eV.^{8,9,10}

6.3 Results and discussion

6.3.1 The structure refinement of $\text{Sr}_4(\text{PO}_4)_2\text{O}:\text{Eu}^{2+}$

The crystal structure of $\text{TTSP}:\text{Eu}^{2+}$ was originally reported as orthorhombic in space group $P222_1$ by Bauer.¹¹ The structure in this work was found to be a monoclinic, having space group $P2_1$ slightly distorted from $P222_1$, and is isotypic with the structure of $\text{TTCP}:\text{Eu}^{2+}$. Figure 6-2 shows the high quality of the Rietveld fit to the X-ray synchrotron powder diffraction pattern obtained of $\text{TTSP}:\text{Eu}^{2+}$ using the monoclinic $P2_1$ structure. The refinement using the orthorhombic $P222_1$ structure showed worse fits. Rietveld refinements revealed that the sample contained a relatively small amount of a $\text{Sr}_{10}(\text{PO}_4)_6\text{O}$ impurity, 10.1(6) % by weight. However, since $\text{Sr}_{10}(\text{PO}_4)_6\text{O}:\text{Eu}^{2+}$ is unable to be excited by visible light, this factor is negligible for this discussion of the optical properties of $\text{Sr}_4(\text{PO}_4)_2\text{O}:\text{Eu}^{2+}$.¹² Table 6-1 shows structural parameters for $\text{TTSP}:\text{Eu}^{2+}$, including R indexes of $R_{wp} = 9.2$ % and $R_p = 7.2$ %, and compares them with the parameters of $\text{TTCP}:\text{Eu}^{2+}$ from the previous work. $\text{TTSP}:\text{Eu}^{2+}$ has a monoclinic structure in space group $P2_1$ with lattice parameters $a = 7.390703(9)$ Å, $b = 12.58826(2)$ Å, $c = 9.82929(1)$ Å and $90.5797(1)^\circ$. The crystal structure is illustrated in Figure 6-3 and the atomic coordinates of are shown in Table 6-2. Seven of the Sr sites are coordinated by seven oxygen atoms with an average bond length from 2.60 Å to 2.68 Å, and one Sr site (Sr8) is coordinated by six oxygen atoms with an average bond length of 2.54 Å. The refined sample contained 0.5 mol% Eu^{2+} , but it was not possible to determine the distribution of Eu^{2+} ions over the cation sites by structural refinement. Bond valence sums were calculated to confirm the proper coordination numbers and oxidation states.¹³ Bond distances from the divalent cations in the TTSP structure, the bond valence sums and ECoNs are listed in Table 6-3. The four P sites are in PO_4 tetrahedra which are isolated from other PO_4 tetrahedra. The structure also contains two distinct oxide anions that are not part of a PO_4 tetrahedron (labeled O17 and O18).

Table 6-1 Crystallographic data and structure refinement for $\text{TTSP}:\text{Eu}^{2+}$.

	TTSP (This work)	TTCP (Previous work)	TTSP (Bauer)
Unit cell dimensions	$a = 7.390703(9)$ Å	$a = 7.01444(5)$ Å	$a = 7.38$ Å
	$b = 12.58826(2)$ Å	$b = 11.9792(1)$ Å	$b = 12.57$ Å
	$c = 9.82929(1)$ Å	$c = 9.46490(7)$ Å	$c = 9.79$ Å
	$\beta = 90.5797(1)^\circ$	$\beta = 90.8915(4)^\circ$	$\beta = 90^\circ$
Cell volume	$V = 914.431(2)$ Å ³	$V = 795.22(1)$ Å ³	$V = 908.19$ Å ³
Space group	$P2_1$	$P2_1$	$P222_1$
R indexes	$R_{wp} = 9.2\%$	$R_p = 7.2\%$	$\chi^2 = 1.4$

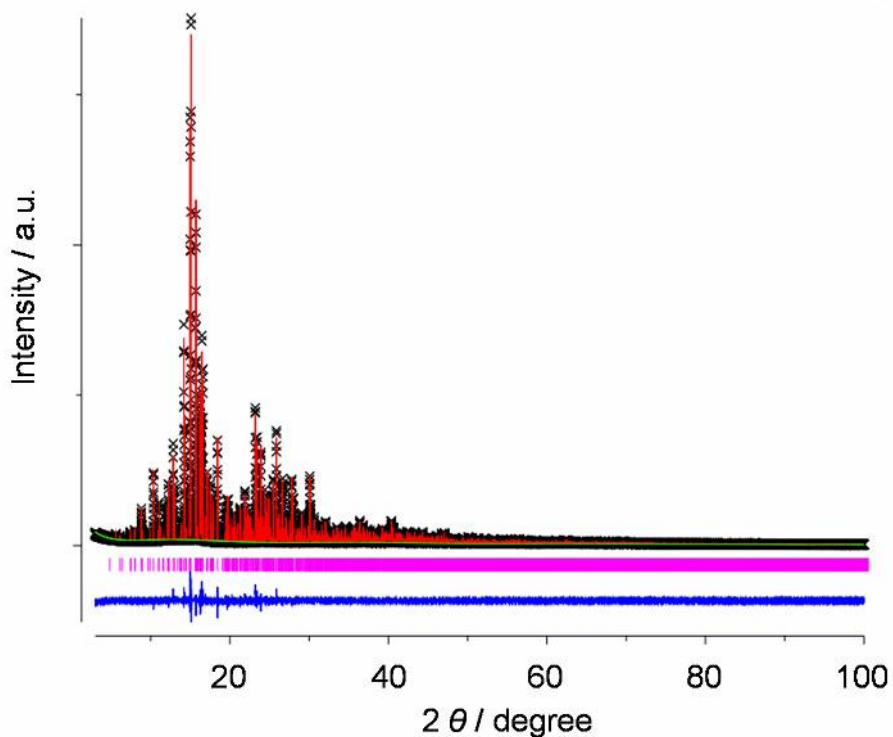


Figure 6-2 Synchrotron x-ray powder diffraction pattern of $\text{TTSP}:\text{Eu}^{2+}$. The crosses, and upper and lower continuous lines are the experimental, calculated and difference profiles, respectively; the vertical lines are the allowed Bragg reflections markers.

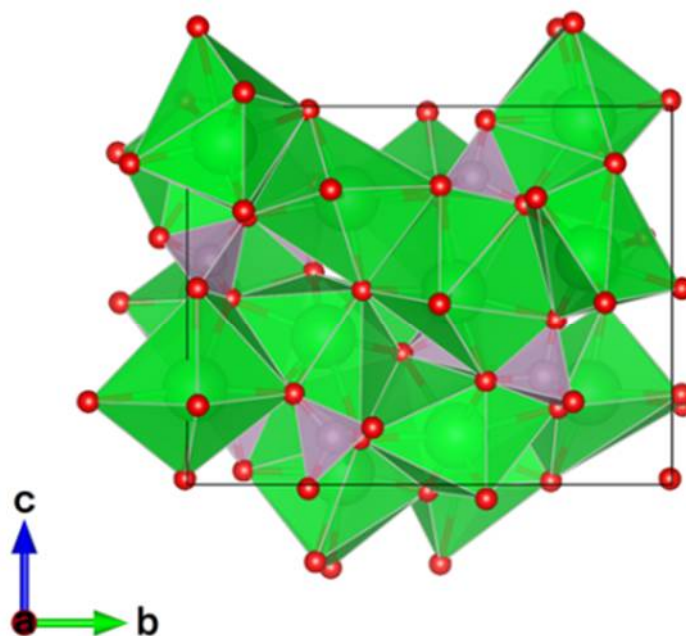


Figure 6-3 Schematic crystal structure illustration of $\text{TTSP}:\text{Eu}^{2+}$ projected onto the (100) plane. Sr, P and O atoms are shown as green, mauve and red spheres.

Table 6-2 Atomic parameters of $\text{Sr}_4(\text{PO}_4)_2\text{O}$ with all sites in the refinement being set to be fully occupied.

Atom	Site	x	y	z
Sr1	2a	0.53266(21)	0.28092(16)	0.39346(16)
Sr2	2a	0.03391(20)	0.32596(16)	0.39863(15)
Sr3	2a	0.25916(21)	0.31862(17)	0.03204(16)
Sr4	2a	0.24033(21)	0.82807(15)	0.24306(16)
Sr5	2a	0.75540(23)	0.01706(15)	0.25294(16)
Sr6	2a	0.24835(23)	0.04954(17)	0.48861(14)
Sr7	2a	0.49668(21)	0.55413(16)	0.12994(15)
Sr8	2a	0.01624(21)	0.57569(15)	0.09355(15)
O1	2a	0.2379(14)	0.1162(4)	0.7254(9)
O2	2a	0.1079(10)	0.2961(6)	0.7808(8)
O3	2a	0.4318(10)	0.2645(7)	0.7965(9)
O4	2a	0.2748(14)	0.2600(7)	0.5625(6)
O5	2a	0.7854(14)	0.2196(6)	0.2405(8)
O6	2a	0.6081(9)	0.3566(7)	0.1223(10)
O7	2a	0.9389(10)	0.3822(6)	0.1508(9)
O8	2a	0.1660(12)	0.7498(7)	0.0104(6)
O9	2a	0.2770(13)	0.1169(7)	0.0373(6)
O10	2a	0.4116(10)	0.0198(6)	0.2383(8)
O11	2a	0.0898(9)	0.0219(6)	0.2091(8)
O12	2a	0.2546(15)	0.1947(5)	0.2589(9)
O13	2a	0.0938(9)	0.5205(7)	0.4797(8)
O14	2a	0.3293(12)	0.4431(5)	0.3456(9)
O15	2a	0.2303(14)	0.6238(6)	0.2881(8)
O16	2a	0.5929(10)	0.0890(7)	0.4937(7)
O17	2a	0.7630(13)	0.3616(8)	0.5170(10)
O18	2a	0.7395(13)	-0.0046(7)	0.0157(9)
P1	2a	0.2622(6)	0.23607(32)	0.7140(4)
P2	2a	0.7903(5)	0.30030(31)	0.1251(4)
P3	2a	0.2577(6)	0.08866(31)	0.1861(4)
P4	2a	0.2664(5)	0.54795(33)	0.4054(4)

Table 6-3 Bond distances, bond valence sums and ECoNs of $\text{Sr}_4(\text{PO}_4)_2\text{O}$.

Bond	Distance (Å)	Bond Valence	Bond	Distance (Å)	Bond Valence
Sr1_O17	2.316	0.59	Sr5_O18	2.350	0.53
Sr1_O5	2.530	0.33	Sr5_O11	2.514	0.34
Sr1_O4	2.555	0.31	Sr5_O10	2.544	0.32
Sr1_O14	2.576	0.29	Sr5_O5	2.562	0.30
Sr1_O16	2.645	0.24	Sr5_O16	2.814	0.15
Sr1_O12	2.664	0.23	Sr5_O13	2.844	0.14
Sr1_O6	2.891	0.12	Sr5_O2	2.980	0.10
Total		2.10	Total		1.89
ECoN		5.6	ECoN		5.0
Bond	Distance (Å)	Bond Valence	Bond	Distance (Å)	Bond Valence
Sr2_O17	2.368	0.51	Sr6_O17	2.368	0.51
Sr2_O4	2.529	0.33	Sr6_O1	2.476	0.38
Sr2_O13	2.612	0.26	Sr6_O13	2.577	0.29
Sr2_O7	2.626	0.25	Sr6_O16	2.595	0.28
Sr2_O14	2.690	0.21	Sr6_O4	2.754	0.18
Sr2_O12	2.706	0.20	Sr6_O10	2.777	0.17
Sr2_O5	2.743	0.19	Sr6_O12	2.905	0.12
Total		1.96	Total		1.92
ECoN		6.1	ECoN		5.7
Bond	Distance (Å)	Bond Valence	Bond	Distance (Å)	Bond Valence
Sr3_O18	2.274	0.66	Sr7_O18	2.365	0.51
Sr3_O9	2.544	0.32	Sr7_O9	2.486	0.37
Sr3_O2	2.715	0.20	Sr7_O1	2.534	0.33
Sr3_O12	2.722	0.20	Sr7_O6	2.621	0.26
Sr3_O3	2.740	0.19	Sr7_O15	2.669	0.23
Sr3_O6	2.760	0.18	Sr7_O3	2.794	0.16
Sr3_O7	2.768	0.17	Sr7_O14	2.834	0.14
Total		1.90	Total		2.00
ECoN		4.4	ECoN		5.7
Bond	Distance (Å)	Bond Valence	Bond	Distance (Å)	Bond Valence
Sr4_O17	2.397	0.47	Sr8_O18	2.340	0.55
Sr4_O8	2.545	0.32	Sr8_O15	2.543	0.32
Sr4_O3	2.585	0.28	Sr8_O9	2.562	0.30
Sr4_O15	2.611	0.26	Sr8_O7	2.566	0.30
Sr4_O2	2.613	0.26	Sr8_O8	2.591	0.28
Sr4_O11	2.701	0.21	Sr8_O1	2.650	0.24
Sr4_O10	2.725	0.19			
Total		2.00	Total		1.98
ECoN		6.4	ECoN		5.5

6.3.2 Optical properties of $\text{Sr}_4(\text{PO}_4)_2\text{O}:\text{Eu}^{2+}$

Figure 6-4 shows the PL and PLE spectra of $\text{TTSP}:\text{Eu}^{2+}$ at different Eu concentrations with respect to Sr, excited at 465 nm and monitored at 680 nm at room temperature. $\text{TTSP}:\text{Eu}^{2+}$ has a broad red emission spectrum with a peak position at 695 nm and a full width at half maximum of 170 nm. The emission at 695 nm corresponds to the $4f^65d^1 - 4f^7$ transition of the Eu^{2+} ions. The Stokes shift is estimated as around 6300 cm^{-1} and the color coordinates on the CIE chromaticity diagram are (0.648, 0.350). The emission intensity of $\text{TTSP}:\text{Eu}^{2+}$ initially increases with higher Eu doping due to significantly enhanced absorbance, reaches a maximum at $x = 0.005$ (0.5 mol%), and then decreases, resulting from the concentration quenching. The asymmetric emission spectra of $\text{TTSP}:\text{Eu}^{2+}$ can be deconvoluted and ascribed to up to eight different emission sites, which could be identified as the different coordination environments of Sr^{2+} ions being occupied by Eu^{2+} ions. However it was found to be difficult to relate the deconvoluted Gaussian components to the different coordination environments of Eu^{2+} ions at Sr sites. As discussed later, Eu^{2+} ions in some Sr sites of TTSP seem not to contribute to the emission spectra of $\text{TTSP}:\text{Eu}^{2+}$, presumably due to non-radiative relaxation processes of Eu^{2+} ions in some of the Sr sites. As mentioned above, it was not possible to determine the distribution of Eu^{2+} ions over the cation sites by powder X-ray diffraction data (PXRD) due to the large number of Sr sites in TTSP, but it is expected that this ion uniformly substitutes at eight Sr sites for doping levels over 0.5 mol%. Normally, different Eu^{2+} ions distribution across several cation sites with different crystal field environments can change the emission spectrum depending on the contribution from each site. However, the spectral shapes from samples with over 0.5 mol% doping level are the same. This implies that Eu^{2+} ions are uniformly distributed across the eight Sr sites with doping levels over 0.5 mol%. However, $\text{TTSP}:\text{Eu}^{2+}$ containing only 0.1 mol% of Eu^{2+} shows a slightly shorter emission peak wavelength (Figure 6-5).

The excitation spectrum monitored at 680 nm comprises three main absorption peaks located around 280, 320, and 450 nm. Having a main absorption around 450 nm, which enables it to match to blue LEDs, is exceptional in phosphate phosphors. When comparing excitation spectra among $\text{TTSP}:\text{Eu}^{2+}$, $\alpha\text{-Sr}_2\text{P}_2\text{O}_7:\text{Eu}^{2+}$ and $\alpha\text{-Sr}_3(\text{PO}_4)_2:\text{Eu}^{2+}$, only $\text{TTSP}:\text{Eu}^{2+}$ can be excited by the blue LED. In the chemical formula, $\text{Sr}_4(\text{PO}_4)_2\text{O}:\text{Eu}^{2+}$ contains isolated O^{2-} ions whereas $\alpha\text{-Sr}_2\text{P}_2\text{O}_7:\text{Eu}^{2+}$ and $\alpha\text{-Sr}_3(\text{PO}_4)_2:\text{Eu}^{2+}$ do not. Isolated O^{2-} ions, as found in $\text{SrO}:\text{Eu}^{2+}$ and $\text{CaO}:\text{Eu}^{2+}$, are more polarizable than O^{2-} ions in PO_4 and it is likely that this structural feature is responsible for the large centroid shift which enables $\text{TTSP}:\text{Eu}^{2+}$ to be excited in the blue,¹⁴ consistent with the optical properties of $\text{TTCP}:\text{Eu}^{2+}$.¹⁵

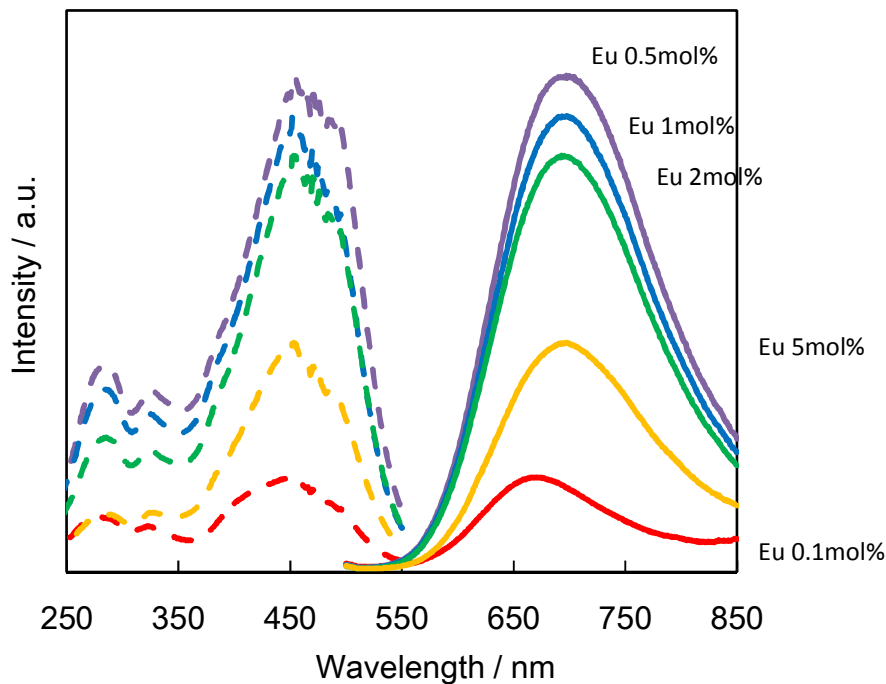


Figure 6-4 PL (solid lines) and PLE (dashed lines) spectra of TTSP activated with different concentrations of Eu^{2+} , excited at 465 nm and monitored for 680 nm emission at room temperature.

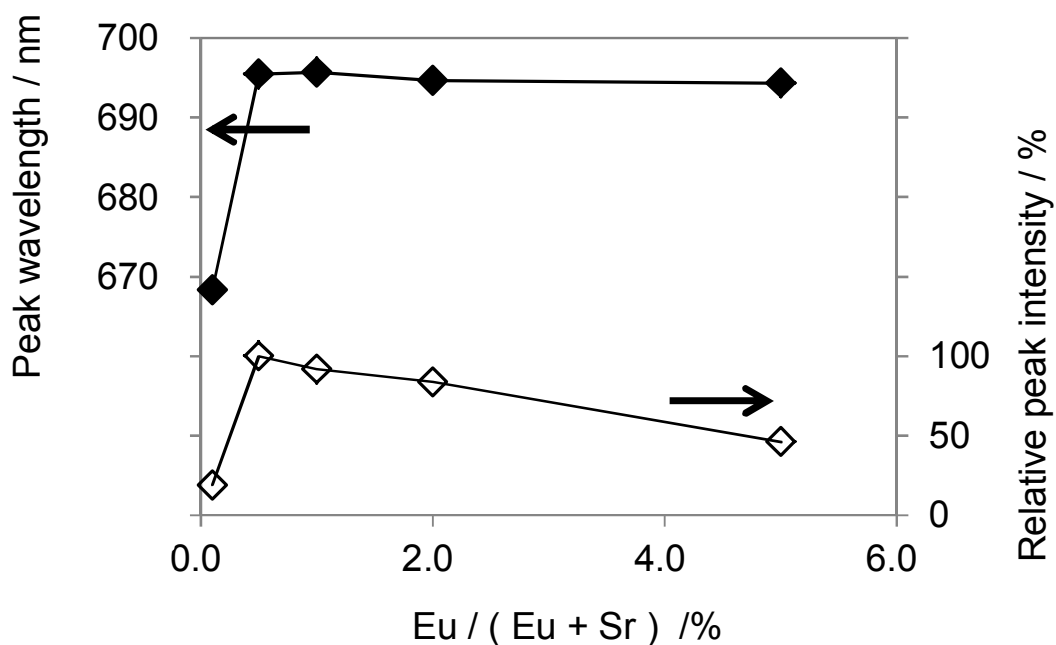


Figure 6-5 Emission peak wavelength and relative peak intensity of TTSP: Eu^{2+} as a function of Eu concentration.

The comparison of PL / PLE at room temperature and higher between TTSP: Eu^{2+} and TTCP: Eu^{2+}

Figure 6-6 shows the PL and PLE spectra for TTSP: Eu^{2+} at 0.5 mol% doping with respect to Sr, compared with TTCP: Eu^{2+} at room temperature. The emission color of TTSP: Eu^{2+} is deep red, which is very similar to the PL of TTCP: Eu^{2+} . The excitation range is also very similar.

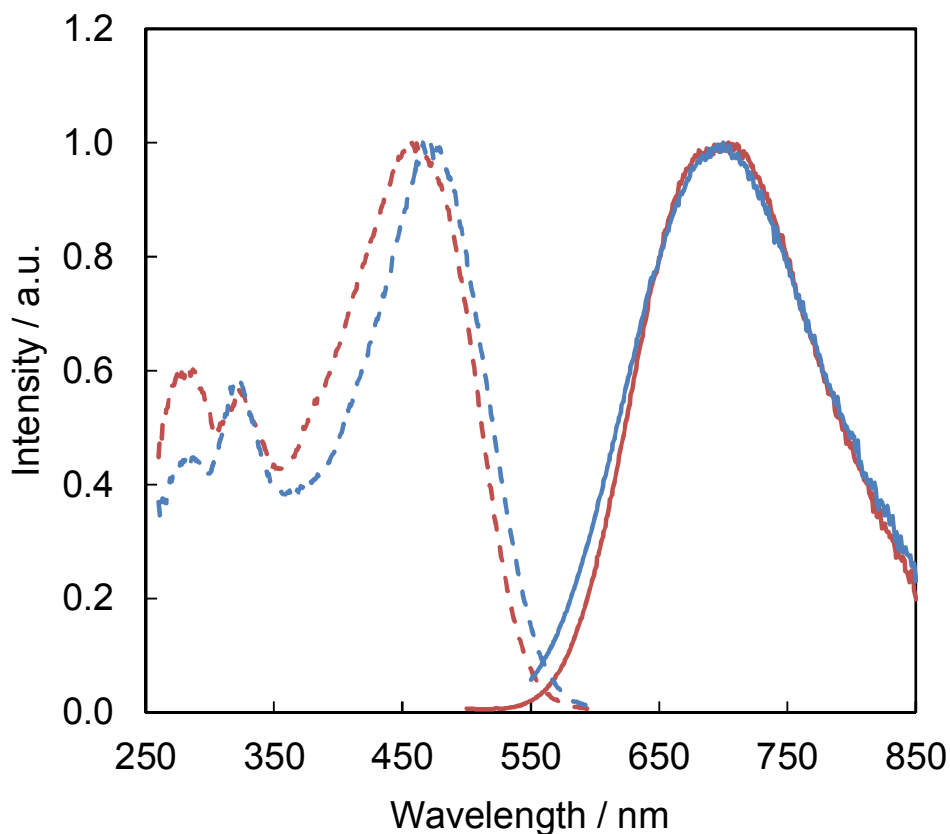


Figure 6-6 PL(solid line) and PLE (dashed line) spectra of TTSP with 0.5 % of Eu^{2+} (red) and TTCP with 0.5 % of Eu^{2+} (blue), excited at 465 nm and monitored for 700 nm emission at room temperature.

As shown in Table 6-1, the lattice volume of TTSP is larger than that of TTCP and a significantly shorter emission peak wavelength from TTSP: Eu^{2+} is expected against TTCP: Eu^{2+} due to the weaker crystal fields on the Eu^{2+} ions in the Sr sites. In simpler structures, SrO has a larger lattice volume, with a Sr-O bond length of 2.58 Å, than CaO with a Ca-O bond length of 2.40 Å; accordingly, an emission peak wavelength of 625 nm was reported for SrO: Eu^{2+} ,¹⁶ whereas it was 733 nm for CaO: Eu^{2+} .¹⁷ This is the typical case for the relationship between the lattice volume and the emission wavelength being affected by the crystal fields on the cation sites. It has therefore been more closely analyzed that the detailed link between the structure and the emission performance by comparison of TTSP: Eu^{2+} and TTCP: Eu^{2+} to enhance our understanding of the unique

properties of these materials, particularly the differences in the coordination environments of the cation sites between TTSP and TTCP. When discussing metal sites heavily distorted from ideal symmetry, the idea of ECoN is useful.¹⁸ ECoN was introduced for TTCP: Eu^{2+} in Chapter 5 to deal with structures containing highly distorted coordination polyhedron. ECoN is defined as the sum of the bond weights, which is calculated from the each bond length and the smallest bond length in the coordination polyhedra.^{18,19} Figure 6-7 compares the coordination environments around cation sites for TTSP and TTCP in terms of average bond length(a), shortest bond length(b) and ECoNs(c), with sites in the two materials paired by the order of their values rather than crystallographic site. Due to the expansion of the lattice volume, the average bond lengths and the shortest bond lengths of TTSP are significantly longer than for TTCP, which is typically expected to lead to weaker crystal field splitting. However the distortion around the Eu^{2+} ions and the polarizability of O^{2-} ions can also be crucial in determining the emission color. The isolated O^{2-} ions played an important role in achieving a large red shift in TTCP: Eu^{2+} , combined with the distortions of the polyhedra enabling the isolated O^{2-} ions to get closer to the Eu^{2+} ions.

ECoN decreases its value as the shortest bond length becomes smaller, and the shortest bond has an influence on the distortion of the coordination polyhedra. The eight Sr sites in TTSP have ECoN values ranging from 4.42 to 6.42, depending on the distortion, while the coordination numbers evaluated from bond valence sum are six or seven. Normally the site with the smaller value of the coordination number is more compressed and this places higher chemical pressure on the dopant. Taking into account the deviation in bond lengths from the average, ECoN can therefore indicate the degree of distortion and stress in the polyhedron. When one cation site has a smaller ECoN in TTSP or TTCP, the Eu^{2+} ion in that site can feel a stronger crystal field than in larger ECoN sites. It can be linked to the site that can show longer wavelength emission. As shown in Figure 6-7(c), the degrees of the distortion around the cation sites described by ECoN, between TTSP and TTCP, are almost equivalent, which helps to explain their similar emission spectra. A link between the more distorted coordination polyhedra and longer emission wavelength in Ce^{3+} ions has already been shown in the garnet structure.²⁰

Another interesting model for large red shifts has been discussed regarding the distortion in $\text{Ca}_{3-x}\text{Sr}_x(\text{PO}_4)_2:\text{Eu}^{2+}$.²¹ $\text{Sr}_2\text{Ca}(\text{PO}_4)_2:\text{Eu}^{2+}$ has a lattice volume of 3843 \AA^3 and exhibits an emission peak wavelength at 527 nm, while $\beta\text{-Ca}_3(\text{PO}_4)_2:\text{Eu}^{2+}$ with a smaller unit cell volume of 3533 \AA^3 showed a shorter emission peak wavelength at 416 nm. In their discussions, larger neighbouring-cations decrease Eu–O bond lengths as a result of higher stress when larger cations replaced smaller ions. That results in strengthening the Eu^{2+} crystal field splitting, generating the red-shifts. This idea can be extended to the comparison between TTSP: Eu^{2+} and TTCP: Eu^{2+} . When comparing neighbouring-cations between Sr and Ca site, larger Sr^{2+} ions as neighbouring-cations can enhance the distortion around an Eu^{2+} ion sitting on a Sr site by displacing the O^{2-} ion from the average position. This is difficult to observe from the average structure obtained from Rietveld refinements, and the low Eu doping concentration also makes it difficult to analyze such local distortions by diffraction-based pair-distribution function techniques.

The polarizability can also have a strong effect on the emission characteristics and the anion polarizability correlates strongly with the cation electronegativity.²² A plot of the anion polarizability against the inverse square of the cation electronegativity shows a good linearity in oxides. When the cation electronegativity decreases, the polarizability of the anion increases. According to this, the isolated O^{2-} ion is more polarizable than O^{2-} in PO_4 . Likewise the O^{2-} ions, which are coordinated by the Sr^{2+} ions, are more polarizable than the O^{2-} ions adjacent to Ca^{2+} ions, since the electronegativity of Sr(0.95) is smaller than Ca(1.0).²³ In some cases, having the larger ions with smaller electronegativity as neighbouring-cations in a distorted polyhedron can be more important than having smaller average bond lengths to generate the red-shifts.

When increasing temperature above room temperature, the luminescence of $\text{TTSP}:\text{Eu}^{2+}$ and $\text{TTCP}:\text{Eu}^{2+}$ showed similar thermal behavior. Figure 6-8 presents the temperature dependence of PL spectra of $\text{TTCP}:\text{Eu}^{2+}$ and $\text{TTSP}:\text{Eu}^{2+}$, excited at 465 nm from 298 K to 423 K. An arrhenius plot of the peak intensity decrease is shown in Figure 6-9 and calculated activation energies from the plot for $\text{TTCP}:\text{Eu}^{2+}$ and $\text{TTSP}:\text{Eu}^{2+}$ are both 0.3 eV, which is categorized by stronger thermal quenching for Eu^{2+} activated phosphors.²⁴ The strong thermal quenching can be related to the large stokes shift, which is explained by the CCD, wherein thermal quenching of PL becomes stronger when the transversal offset between the ground-state parabola and the excited state parabola becomes larger, leading to stronger thermal quenching of longer emission wavelengths.²⁵

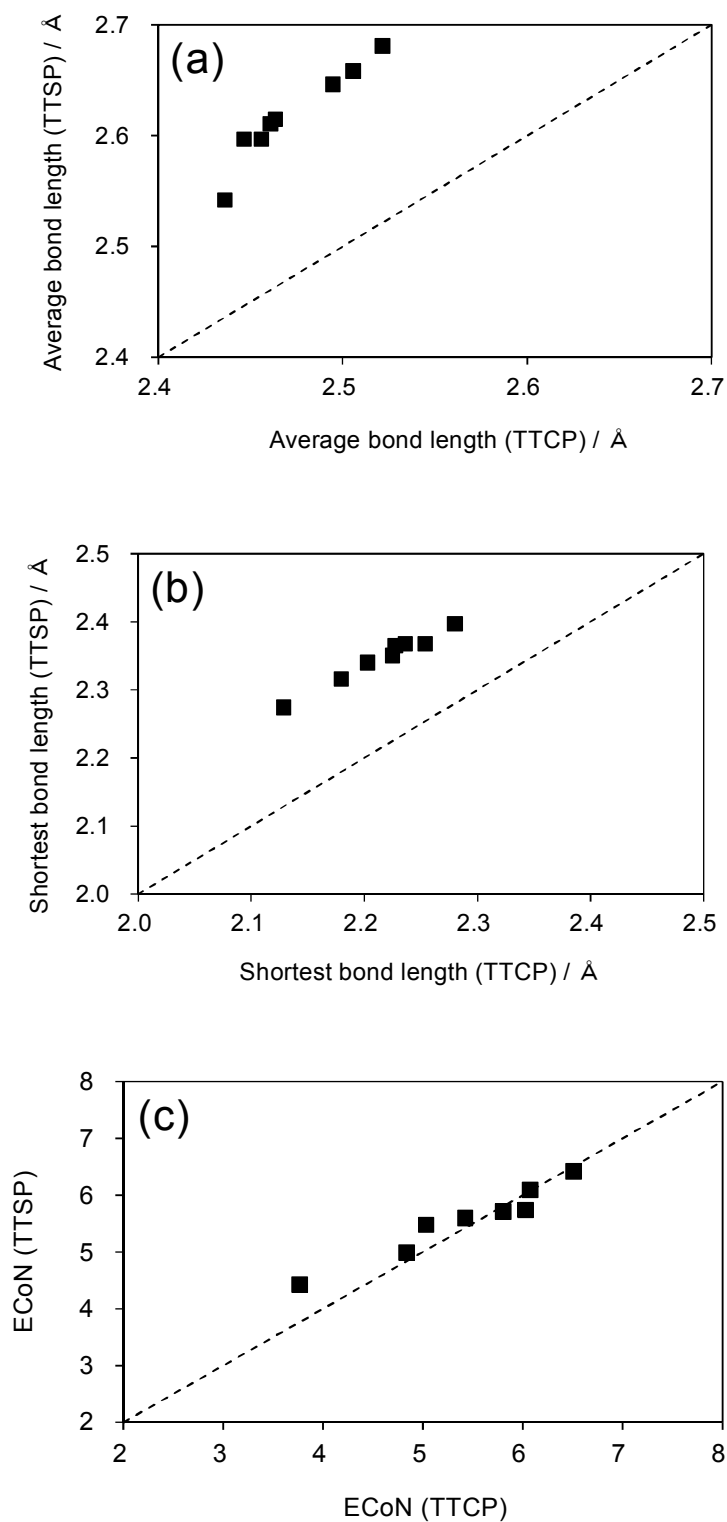


Figure 6-7 Comparison of each environment around divalent cation between TTSP and TTCP, average bond length(a), shortest bond length(b) and ECoN(c).

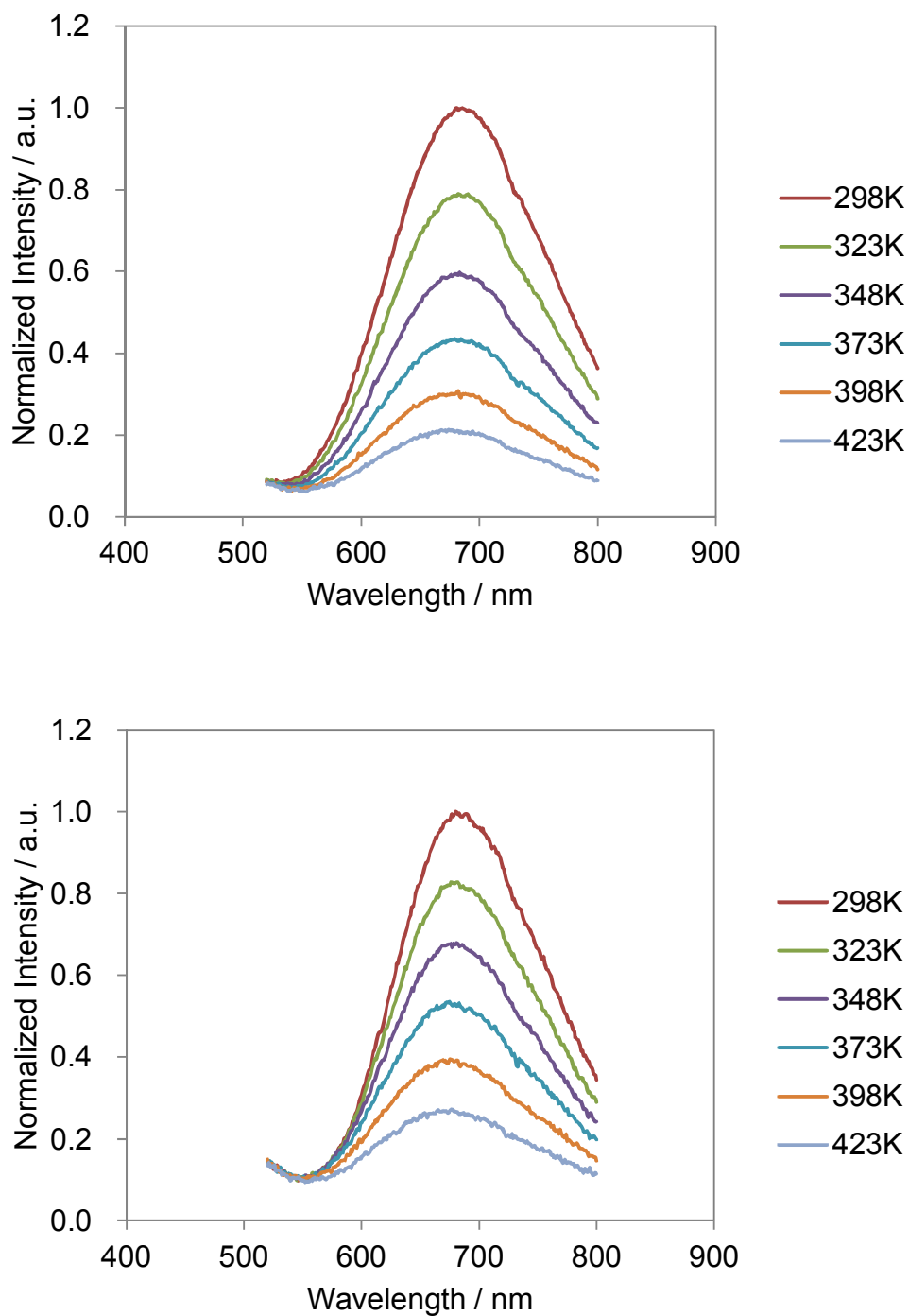


Figure 6-8 Temperature dependence of PL spectra of TTCP:Eu²⁺ (Top) and TTSP:Eu²⁺ (Bottom), excited at 465 nm from 298 K to 423 K.

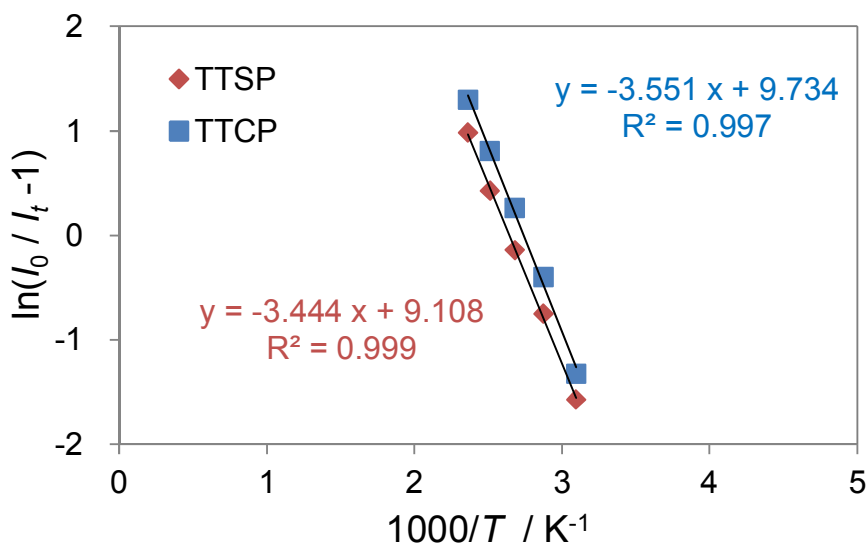


Figure 6-9 Temperature dependence of peak intensity for TTSP (red) and TTCP (blue) on Arrhenius plot.

The comparison of PL / PLE at 77 K between TTSP:Eu²⁺ and TTCP:Eu²⁺

Figure 6-10 shows the comparison of PL and PLE between TTSP:Eu²⁺ and TTCP:Eu²⁺ at 77 K. TTCP:Eu²⁺ has a yellow emission component at around 560 nm, being excited by 465 nm light at 77 K. However, as the temperature increases to ambient conditions the emission shoulder at around 560 nm decreases its peak intensity rapidly, showing much stronger thermal quenching than at around 670 nm. This is the opposite of what would be expected from the conventional idea of the CCD, wherein thermal quenching of PL becomes stronger when the transversal offset between the ground-state parabola and the excited state parabola becomes larger, leading to stronger thermal quenching of longer emission wavelengths.²⁵ In the case of TTSP:Eu²⁺, it interestingly emits only red light at 77 K. A comparison of the thermal behavior of TTSP:Eu²⁺ and TTCP:Eu²⁺, in particular their possible energy diagrams, is important for the key factors responsible for the thermal quenching to be understood.

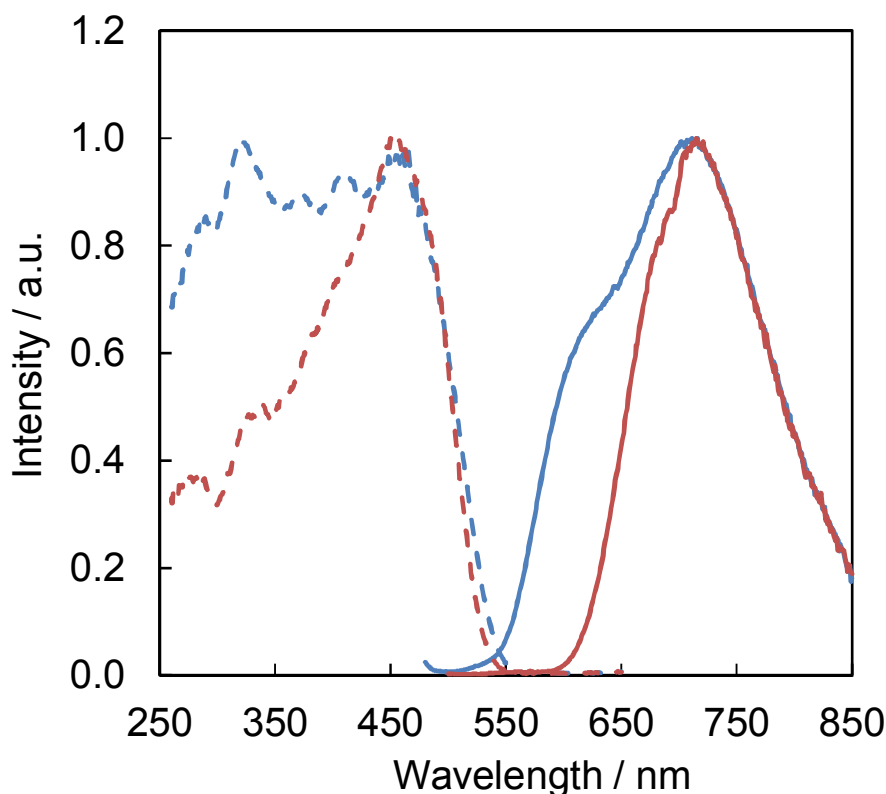


Figure 6-10 PL (solid line) and PLE (dashed line) spectra of TTSP:Eu²⁺ (red) and TTCP:Eu²⁺ (blue), excited at 465 nm and monitored for 700 nm emission at 77 K.

The diffuse reflection spectra of Eu-doped TTSP and TTCP were measured, and their absorption spectra (K/S) derived with the Kubelka - Munk function are shown in Figure 6-11. TTSP:Eu²⁺ showed a quite similar absorption curve to TTCP:Eu²⁺. It increases the absorption in the range of 3 - 5 eV associated with the energy transition from the $4f^7(^8S_{7/2})$ ground state to the $4f^65d^1$ excited state of the Eu²⁺ ions, and the sudden rise around 5.5 eV corresponds to the absorption at the band gap of TTSP. This confirms that the crystal field environment around Eu²⁺ in the TTSP structure is very similar to the one in the TTCP structure. The value of the optical band gap can be calculated by extrapolating the Kubelka - Munk function $F(R_\infty)$ to $K/S = 0$.²⁶ This gave a value of the optical band gap in the Eu-doped TTSP, E_g , of about 5.5 eV for TTSP and 6.2 eV for TTCP, which appears sufficiently close to the computed band gap of 5.47 eV for TTSP and 6.12 eV for TTCP. The calculated Densities of States (DOSs) from TTSP and TTCP are shown in Figure 6-12. The band gap differences between TTSP and TTCP are 0.7 eV from the experiment and 0.65 eV from the calculation, respectively. Thus, around 0.7 eV of energy difference in the band gap is assumed.

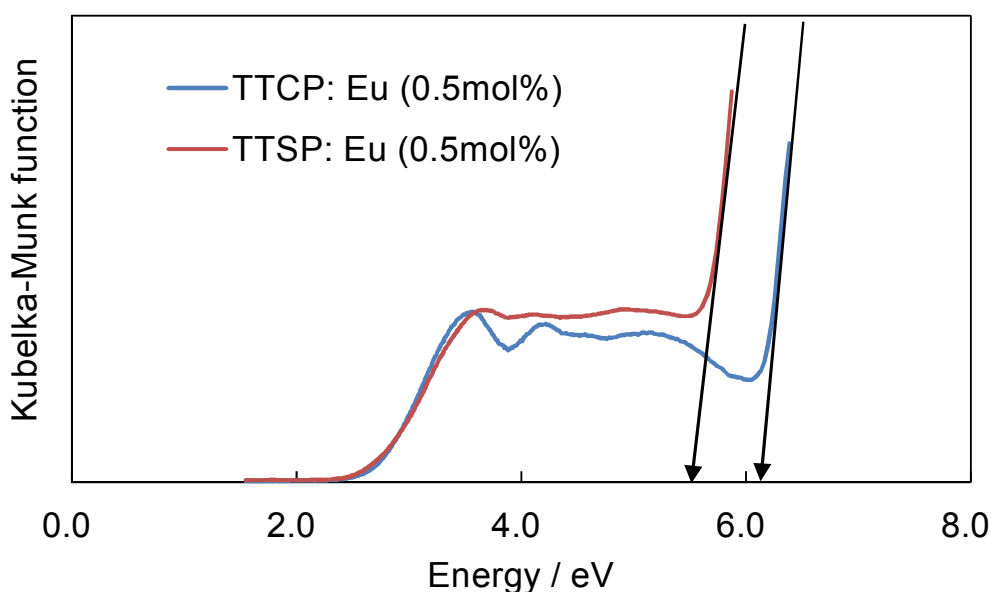


Figure 6-11 Absorption spectra of TTSP: Eu^{2+} (red) and TTCP: Eu^{2+} (blue).

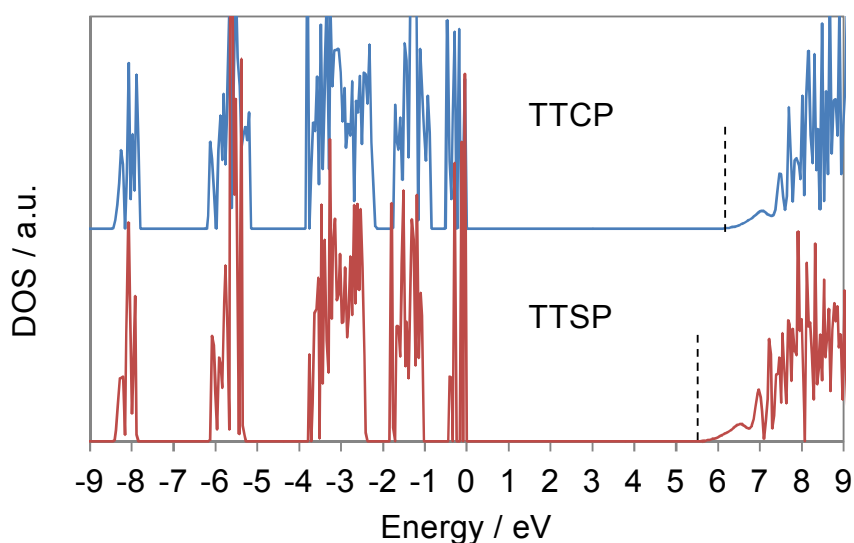


Figure 6-12 Calculated DOSs of TTSP (red) and TTCP (blue). The vertical dashed bars indicate the end of the fundamental band gap.

The stronger thermal quenching of shorter wavelength emission can be explained on the basis of auto-ionization from the $5d$ level of Eu^{2+} to the conduction band, as discussed in the $\text{SrAl}_2\text{O}_4:\text{Eu}^{2+},\text{Dy}^{3+}$ phosphor,²⁷ wherein the blue emission has stronger thermal quenching (little luminescence at room temperature) than green emission. Similarly, the degree of auto-ionization can be considered on each Sr and Ca site. The schematic energy diagram

for $\text{TTCP}:\text{Eu}^{2+}$ was suggested in Chapter 5 to explain the different thermal quenching behavior representing two typical sites with the yellow emission at the peak position of 560 nm being excited by 346 nm and the red emission at the peak position of 670 nm being excited by 466 nm, as shown in Figure 6-13(b). A smaller energy gap between the $5d$ energy level of Eu^{2+} and the bottom of conduction band on the 560 nm emission site should therefore be expected compared to the 670 nm emission site. These energy gaps between the $5d$ energy levels of Eu^{2+} and the bottom of conduction band on each emission site can affect the degree of auto-ionization. Considering the PLE and absorption spectra of $\text{TTSP}:\text{Eu}^{2+}$ and $\text{TTCP}:\text{Eu}^{2+}$, it is assumed that inert $4f$ ground states and excited $5d$ levels of each Eu^{2+} in both TTSP and TTCP structure locate at more or less the same energy level in the band gap. The evaluated band gaps of $\text{TTSP}:\text{Eu}^{2+}$ and $\text{TTCP}:\text{Eu}^{2+}$ from the Kubelka-Munk function are about 5.5 eV and 6.2 eV, respectively.

The thermal excitation of the $5d$ electron to the conduction band states was suggested as an intrinsic mechanism.²⁴ As shown in their empirical formula, $\Delta E = T_{0.5}/680$ eV, where $T_{0.5}$ is the quenching temperature at which the emission intensity has dropped to 50 % of the low temperature value and ΔE is the energy barrier, a sub-eV difference may be significant for thermal quenching. The energy difference of the band gap between TTSP and TTCP is about 0.7 eV, which corresponds to the quenching temperature difference of 476 K. This can be a crucial factor to make the energy relaxation process non-radiative on the shorter emission of $\text{TTSP}:\text{Eu}^{2+}$. This explains why, unlike in $\text{TTCP}:\text{Eu}^{2+}$, several of the sites do not appear to contribute to the emission spectra.

The radiative and non-radiative behavior was reported on the Ce-activated garnet phosphors by photo conductivity measurement.²⁸ Although the systems were different, $\text{Y}_3\text{Al}_5\text{O}_{12}:\text{Ce}^{3+}$ with the band gap of 6.5 eV was radiative and $\text{Y}_3\text{Ga}_5\text{O}_{12}:\text{Ce}^{3+}$ with the band gap of 5.5 eV was non-radiative. About 1 eV energy difference in band gap was significant enough to differentiate radiative and non-radiative behaviors. The thermal quenching of $\text{TTSP}:\text{Eu}^{2+}$ and $\text{TTCP}:\text{Eu}^{2+}$ can basically be explained by CCD, however when phosphors have different crystallographic sites for luminescence activators or phosphors in analogous structures with different crystal fields are compared, the gap between the $5d$ level of activator and the bottom of conduction band should be noted since $5d$ level is strongly affected by the crystal field in the host lattice.

The temperature dependence of PL below room temperature was measured from 50 K to 300 K, in which the emission from shorter emission sites was avoided as much as possible by shifting the excitation wavelength longer with the excitation of 470 nm blue LED (Figure 6-14 for $\text{TTCP}:\text{Eu}^{2+}$ and Figure 6-15 for $\text{TTSP}:\text{Eu}^{2+}$). They both showed clear blue shift in emission peak wavelength, which is explained by a thermally active phonon-assisted tunneling from the excited states of the lower $5d$ energy level to the excited states of the higher $5d$ energy level.²⁹

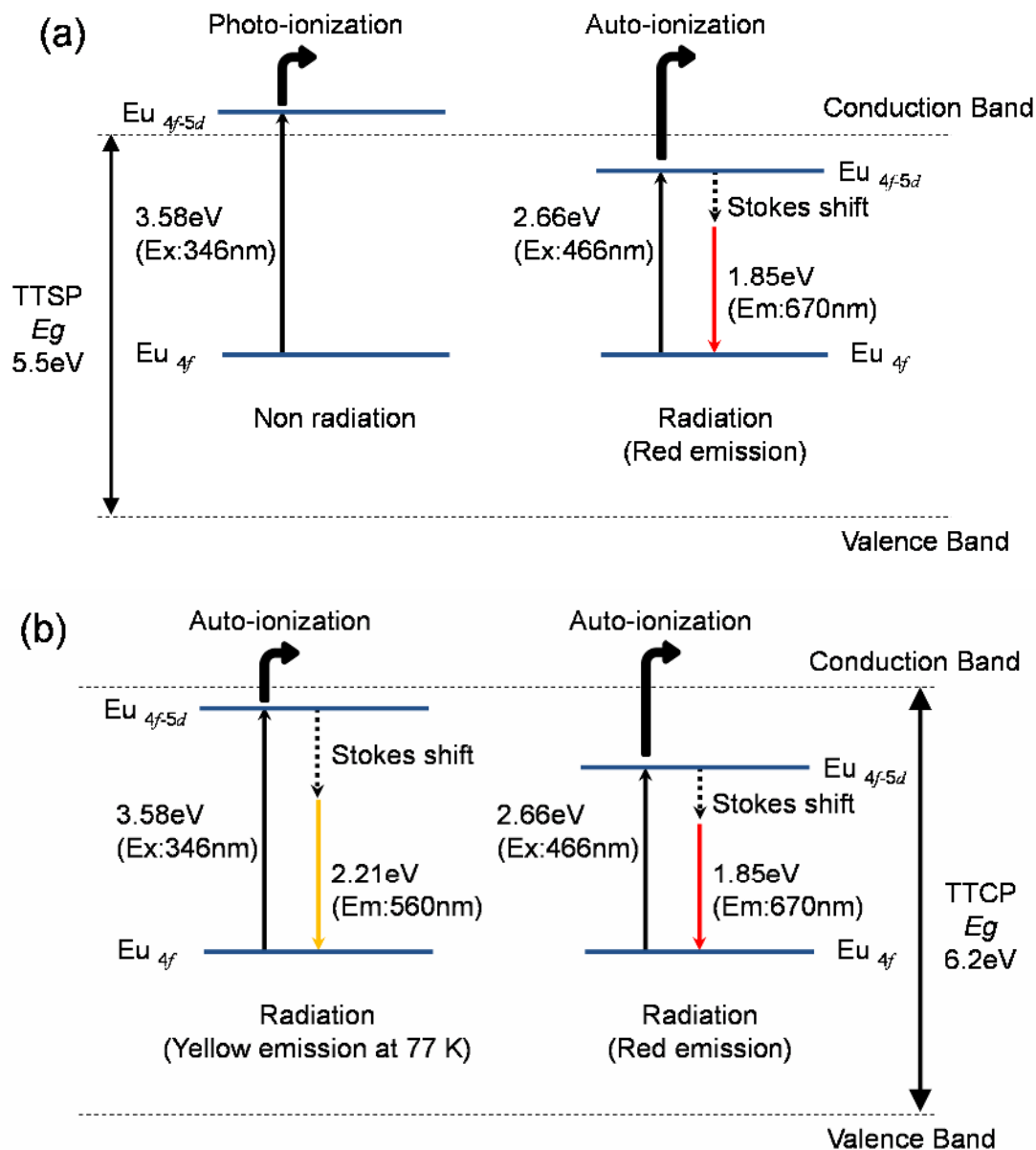


Figure 6-13 Schematic energy diagram of TTSP:Eu²⁺(a) and TTCP:Eu²⁺(b) representing yellow emission (560 nm) and red emission (670 nm).

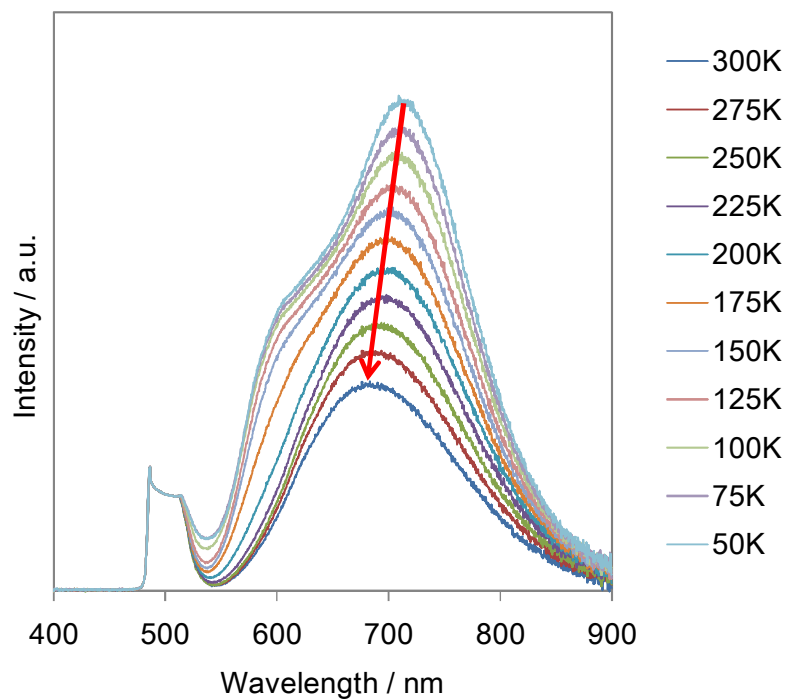


Figure 6-14 PL of TTCP activated with 1 mol% of Eu^{2+} , excited by 470 nm blue LED light at lower temperature from 50 K to 300 K.

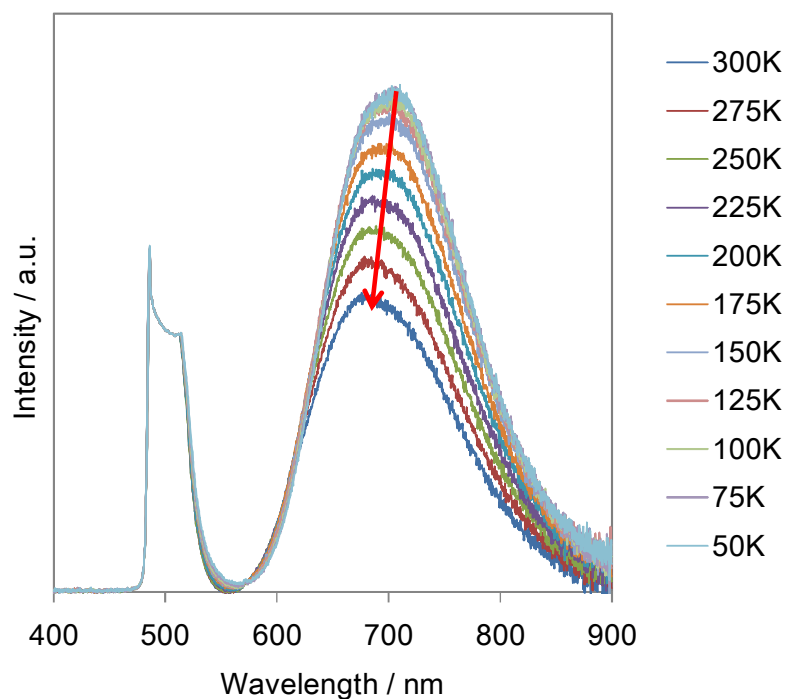


Figure 6-15 PL of TTSP activated with 1 mol% of Eu^{2+} , excited by 470 nm blue LED light at lower temperature from 50 K to 300 K.

6.4 Summary

The new red phosphor $\text{Sr}_4(\text{PO}_4)_2\text{O}:\text{Eu}^{2+}$ is studied. It shows a broad deep red emission with a peak position at 680 nm being excited at around 450 nm, which matches well with blue LEDs. The crystal structure of $\text{Sr}_4(\text{PO}_4)_2\text{O}:\text{Eu}^{2+}$ was refined in a monoclinic $P2_1$ structure. It is isotypic to $\text{Ca}_4(\text{PO}_4)_2\text{O}:\text{Eu}^{2+}$, which also shows deep red emission. Their emission and excitation spectra at room temperature are very similar despite $\text{Sr}_4(\text{PO}_4)_2\text{O}:\text{Eu}^{2+}$ having a much larger unit cell volume than $\text{Ca}_4(\text{PO}_4)_2\text{O}:\text{Eu}^{2+}$. The relationship between the crystal structure and the emission spectra of $\text{Sr}_4(\text{PO}_4)_2\text{O}:\text{Eu}^{2+}$ was discussed by comparison with $\text{Ca}_4(\text{PO}_4)_2\text{O}:\text{Eu}^{2+}$ to find the key factors for achieving a large redshift of the $5d$ level of Eu^{2+} ion to emit red light. The importance of the higher anion polarizability and the heavy distortion of the coordination polyhedron were confirmed based on the idea of the electronegativity of the cations and the ECoNs. $\text{Ca}_4(\text{PO}_4)_2\text{O}:\text{Eu}^{2+}$ shows yellow emission at 77 K, whereas $\text{Sr}_4(\text{PO}_4)_2\text{O}:\text{Eu}^{2+}$ does not. The different thermal quenching behaviors for Eu^{2+} dopants in $\text{Sr}_4(\text{PO}_4)_2\text{O}:\text{Eu}^{2+}$ and $\text{Ca}_4(\text{PO}_4)_2\text{O}:\text{Eu}^{2+}$ were also discussed and attributed to the degree of auto/photo-ionization caused by the different band gaps of the materials. The importance of the large band gap of the host lattice in avoiding non-radiative processes of energy relaxation was also confirmed.

6.5 References

- 1 C. C. Lagos, *J. Electrochem. Soc.: SOLID STATE SCIENCE*, 1970, **117**, 1189.
- 2 J. C. Zhang, Y. Z. Long, H. D. Zhang, B. Sun, W. P. Han and X. Y. Sun, *J. Mater. Chem. C*, 2014, **2**, 312.
- 3 E. R. Kreidler and F. A. Hummel, *Inorg. Chem.*, 1967, **6**, 884.
- 4 S. P. Thompson, J. E. Parker, J. Potter, T. P. Hill, A. Birt, T. M. Cobb, F. Yuan, and C. C. Tang, *Rev. Sci. Instrum.*, 2009, **80**, 075107.
- 5 A.C. Larson and R. B. Von Dreele, "General Structure Analysis System (GSAS)", Los Alamos National Laboratory Report LAUR 86-748, 1994.
- 6 B. H. Toby, *J. Appl. Crystallogr.*, 2001, **34**, 210.
- 7 K. Momma and F. Izumi, *J. Appl. Crystallogr.*, 2011, **44**, 1272.
- 8 G. Kresse and J. Furthmuller, *Phys. Rev. B*, 1996, **54**, 11169.
- 9 G. Kresse and D. Joubert, *Phys. Rev. B*, 1999, **59**, 1758.
- 10 A. V. Krukau, O. A. Vydrov, A. F. Izmaylov and G. E. Scuseria, *J. Chem. Phys.*, 2006, **125**, 224106.
- 11 H. Bauer and W. Balz, *Z. Anorg. Allg. Chem.*, 1965, **340**, 225.
- 12 Q. Guo, L. Liao, L. Mei and H. Liu, *J. Solid State Chem.*, 2015, **226**, 107.
- 13 R. E. Brese and M. O'Keeffe, *Acta Crystallogr. Sect. B*, 1991, **B47**, 192.
- 14 M. Mikami, *ECS J. Solid State Sci. Technol.* 2013, **2**, R3048.
- 15 N. Komuro, M. Mikami, P. J. Saines and A. K. Cheetham, *J. Lumin.*, 2015, **162**, 25.
- 16 N. Yamashita, *J. Lumin.* 1994, **59**, 195.
- 17 N. Yamashita, *J. Electrochem. Soc.*, 1993, **140**, 840.
- 18 M. Nespolo, G. Ferraris, G. Ivaldi and R. Hoppe, *Acta Crystallogr., Sect. B: Struct. Sci.*, 2001, **57**, 652.
- 19 R. Hoppe, S. Voigt, H. Glaum, J. Kissel, H. P. Muller and K. Bernet, *J. Less-Common. Met.*, 1989, **156**, 105.
- 20 G. Gundiah, J. L. Wu and A. K. Cheetham, *Chem. Phys. Lett.*, 2007, **441**, 250.
- 21 H. Ji, Z. Huang, Z. Xia, M. S. Molokeev, V. V. Atuchin, M. Fang and Y. Liu, *J. Phys. Chem. C*, 2015, **119**, 2038.
- 22 P. Dorenbos, *Phys. Rev. B*, 2002, **65**, 235110.
- 23 A. L. Allred, *J. Inorg. Nucl. Chem.*, 1961, **17**, 215.
- 24 P. Dorenbos, *Condens. Matter*, 2005, **17**, 8103.
- 25 G. Blasse and B. C. Grabmaier, *Luminescent Materials*, Springer, Berlin, 1994.
- 26 C. J. Duan, A. C. A. Delsing and H. T. Hintzen, *Chem. Mater.*, 2009, **21**, 1010.
- 27 J. Ueda, T. Nakanishi, Y. Katayama and S. Tanabe, *Phys. Status Solidi C*, 2012, **9**, 2322.
- 28 J. Ueda, S. Tanabe and T. Nakanishi, *J. Appl. Phys.*, 2011, **110**, 053102.
- 29 C. C. Lin, Y. S. Zheng, H. Y. Chen, C. H. Ruan, G. W. Xiao and R. S. Liu, *J. Electrochem. Soc.*, 2010, **157**, H900.

Chapter 7 Yellow luminescence of $\text{Ca}_6\text{Ba}(\text{PO}_4)_4\text{O}:\text{Eu}^{2+}$

A new phase, $\text{Ca}_6\text{Ba}(\text{PO}_4)_4\text{O}$, was found in the CaO-BaO- P_2O_5 phase diagram and its Eu^{2+} -doped derivative was evaluated as a possible phosphor for SSL. $\text{Ca}_6\text{Ba}(\text{PO}_4)_4\text{O}$ was prepared by conventional solid-state synthesis and its structure was solved *ab initio* from high-resolution, synchrotron X-ray powder diffraction data. The bandgap of $\text{Ca}_6\text{Ba}(\text{PO}_4)_4\text{O}$ was estimated to be 5.8 eV. Under excitation with UV to blue light, $\text{Ca}_6\text{Ba}(\text{PO}_4)_4\text{O}:\text{Eu}^{2+}$ shows strong yellow emission with the peak position at 553 nm. A white LED, which was fabricated with an InGaN blue chip and $\text{Ca}_6\text{Ba}(\text{PO}_4)_4\text{O}:\text{Eu}^{2+}$, achieved a luminous efficacy of 31 lmW^{-1} with a color rendering index of 78 around the correlated color temperature of 6500 K.

7.1 Introduction

Currently, the most common approach for white LEDs is to combine a blue LED with a color-converting phosphor, first achieved using a $\text{YAG}:\text{Ce}^{3+}$ phosphor for blue-to-yellow down conversion.^{1,2} Although $\text{YAG}:\text{Ce}^{3+}$ still plays an important role for white LEDs, its modest color rendering index (CRI, Ra) of 75 restricts its application when good color quality is required.³ $(\text{Ba},\text{Sr})_2\text{SiO}_4$,⁴ also commonly used as a commercial phosphor, has a strong yellow emission but lacks chemical stability against moisture. Most oxide phosphors for LED use have been adapted from those used in CRTs or lamps, and there are few examples of new oxide-based phosphors that exhibit good excitation and emission performance when combined with blue LEDs. Much recent effort has been devoted to developing alternative yellow phosphors to $\text{YAG}:\text{Ce}^{3+}$ based on the more chemically stable (oxy)nitride phosphors such as $\text{Ca}-\alpha\text{-SiAlON}:\text{Eu}^{2+}$ and $\text{CaAlSiN}_3:\text{Ce}^{3+}$.^{5,6} Neither, however, showed any significant improvement in Ra value. Furthermore, (oxy)nitride phosphors involve the handling of sensitive raw materials and require high synthesis temperatures, for which reasons oxide phosphors are generally preferred commercially. There is therefore a drive to find new oxide phosphors suitable for SSL.

The $\text{CaO}-\text{BaO}-\text{P}_2\text{O}_5$ phase diagram is well understood and includes many complex phases such as $(\text{Ca},\text{Ba})_2\text{P}_2\text{O}_7$, $\text{Ca}_2\text{Ba}(\text{PO}_4)_2$, $(\text{Ca},\text{Ba})_3(\text{PO}_4)_2$, $\text{Ca}_{10}(\text{PO}_4)_6\text{O}$ and $\text{Ca}_4(\text{PO}_4)_2\text{O}$ (Figure 7-1).^{7,8,9} However the system has been little explored for phosphor applications in combination with blue LEDs. Lagos reported behavior of $(\text{Ca},\text{Ba})_2\text{P}_2\text{O}_7:\text{Eu}^{2+}$ as a blue phosphor and $(\text{Ca},\text{Ba})_3(\text{PO}_4)_2:\text{Eu}^{2+}$ as a yellow phosphor for UV excitation, but these are not alternatives to $\text{YAG}:\text{Ce}^{3+}$ since they are poorly matched to blue LEDs.¹⁰ The discovery and crystal structure of $\text{Ca}_6\text{Ba}(\text{PO}_4)_4\text{O}$ (hereafter referred to as CBP) is reported in this chapter, a hitherto unknown phase in the $\text{CaO}-\text{BaO}-\text{P}_2\text{O}_5$ system.¹¹ The potential of its Eu^{2+} -activated derivative for use as a phosphor in SSL are also explored. Under excitation from the near UV to the blue, the new phosphor shows bright yellow emission with a high internal quantum yield throughout this excitation range. In addition, the luminous efficacy of a white LED fabricated by the combination of this phosphor and a blue LED was 31 lmW^{-1} and the Ra of 78 is higher than that of $\text{YAG}:\text{Ce}^{3+}$.³ This can be the first report of a yellow emission phosphate phosphor excited by the blue LED.

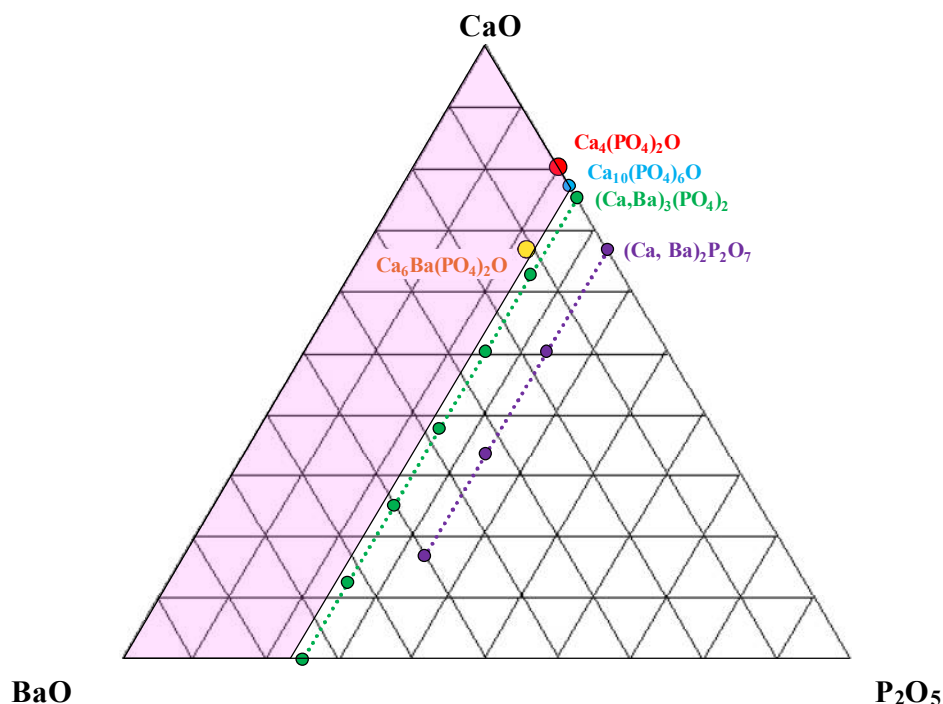


Figure 7-1 Phase diagram in CaO - BaO - P_2O_5 system with CBP phase.

7.2 Experimental

7.2.1 Synthetic procedures

A phase pure sample of CBP was synthesized by conventional solid-state reaction of CaCO_3 (Hakushin Chemicals), BaCO_3 (Hakushin Chemicals) and CaHPO_4 (Alfa Aesar). The ground mixtures of the raw materials were placed in alumina crucibles and heated in a reducing atmosphere of 5 % H_2 + 95 % N_2 at 1250 °C for 10 hrs. CBP can be readily doped with Eu^{2+} by adding Eu_2O_3 (Alfa Aesar) to the starting materials with the same synthesis condition as those for CBP.

7.2.2 Crystallography

Selected area electron diffraction patterns for CBP were collected under precession conditions using a Philips CM30 transmission electron microscope fitted with a Spinning Star precession unit, while SEM images and EDX spectra were obtained using a JEOL 5800LV scanning electron microscope. Synchrotron X-ray diffraction data were collected on beamline I11 at the Diamond Light Source facility in the UK using a wavelength of 0.82713 Å.¹² The model for the crystal structure of CBP was obtained by FOX,¹³ refined by GSAS,^{14,15} and depicted in VESTA.¹⁶

7.2.3 Optical characterization

Photoluminescence and photoluminescence excitation spectra at room temperature were measured using a Horiba FluoroLog-3 spectrometer. The UV-vis reflectance spectra were measured using a PerkinElmer Lambda 750 spectrophotometer. The photoluminescence quantum efficiency was measured from PL measurements with an integrating sphere equipped with a 150 W Xe lamp and a multichannel spectrophotometer (model MCPD7000; Otsuka Electronics). The temperature dependence of the photoluminescence was also measured by a multichannel spectrophotometer (model MCPD7000; Otsuka Electronics).

7.2.4 White LED fabrication

White LEDs were fabricated by embedding the $\text{Ca}_6\text{Ba}(\text{PO}_4)_4\text{O}:\text{Eu}^{2+}$ yellow phosphor in a transparent silicone resin; the down-converter was packaged with 1 W InGaN LED chips, targeting a correlated color temperature of around 6500 K.

7.3 Results and discussion

7.3.1 The structure of $\text{Ca}_6\text{Ba}(\text{PO}_4)_4\text{O}$

A systematic exploration of the $\text{CaO-BaO-P}_2\text{O}_5$ phase diagram revealed the presence of Bragg peaks in some of the X-ray powder diffraction (XRD) patterns which could not be accounted for on the basis of any of the known phases in the system. It has been able to be established that these peaks arise from a hitherto unidentified phase, CBP. The simplest XRD patterns were obtained at a $\text{Ca}/(\text{Ca}+\text{Ba})$ ratio of about 0.85 and imply distinct Ca and Ba sites rather than a solid solution. Ba is a required component for this structure: samples lacking this element never yielded the new phase (Figure 7-2). SEM-EDX analysis also indicates a homogenous $\text{Ca}/(\text{Ca}+\text{Ba})$ ratio of about 0.84. Typical SEM images are shown in Figure 7-3. The molar ratio of $\text{Ca}:\text{Ba}=6:1$ was assumed from these results.

Selected area electron diffraction (SAED) patterns for CBP were obtained by transmission electron microscopy from which it was possible to assign an approximate unit cell with $a = 11.98 \text{ \AA}$, $b = 6.93 \text{ \AA}$, $c = 11.42 \text{ \AA}$ and $\beta = 134.2^\circ$ (Figure 7-4); it was subsequently possible to confirm this result using XRD data. The unknown structure of CBP was solved *ab initio* and refined from high resolution synchrotron X-ray powder diffraction data, as described in the experimental section. The sample contained 0.5 mol% Eu^{2+} , but it was not possible to determine the distribution of europium over the cation sites due to the low concentration. Figure 7-5 shows the observed, calculated, and difference synchrotron profiles for the Rietveld refinement of CBP, in which the XRD pattern was well fitted by the derived structure up to high angles in 2θ . Table 7-1 shows the atomic coordinates and other structural parameters for CBP, including R indexes of $R_{wp} = 6.28 \%$, $R_p = 4.77 \%$, and $R_F = 5.04 \%$ after

refinement of the unit cell and atomic positions. CBP has a monoclinic structure in space group $C2/m$ (Figure 7-6) with refined lattice parameters $a = 12.30304(3) \text{ \AA}$, $b = 7.10454(2) \text{ \AA}$, $c = 11.71603(4) \text{ \AA}$ and $\beta = 134.4420(1)^\circ$, a single Ba site and two Ca sites. The Ba site is coordinated by twelve oxygen atoms with an average bond length of 3.04 \AA , the Ca1 site by eight oxygen atoms with an average bond length of 2.51 \AA , and the Ca2 site by seven oxygen atoms with an average bond length of 2.42 \AA (Figure 7-7). The two P sites are in PO_4 tetrahedra which are isolated from other PO_4 tetrahedra. The structure also contains an oxide ion that is not part of a PO_4 tetrahedron. Bond distances from the divalent cations in the CBP structure are listed in Table 7-2.

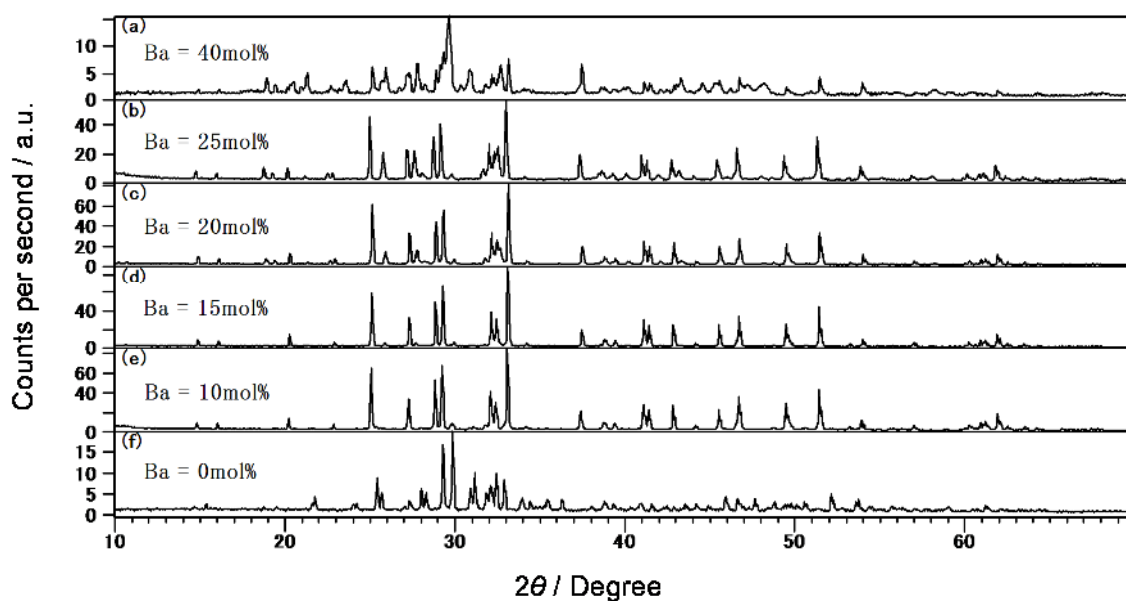


Figure 7-2 Experimental XRD patterns of samples with different concentrations of Ba: (a) apatite; (b)-(c) mixtures of apatite and CBP; (d)-(e) CBP, (f) tetra calcium phosphate.

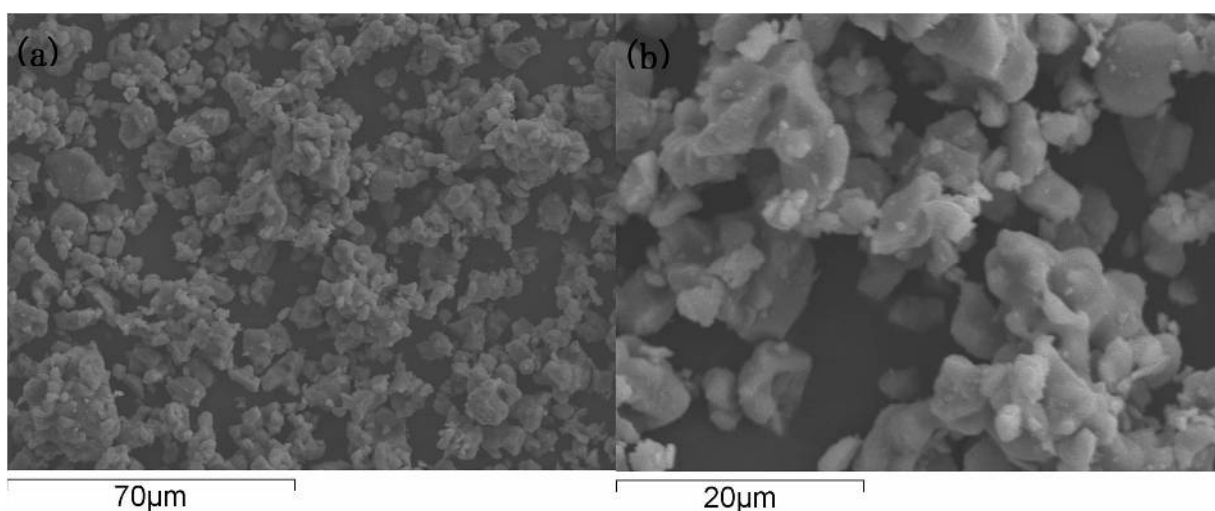


Figure 7-3 SEM images of CBP in the secondary electron mode.

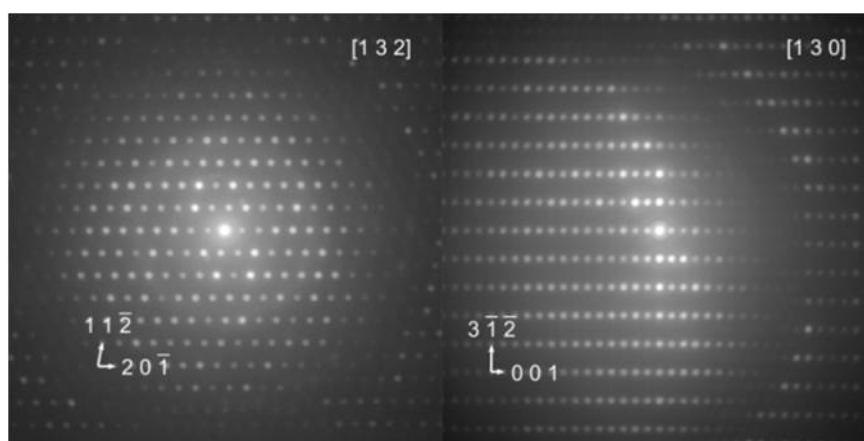


Figure 7-4 SAED patterns under precession conditions at 300 kV from different fragments of the CBP material.

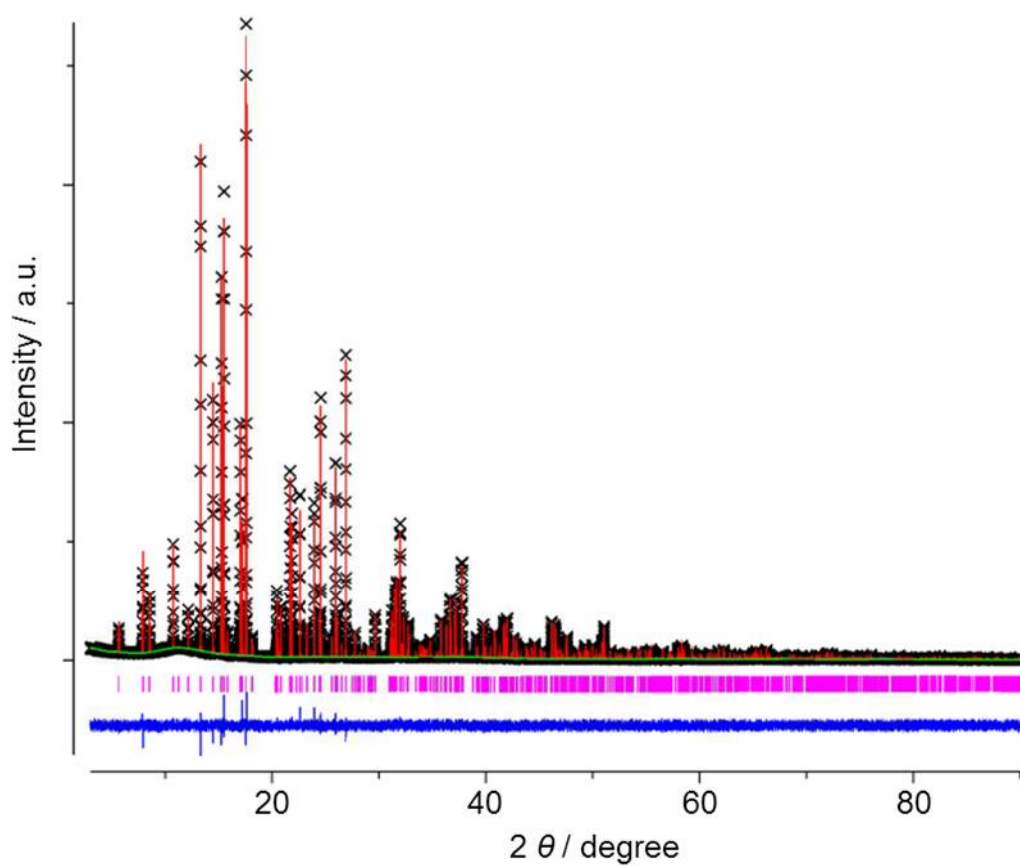


Figure 7-5 Observed, calculated, and difference synchrotron XRD profiles for the Rietveld refinement of CBP.

Table 7-1 Crystallographic data and structure refinement for CBP.

Unit cell dimensions	$a = 12.30304(3) [\text{\AA}]$					
	$b = 7.10454(2) [\text{\AA}]$					
	$c = 11.71603(4) [\text{\AA}]$					
	$\beta = 134.4420(1) [^\circ]$					
Cell volume	$V = 731.142(4) [\text{\AA}^3]$					
<i>R</i> indexes	$R_{wp} = 6.28\% \quad R_p = 4.77\% \quad R_F = 5.04\%$					
Atom	site	<i>x</i>	<i>y</i>	<i>z</i>	occupancy	
Ba	2 <i>a</i>	0	0	0	1	
Ca1	4 <i>i</i>	0.7194(3)	0	0.3117(4)	1	
Ca2	8 <i>j</i>	0.0506(2)	0.7666(3)	0.6930(2)	1	
O	2 <i>c</i>	0	0	0	1	
P1	4 <i>i</i>	0.2664(4)	0	0.3996(1)	1	
O11	4 <i>i</i>	0.4013(7)	0	0.5830(3)	1	
O12	8 <i>j</i>	0.2831(6)	-0.1749(7)	0.3364(4)	1	
O13	4 <i>i</i>	0.1208(7)	0	0.3680(7)	1	
P2	4 <i>i</i>	0.3664(4)	0	0.0472(1)	1	
O21	4 <i>i</i>	0.2877(11)	0	0.1077(12)	1	
O22	4 <i>i</i>	0.2432(10)	0	-0.1397(3)	1	
O23	8 <i>j</i>	0.4620(6)	-0.1797(8)	0.1148(6)	1	

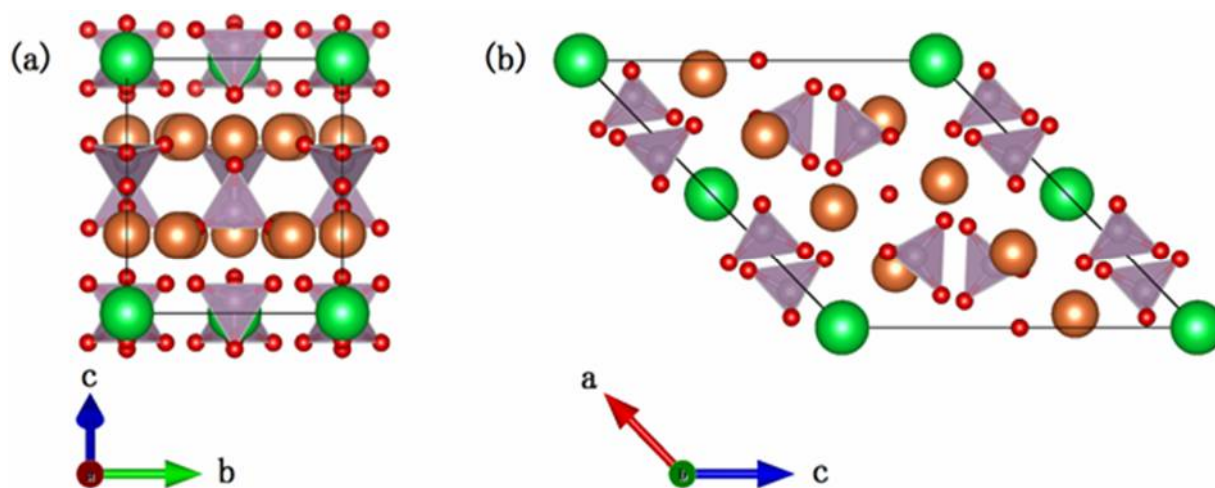


Figure 7-6 Schematic crystal structure illustrations of CBP projected onto (a) the (100) plane and (b) the (010) plane. Ba is green, Ca is brown, P is mauve and oxygen is red.

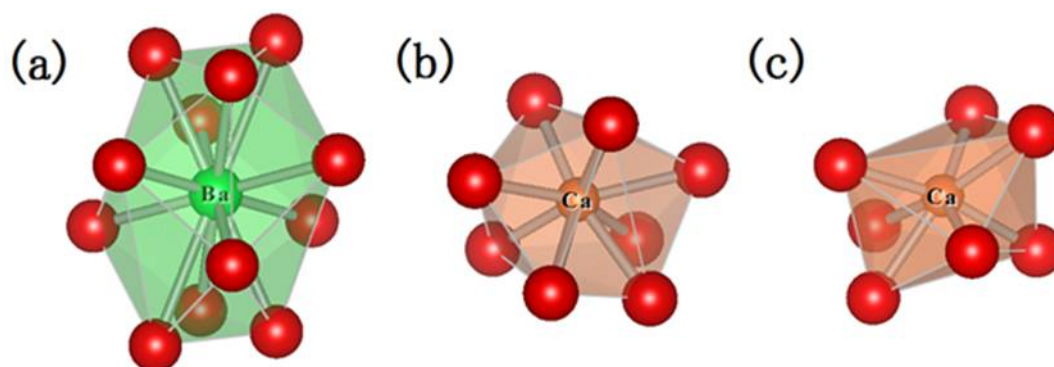


Figure 7-7 Comparison of the coordination geometries around (a) the Ba site, (b) the Ca1 site and (c) the Ca2 site. Colors as in Figure 7-6.

Table 7-2 Bond distances for divalent cations in CBP.

Bond	Distance	Bond	Distance
Ba-O ₂₁	2.804(9)	Ca ₁ -O ₂₂	2.360(11)
Ba-O ₂₁	2.804(9)	Ca ₁ -O ₁₂	2.390(7)
Ba-O ₂₃	2.844(5)	Ca ₁ -O ₁₂	2.390(7)
Ba-O ₂₃	2.844(5)	Ca ₁ -O	2.473(3)
Ba-O ₂₃	2.844(5)	Ca ₁ -O ₁₁	2.509(8)
Ba-O ₂₃	2.844(5)	Ca ₁ -O ₂₃	2.598(6)
Ba-O ₁₂	3.160(3)	Ca ₁ -O ₂₃	2.598(6)
Ba-O ₁₂	3.160(3)	Ca ₁ -O ₁₃	2.760(7)
Ba-O ₁₂	3.160(3)	Ca ₂ -O ₁₁	2.303(4)
Ba-O ₁₂	3.160(3)	Ca ₂ -O ₁₃	2.366(5)
Ba-O ₁₃	3.438(7)	Ca ₂ -O ₂₂	2.388(6)
Ba-O ₁₃	3.438(7)	Ca ₂ -O ₁₂	2.392(7)
		Ca ₂ -O ₂₃	2.442(7)
		Ca ₂ -O	2.506(2)
		Ca ₂ -O ₂₁	2.548(7)

It was found out that the combination of higher anion polarizability and highly distorted polyhedral structure around Eu^{2+} or Ce^{3+} ions can generate stronger crystal fields, lowering the $5d$ energy level of Eu^{2+} or Ce^{3+} ions in the previous chapters. Figure 7-8 shows the coordination geometry around the oxygen ion explaining the different polarization. The isolated oxygen ion of CBP or TTCP can be much more polarizable than the one in phosphate. It is because the isolated oxygen ions are not coordinated by the phosphorous, to which oxygen ions can be bound strongly, as seen in ECoN values around oxygen ions. The large deviation in the coordination number from nominal to effective indicates the degree of distortion showing the oxygen ion in phosphate is so different from others. It is believed that isolated oxygen ions in CBP can contribute the unusual longer excitation wavelength, which matches to blue LEDs.

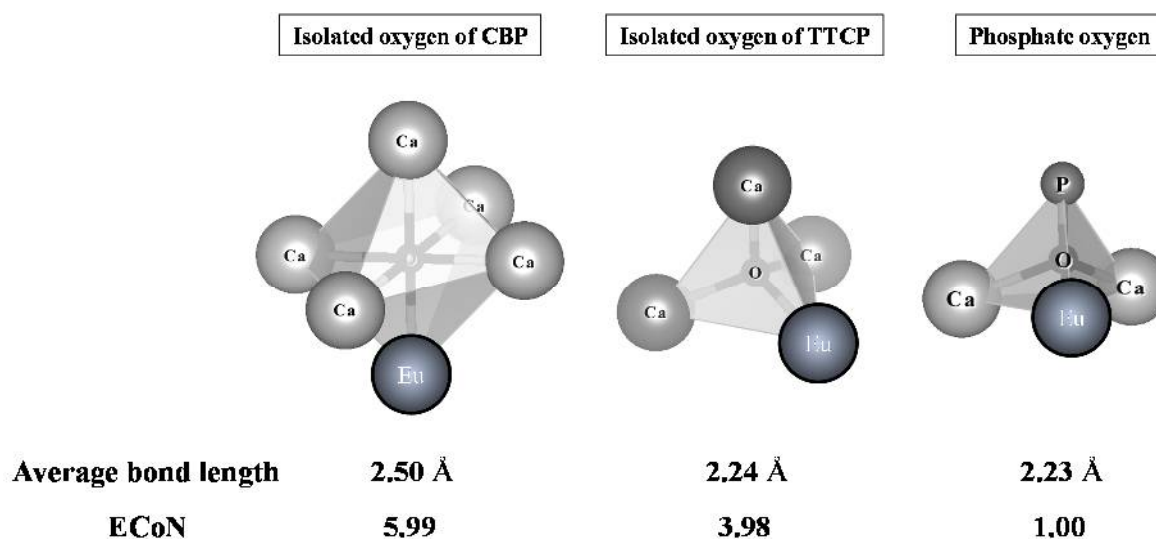


Figure 7-8 Comparison of the coordination geometries around oxygen ions in CBP, TTCP and phosphate tetrahedron with the substitution of Eu^{2+} ions.

7.3.2 Optical properties of $\text{Ca}_6\text{Ba}(\text{PO}_4)_4\text{O}:\text{Eu}^{2+}$

It was unable to determine the distribution of Eu^{2+} in CBP directly, as stated above, but it is believed that Eu^{2+} ions substitute at the Ca sites. The ionic radius of the twelve-coordinated Ba is 1.61 Å, and the ionic radii of the seven and eight-coordinated Ca are 1.06 and 1.12 Å, respectively. Considering the ionic radii of seven and eight-coordinated Eu^{2+} , which are 1.20 and 1.25 Å, respectively, random occupation of Eu into the two Ca sites can be expected. The emission characteristics support this behavior. There are only minor changes in the observed emission spectra for excitation wavelengths of 365 nm and 465 nm, even at liquid nitrogen temperatures, which indicates that the PL spectra are not contributed to by emissions from sites with significantly different crystal fields, i.e. the Ca and Ba sites (since the emissions from sites with significantly different crystal fields show different colors when the excitation wavelength is varied). Furthermore, Ba induces a somewhat weaker crystal field than Ca, and the Ba site is normally too large to achieve yellow emission in phosphates.¹⁷

Figure 7-9 shows the PL and PL excitation spectra for $\text{CBP}:\text{Eu}^{2+}$ at 0.9 mol% doping with respect to Ca, compared with $\text{YAG}:\text{Ce}^{3+}$. $\text{CBP}:\text{Eu}^{2+}$ has a broad yellow emission spectrum with the peak position at 553 nm and a full width at half maximum of 132 nm, wider than the 127 nm from the commercial yellow-emitting $\text{YAG}:\text{Ce}^{3+}$ (P46-Y3); it can therefore contribute a higher Ra to LED fabrication. The emission at 553 nm corresponds to the $4f^7 - 4f^65d^1$ transition of the Eu^{2+} ions. The Stokes shift is estimated to be around 3700 cm^{-1} and the color coordinates on the CIE chromaticity diagram is (0.428, 0.545). The broad band excitation is a good

fit to the requirements for a light color conversion phosphor excited by near UV to blue light, whereas $\text{YAG}:\text{Ce}^{3+}$ is restricted to blue applications alone.

When comparing excitation spectra among $\text{Ca}_3(\text{PO}_4)_2$, $\text{Ca}_4(\text{PO}_4)_2\text{O}$ and $\text{Ca}_6\text{Ba}(\text{PO}_4)_4\text{O}$, only $\text{Ca}_3(\text{PO}_4)_2$ cannot be excited by the blue LED. In the chemical formulae, $\text{Ca}_4(\text{PO}_4)_2\text{O}$ and $\text{Ca}_6\text{Ba}(\text{PO}_4)_4\text{O}$ contain isolated O^{2-} ions whereas $\text{Ca}_3(\text{PO}_4)_2$ does not. The isolated oxide ion is more polarizable than oxygen in PO_4 and we believe that this structural feature is responsible for the centroid shift which enables $\text{Ca}_4(\text{PO}_4)_2\text{O}$ and $\text{Ca}_6\text{Ba}(\text{PO}_4)_4\text{O}$ to be excited in the blue.¹⁸

The emission of $\text{CBP}:\text{Eu}^{2+}$ was deconvoluted into two components attributed to the Ca1 and Ca2 sites, as shown in Figure 7-10. The Ca1 site shows shorter wavelength emission centered at 536 nm since it is affected by the weaker crystal field of the eight-coordinated site (average M-O bond lengths 2.51 Å). By contrast, Ca2 exhibits longer wavelength emission centered at 589 nm due to the stronger crystal field associated with the seven-coordinated site (average M-O bond length 2.42 Å).

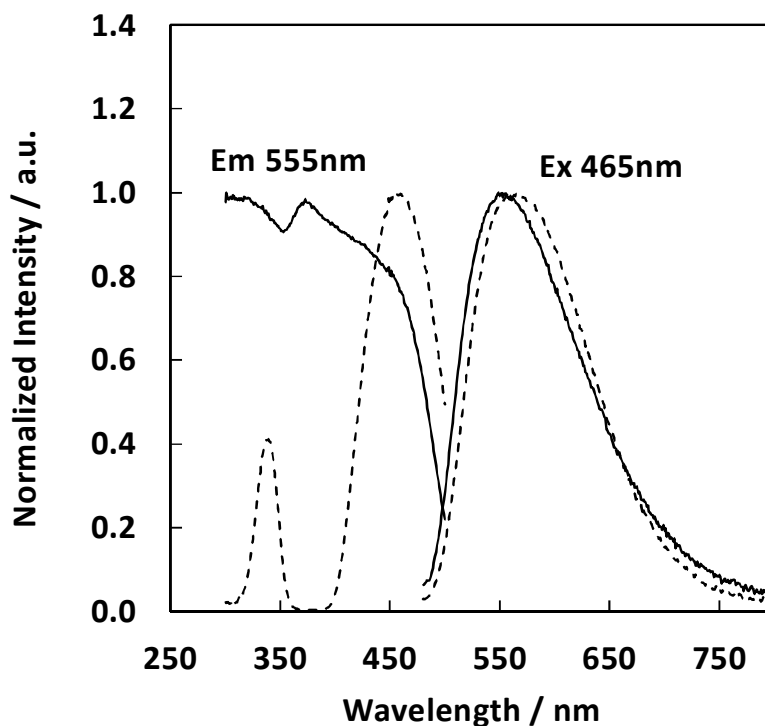


Figure 7-9 PL and PL excitation spectra of CBP activated with 0.9 mol% of Eu^{2+} (solid line) and $\text{YAG}:\text{Ce}^{3+}$ (dashed line).

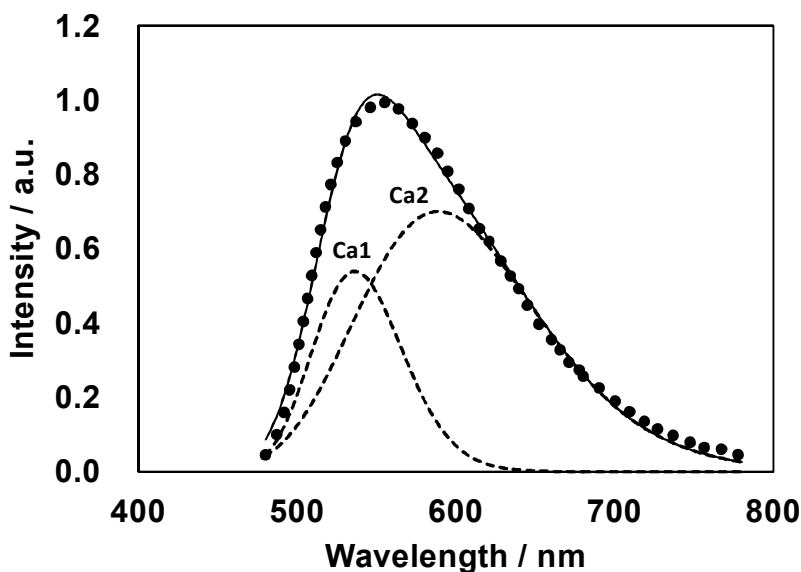


Figure 7-10 Deconvoluted emission spectra of $\text{CBP}:\text{Eu}^{2+}$. Observed (dotted line), fitted curve (solid line) and deconvoluted Gaussian components for Ca1 and Ca2 site (dashed line).

The optimum doping level of $\text{CBP}:\text{Eu}^{2+}$ was found to be 1-2 mol% with respect to the Ca site, and the emission color showed a linear shift in CIE color coordinates as a function of Eu^{2+} (Figure 7-11). The previously reported internal quantum efficiency of P46-Y3 is about 86 %, ¹⁹ and based on this value the internal quantum efficiency of $\text{CBP}:\text{Eu}^{2+}$ is about 65 %, considerably higher than the values reported for $\text{Ca}_4(\text{PO}_4)_2\text{O}:\text{Eu}^{2+}$ (37.5 %) and $(\text{Ca,Ba})_3(\text{PO}_4)_2:\text{Eu}^{2+}$ (40.7 %). ^{20,21}

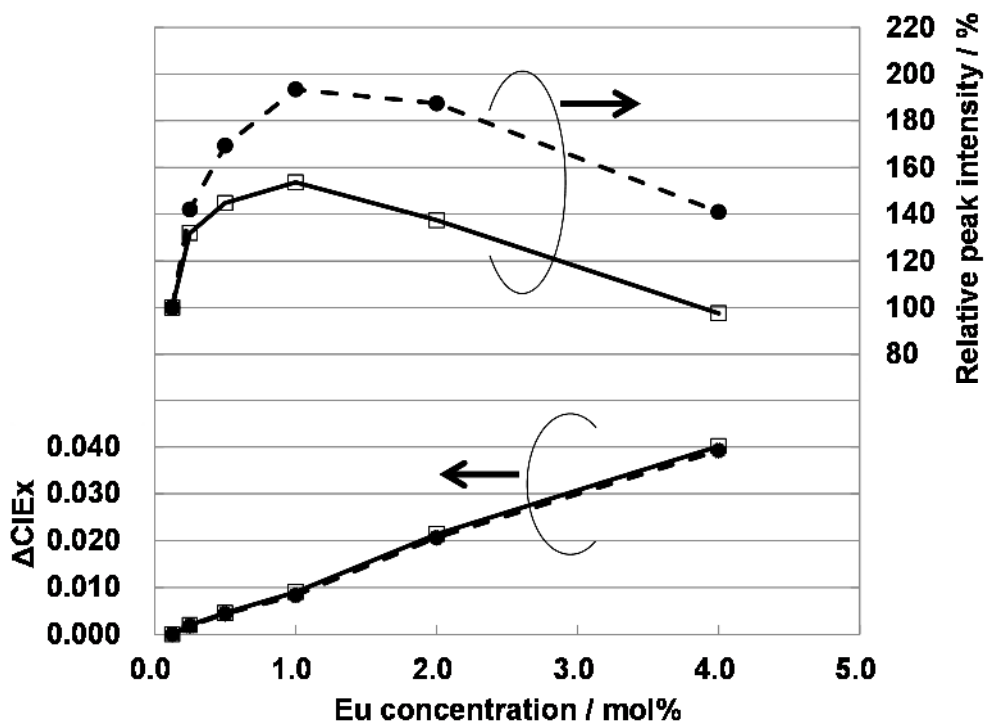


Figure 7-11 Relative peak intensity and color shift as a function of Eu concentration. □:Ex.400 nm, ●:Ex.465 nm.

Figure 7-12 shows the reflectance spectra of undoped and Eu-doped CBP. The reflectance of undoped CBP remains at about 90 % in the spectral range of 250-750 nm, with a sudden drop below 250 nm corresponding to the absorption at the bandgap in CBP. The Eu^{2+} doping introduces a strong, broad absorption in the range 200-500 nm associated with its $4f^7 - 4f^65d^1$ transition.

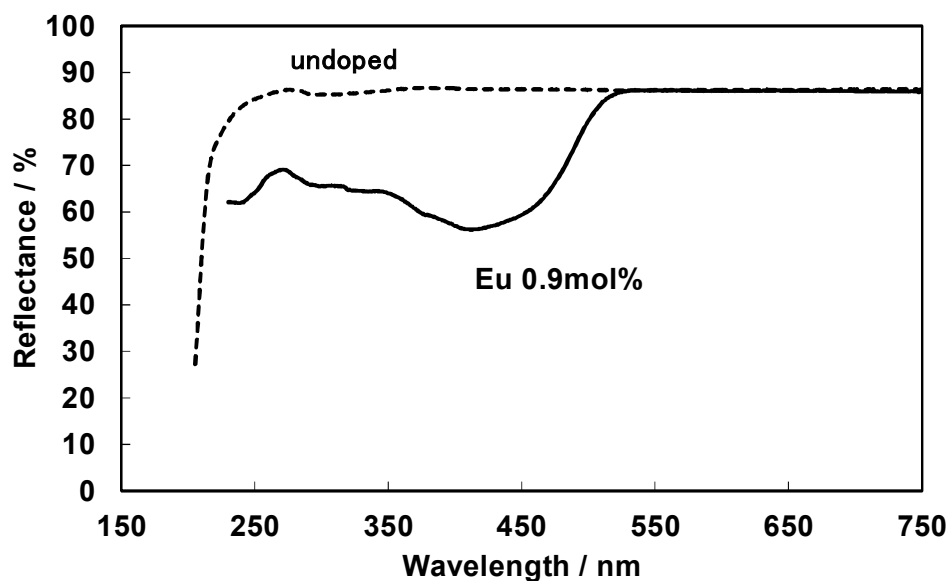


Figure 7-12 Reflectance spectra of an undoped CBP sample (dashed line) and a sample doped with 0.9 mol% of Eu (solid line).

Absorption spectra calculated from the Kubelka-Munk function are shown in Figure 7-13,²² from which the value of the optical bandgap, E_g , was estimated to be about 5.8 eV, compared with the reported bandgap of 5.0 eV for $\text{Ba}_2\text{Ca}(\text{PO}_4)_2$.²¹ The value for CBP is much larger than reported value, which can help to enable CBP to maintain bright emission at room temperature, and compares well with the calculated bandgap of 6.2 eV derived using the meta-GGA method implemented in ABINIT package interfacing with the Libxc library.^{23,24}

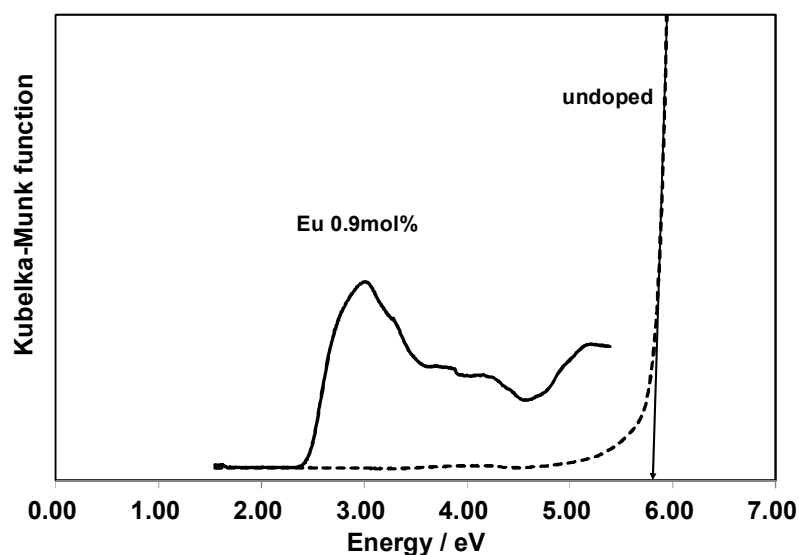


Figure 7-13 Absorption spectra of an undoped sample (dashed line) and a sample doped with 0.9 mol% of Eu (solid line).

7.3.3 Temperature dependence of the photoluminescence

Figure 7-14 shows the temperature dependence of the photoluminescence of $\text{CBP}:0.012 \text{Eu}^{2+}$ excited at 455 nm. This quenching behavior can be a disadvantage for a practical use since this is a little stronger than YAG. The luminescence intensity of $\text{P46-Y3}:\text{Ce}^{3+}$ ($\text{YAG}:\text{Ce}^{3+}$) decreases by 60 % as the temperature increases from 25 to 150 °C.

The temperature dependence of PL was measured with $\text{CBP}:\text{Eu}^{2+}$ (1 mol% substitution) from 75 K to 300 K (Figure 7-15). When temperature increased, it showed a clear blue shift in emission peak wavelength as $\text{TTCP}:\text{Eu}^{2+}$ and $\text{TTSP}:\text{Eu}^{2+}$ presented, which can also be explained by a thermally active phonon-assisted tunneling from the excited states of the lower $5d$ energy level to the excited states of the higher $5d$ energy level.²⁵ To support this explanation, PL and PLE at room temperature and 77 K were normalized and compared in Figure 7-16. There was no change in the shape of excitation spectra between room temperature and 77 K, whereas emission peaks shift, confirming there is no change in the crystal field around Eu^{2+} ions.

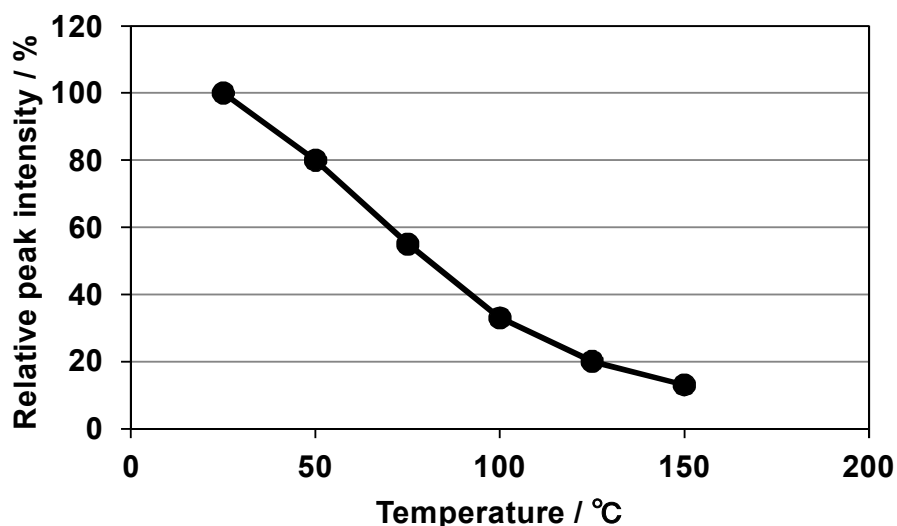


Figure 7-14 Temperature dependence of the photoluminescence of $\text{CBP}:0.012 \text{Eu}^{2+}$ excited at 455 nm.

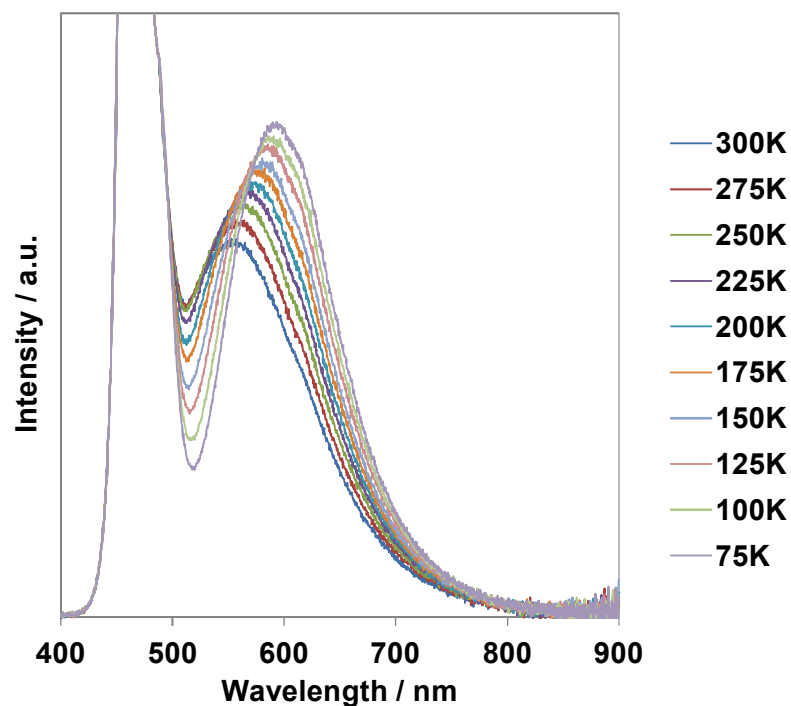


Figure 7-15 PL of CBP activated with 1 mol% of Eu^{2+} , excited by 470 nm blue LED light at lower temperature from 75 K to 300 K.

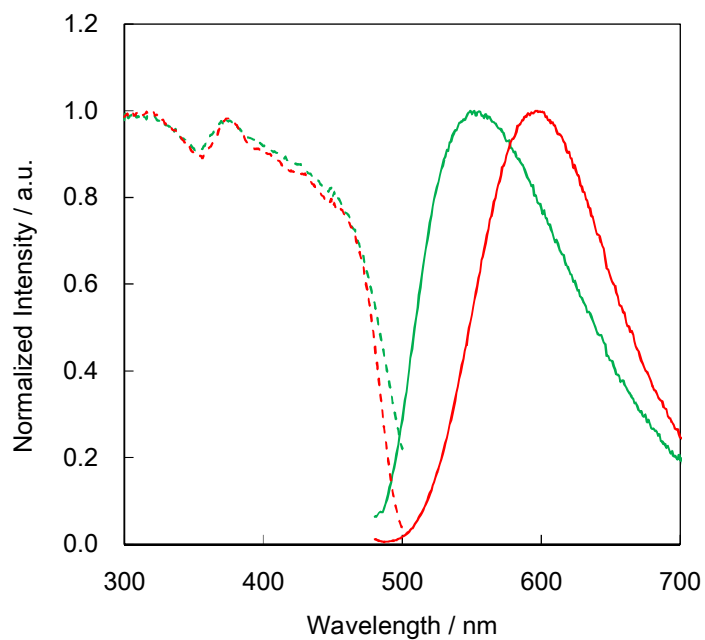


Figure 7-16 PL (solid line) and PLE (dashed line) spectra of CBP activated with 0.9 mol% of Eu^{2+} at room temperature (green) and 77 K (red).

7.3.4 Luminescence from a white LED

The $\text{CBP}:\text{Eu}^{2+}$ phosphor is very suitable as a color converter for a white LED because of its blue light absorption and yellow light emission. The phosphor has a strong, deep yellow color in natural light (Figure 7-17a), and a fabricated LED is also shown, both as-prepared (Figure 7-17b) and in operation (Figure 7-17c). Figure 7-18 shows the luminescence spectrum of a white LED consisting of a blue InGaN LED and $\text{CBP}:\text{Eu}^{2+}$. Its correlated color temperature (CCT) was 6500 K and the CIE color coordinates were (0.312, 0.344). The luminous efficacy of the LED, η , external quantum efficiency of the LED, and the average color rendering index, R_a , at a high forward current of 350 mA were 31 lmW^{-1} , 10 % and 78, respectively, whereas a white LED with $\text{YAG}:\text{Ce}^{3+}$ normally reaches only 75 in R_a .³ For further comparison, the reported values for white LEDs comprising of a blue LED and a yellow phosphor are $R_a = 70.3$, $\eta = 50.7 \text{ lmW}^{-1}$ at CCT = 3722 K for $\text{CaAlSiN}_3:\text{Ce}^{3+}$ and $R_a = 72$, $\eta = 43 \text{ lmW}^{-1}$ at CCT = 6150 K for $\text{Li-}\alpha\text{-SiAlON}:\text{Eu}^{2+}$.^{6,26} $\text{CBP}:\text{Eu}^{2+}$ therefore shows significant potential as a white LED phosphor, balancing η and R_a . $\text{CBP}:\text{Eu}^{2+}$ can achieve a high R_a without using an additional phosphor covering the red light component.^{20,21}



Figure 7-17 (a) new yellow phosphor; (b) as-prepared LED; (c) LED in operation.

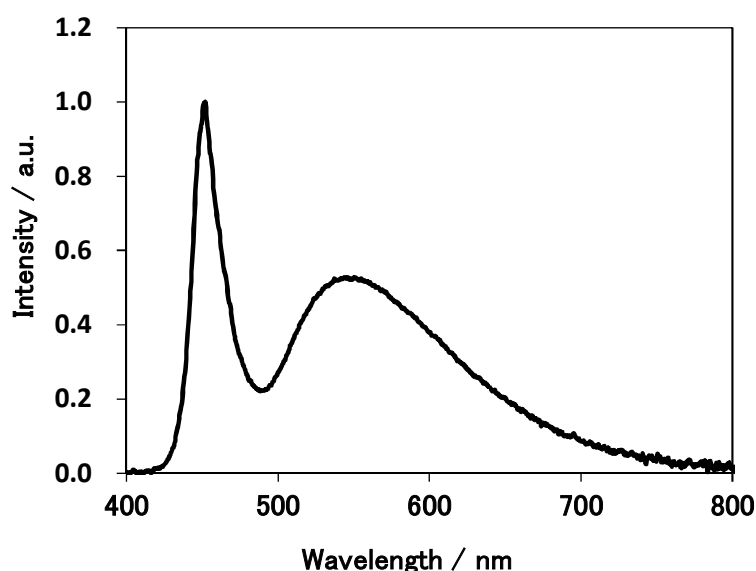


Figure 7-18 Luminescence spectrum of a white LED consisting of a blue LED and the $\text{CBP}:\text{Eu}^{2+}$ phosphor.

7.4 Summary

A new yellow phosphor, $\text{Ca}_6\text{Ba}(\text{PO}_4)_4\text{O}:\text{Eu}^{2+}$, has been discovered. The unknown structure of $\text{Ca}_6\text{Ba}(\text{PO}_4)_4\text{O}$ was solved *ab initio* from synchrotron X-ray powder diffraction data and the bandgap of CBP was estimated to be about 5.8 eV. When combined with a blue InGaN LED, $\text{CBP}:\text{Eu}^{2+}$ shows good characteristics, which are suitable for a white LED, with a broad excitation band from the near-UV to the blue region, and strong yellow emission with a peak position at 553 nm. Because the emission of $\text{CBP}:\text{Eu}^{2+}$ is broader and red-shifted compare with other yellow oxide phosphors, the color rendering index of white LEDs based on $\text{CBP}:\text{Eu}^{2+}$ is superior to those other systems.

7.5 References

- 1 S. Nakamura, S. Pearton and G. Fasol, *The Blue Laser Diode : The Complete Story*, pp. 230-235, Springer-Verlag, Berlin 2000.
- 2 K. Bando, K. Sakano, Y. Noguchi and Y. Shimizu, *J. Light & Vis. Env.*, 1998, **22**, 2.
- 3 H. S. Jang, Y. H. Won and D. Y. Jeon, *Appl. Phys. B: Lasers Opt.*, 2009, **95**, 715.
- 4 T. L. Barry, *J. Electrochem. Soc.: SOLID STATE SCIENCE*, 1968, **115**, 1181.
- 5 K. Sakuma, N. Hirosaki and R.-J. Xie, *J. Lumin.*, 2007, **126**, 843.
- 6 Y. Q. Li, N. Hirosaki, R.-J. Xie, T. Takeda and M. Mitomo, *Chem. Mater.*, 2008, **20**, 6704.
- 7 M. Yashima and Y. Kawaike, *Chem. Mater.*, 2007, **19**, 3973.
- 8 P. A. Henning, A. R. Landa-Canovas, A.-K. Larsson and S. Lidin, *Acta Crystallogr., Sect. B: Struct. Sci.*, 1999, **B55**, 170.
- 9 B. Dickens, W. E. Brown, G. J. Kruger and J. M. Stewart, *Acta Crystallogr., Sect. B: Struct. Sci.*, 1973, **B29**, 2046.
- 10 C. C. Lagos, *J. Electrochem. Soc.: SOLID STATE SCIENCE*, 1970, **117**, 1189.
- 11 N. Komuro, M. Mikami, Y. Shimomura, E. G. Bithell and A. K. Cheetham, *J. Mater. Chem. C*, 2014, **2**, 6084.
- 12 S. P. Thompson, J. E. Parker, J. Potter, T. P. Hill, A. Birt, T. M. Cobb, F. Yuan, and C. C. Tang, *Rev. Sci. Instrum.*, 2009, **80**, 075107.
- 13 V. Favre-Nicolin and R. Cerny, *J. Appl. Crystallogr.*, 2002, **35**, 734.
- 14 A.C. Larson and R. B. Von Dreele, "General Structure Analysis System (GSAS)", Los Alamos National Laboratory Report LAUR 86-748, 1994.
- 15 B. H. Toby, *J. Appl. Crystallogr.*, 2001, **34**, 210.
- 16 K. Momma and F. Izumi, *J. Appl. Crystallogr.*, 2011, **44**, 1272.
- 17 P. Dorenbos, *J. Lumin.*, 2003, **104**, 239.
- 18 M. Mikami and N. Kijima, *Opt. Mater.*, 2010, **33**, 145; M. Mikami, *ECS J. Solid State Sci. Technol.*, 2013, **2**, R3048.
- 19 B.-G. Yun, Y. Miyamoto and H. Yamamoto, *J. Electrochem. Soc.*, 2007, **154**, J320.
- 20 D. Deng, H. Yu, Y. Li, Y. Hua, G. Jia, S. Zhao, H. Wang, L. Huang, Y. Li, C. Li and S. Xu, *J. Mater. Chem. C*, 2013, **1**, 3194.
- 21 H. Yu, D. Deng, D. Zhou, W. Yuan, Q. Zhao, Y. Hua, S. Zhao, L. Huang and S. Xu, *J. Mater. Chem. C*, 2013, **1**, 5577.
- 22 C. J. Duan, A. C. A. Delsing and H. T. Hintzen, *Chem. Mater.*, 2009, **21**, 1010.
- 23 X. Gonze, J.-M. Beuken, R. Caracas, F. Detraux, M. Fuchs, G.-M. Rignanese, L. Sindic, M. Verstraete, G. Zerah, F. Jollet, M. Torrent, A. Roy, M. Mikami, Ph. Ghosez, J.-Y. Raty and D. C. Allan, *Comput. Mater. Sci.*, 2002, **25**, 478; X. Gonze, B. Amadon, P. Anglade, J. Beuken, F. Bottin, P. Boulanger, F. Bruneval, D. Caliste, R. Caracas, M. Côté, T. Deutsch, L. Genovese, Ph. Ghosez, M. Giantomassi, S. Goedecker, S. D. R. Hamann, P. Hermet, F. Jollet, G. Jomard, S. Leroux, M. Mancini, S. Mazevet, M. J. T. Oliveira, G. Onida, Y. Pouillon, T. Rangel, G.-M. Rignanese, D. Sangalli, R. Shaltaf, M. Torrent, M. J. Verstraete, G. Zerah, and J. W. Zwanziger, *Comput. Phys. Commun.* 2009,

- 180**, 2582; D. Waroquiers, A. Lherbier, A. Miglio, M. Stankovski, S. Poncé, M. J. T. Oliveira, M. Giantomassi, G.-M. Rignanese, and X. Gonze, *Phys. Rev. B*, 2013, **87**, 075121.
- 24 M.A.L. Marques, M.J.T. Oliveira and T. Burnus, *Comp. Phys. Commun.*, 2012, **183**, 2272.
- 25 C. C. Lin, Y. S. Zheng, H. Y. Chen, C. H. Ruan, G. W. Xiao and R. S. Liu, *J. Electrochem. Soc.*, 2010, **157**, H900.
- 26 R.-J. Xie, N. Hirosaki and M. Mitomo, *Appl. Phys. Lett.*, 2006, **88**, 101104.

Chapter 8 Blue-green luminescence of $\text{Ca}_6\text{Ba}(\text{PO}_4)_4\text{O}:\text{Ce}^{3+}$

A new blue-green phosphor, $\text{Ca}_6\text{Ba}(\text{PO}_4)_4\text{O}:\text{Ce}^{3+}$, which can be prepared by conventional solid-state synthesis, is reported as a candidate phosphor for SSL with near-ultraviolet LEDs. Under excitation at around 400 nm, $\text{Ca}_6\text{Ba}(\text{PO}_4)_4\text{O}:\text{Ce}^{3+}$ shows strong blue-green emission with the peak position at 477 nm. $\text{Ce}^{3+},\text{Si}^{4+}$ co-doping is found to enhance the luminous intensity, and the unique emission characteristics of this combination are studied and related to the crystal structure. $\text{Ca}_6\text{Ba}(\text{PO}_4)_4\text{O}$ is an exceptional host material, which also accommodates Eu^{2+} , emitting strong yellow light under 400 nm excitation. A fabricated white LED, combining $\text{Ca}_6\text{Ba}(\text{PO}_4)_4\text{O}:\text{Ce}^{3+},\text{Si}^{4+}$ with $\text{Ca}_6\text{Ba}(\text{PO}_4)_4\text{O}:\text{Eu}^{2+}$ and a red $\text{CaAlSiN}_3:\text{Eu}^{2+}$ phosphor, achieved a luminous efficacy of 45 lmW^{-1} with a color rendering index of 93 around the correlated color temperature of 4500 K.

8.1 Introduction

Many Ce^{3+} -containing phosphors, including oxides, sulfides, and nitrides, have been proposed as color-converting materials for SSL. However, only a few Ce^{3+} -doped oxide phosphors are genuine candidates for white LEDs since oxide hosts rarely offer excitation in the near-UV or blue part of the spectrum. The garnet system, $\text{YAG}:\text{Ce}^{3+}$, is an important exception, exhibiting a large red shift in the $5d$ energy level of Ce^{3+} such that it absorbs in the blue and emits in the yellow.¹ It plays an important role in SSL based upon blue LEDs emitting at 460 nm. However, its excitation band matches to only blue light and restricts its application for near-UV. The luminescence of Ce^{3+} in perovskite hosts such as CaHfO_3 , LaScO_3 and GdScO_3 is more typical of oxide systems;² the wavelength of the Ce^{3+} excitation band in these materials extends up to around 350 nm, but it is too short to meet the excitation wavelength range for near-UV LEDs at about 400 nm. In terms of Ce^{3+} -doped oxide phosphors that can be excited at around 400 nm and emit in the visible, among the few examples are $\text{Sr}_2\text{Ba}(\text{AlO}_4\text{F})_{1-x}(\text{SiO}_5)_x:\text{Ce}^{3+}$ and $\text{Ba}_9\text{Y}_2\text{Si}_6\text{O}_{24}:\text{Ce}^{3+}$, the latter exhibiting a quantum efficiency of 60 % for emission across a broad part of the visible spectrum.^{3,4}

In Chapter 7, the discovery and crystal structure of CBP was introduced and the potential of its Eu^{2+} -activated derivative for use as a phosphor in SSL was also explored. $\text{CBP}:\text{Eu}^{2+}$ emits a strong yellow light under excitation from the near-UV to the blue.⁵ In this chapter, $\text{CBP}:\text{Ce}^{3+}$ phosphor is introduced for a near-UV LED which proves to be an exceptional Ce-based blue-green phosphate phosphor showing bright emission with a high internal quantum yield. This can be the first report of a Ce-doped phosphate phosphor enabling excitation with a near-UV LED. Co-doped $\text{CBP}:\text{Ce}^{3+},\text{Si}^{4+}$ phosphors have also been prepared and enhance the blue-green emission for the high Ce concentration region, substituting the P site with Si. The unique emission performance was investigated due to the lattice expansion accompanying an increasing Ce,Si co-doping concentration. It is possible to correlate the unit cell volume of CBP host lattice with the position of the lowest Ce^{3+} $4f-5d$ transition.

The CBP host is one of the few phosphors that can accommodate both Eu^{2+} and Ce^{3+} with different emission colors when excited with a near-UV LED. Phosphors co-doped with Ce^{3+} and Eu^{2+} , such as $\text{CaAl}_2\text{Si}_2\text{O}_8$,⁶ $\text{Li}_2\text{SrSiO}_4$,⁷ $\text{Ca}_8\text{La}_2(\text{PO}_4)_6\text{O}_2$,⁸ have been proposed before, but none are well adapted for near-UV LEDs. In the present work, the luminous efficacy of a white LED fabricated by combining $\text{CBP}:\text{Ce}^{3+},\text{Si}^{4+}$, $\text{CBP}:\text{Eu}^{2+}$, $\text{CaAlSiN}_3:\text{Eu}^{2+}$ and a near-UV LED was 45 lmW^{-1} with a color rendering index, Ra, of 93.

8.2 Experimental

8.2.1 Synthetic procedures

Phase pure samples of $\text{CBP}:\text{Ce}^{3+}$ were synthesized by conventional solid-state reaction between CaCO_3 (Hakushin Chemicals), BaCO_3 (Hakushin Chemicals), CaHPO_4 (Alfa Aesar) and CeO_2 (Alfa Aesar). The ground mixtures of the starting materials were placed in alumina crucibles and heated in a reducing atmosphere of 5 % H_2 + 95 % N_2 in the range of 1250-1300 °C for 10 hrs. $\text{CBP}:\text{Ce}^{3+},\text{Si}^{4+}$ Co-doped samples were readily prepared by adding SiO_2 (Tatsumori) to the starting materials, with the same synthesis conditions as those for $\text{CBP}:\text{Ce}^{3+}$. Co-doping samples were substituted in the chemical formula of $(\text{Ca}_{1-x}\text{Ce}_x)_6\text{Ba}(\text{P}_{1-6x/4}\text{Si}_{6x/4}\text{O}_4)_4\text{O}$ considering the charge balance. After synthesis, the samples were crushed into fine powders for characterization.

8.2.2 Crystallography and optical characterization

Laboratory powder X-ray diffraction (PXRD) data were obtained on a PANalytical X'Pert Powder diffractometer (Bragg–Brentano geometry) using $\text{Cu-K}\alpha$ radiation and a position sensitive detector (X'Celerator) with a step size of 0.02° in the range of $2\theta = 10\text{--}120^\circ$. Calculations of the unit cell volumes were carried out with the nonlinear, least-squares cell-refinement program, UNITCELL.⁹ The crystal structure of CBP was depicted in VESTA.¹⁰

Photoluminescence and photoluminescence excitation spectra at room temperature were measured using a Horiba FluoroLog-3 spectrometer and a Hitachi spectrometer (model F4500). The UV-vis reflectance spectra were measured on a PerkinElmer Lambda 750 spectrophotometer. The photoluminescence quantum efficiency was measured from PL measurements with an integrating sphere equipped with a 150 W Xe lamp and a multichannel spectrophotometer (model MCPD7000; Otsuka Electronics). The temperature-dependence of the photoluminescence was measured using a multichannel spectrophotometer (model MCPD7000; Otsuka Electronics).

8.2.3 White LED fabrication

White LEDs were fabricated by embedding the $\text{Ca}_6\text{Ba}(\text{PO}_4)_4\text{O}:\text{Ce}^{3+},\text{Si}^{4+}$ (blue-green), $\text{Ca}_6\text{Ba}(\text{PO}_4)_4\text{O}:\text{Eu}^{2+}$ (yellow) and $\text{CaAlSiN}_3:\text{Eu}^{2+}$ (red) phosphors in a transparent silicone resin; the down-converter was packaged with 1 W InGaN LED chips, targeting a correlated color temperature of around 4500 K.

8.3 Results and discussion

8.3.1 Phase identification

The as-prepared powder of CBP is white for the pure sample with a slightly bluish tinge for doped samples. The body colors of the samples become grayish as the Ce concentration increases. Some defects may have been induced by the substitution of the divalent site with trivalent Ce^{3+} .

There is no JCPDS ICDD PDF for CBP since the structure of CBP has only recently been solved in the previous work.⁵ The phase identification was achieved by comparing the PXRD pattern from $\text{CBP}:\text{Ce}^{3+}$ with that from $\text{CBP}:\text{Eu}^{2+}$. As shown in Figure 8-1, the PXRD pattern for $\text{CBP}:\text{Ce}^{3+}$ is indistinguishable from the one for $\text{CBP}:\text{Eu}^{2+}$.

CBP has a monoclinic structure in space group $C2/m$ with a single Ba site and two Ca sites (Figure 8-2).⁵ The Ba site is coordinated by twelve oxygen atoms with an average bond length of 3.04 Å, the Ca1 site by eight oxygen atoms with an average bond length of 2.51 Å, and the Ca2 site by seven oxygen atoms with an average bond length of 2.42 Å. Schematic illustrations of the coordination around the Ba and Ca sites are depicted in Figure 8-3. The two P sites are in PO_4 tetrahedra, which are isolated from other PO_4 tetrahedra. The structure also contains an oxide ion that is not part of a PO_4 tetrahedron; it is coordinated to Ca1 and Ca2, but not to Ba.

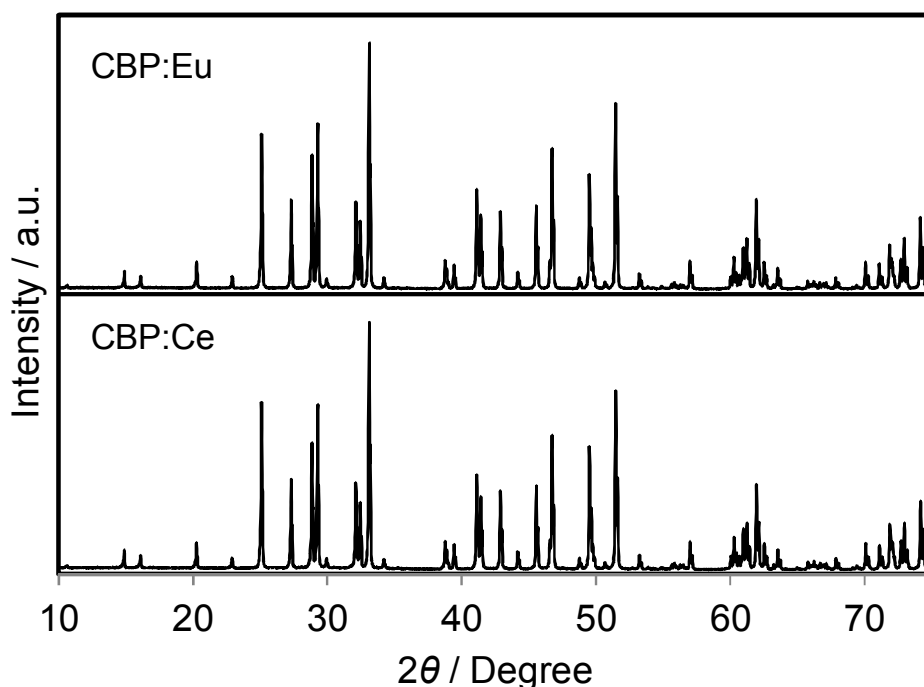


Figure 8-1 Experimental PXRD patterns of $\text{CBP}:\text{Eu}$ and $\text{CBP}:\text{Ce}$ in the range of $2\theta = 10\text{--}75^\circ$.

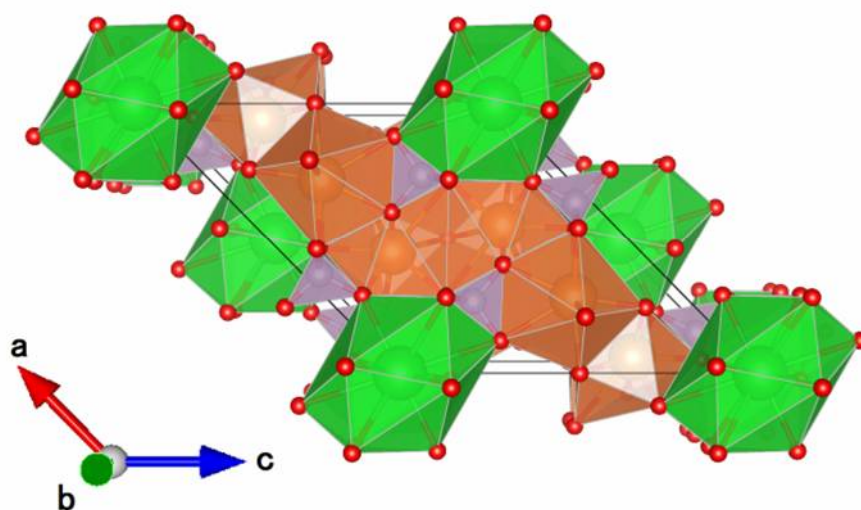


Figure 8-2 Schematic crystal structure illustrations of CBP projected onto the (010) plane. Ba is green, Ca is brown, P is mauve and oxygen is red.

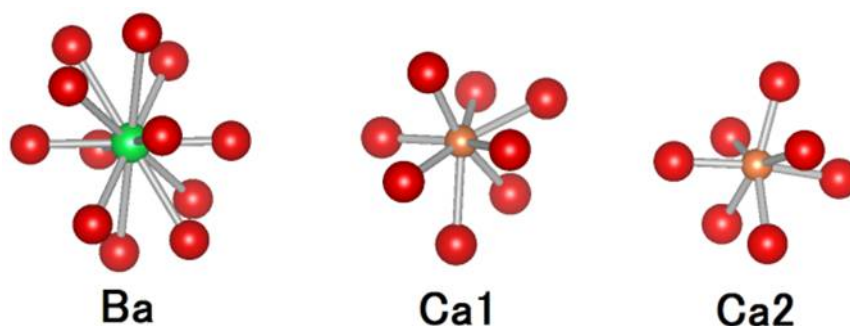


Figure 8-3 Comparison of the coordination geometries around the Ba site, the Ca1 site and the Ca2 site. Colors as in Figure 8-2.

8.3.2 Optical properties of $\text{Ca}_6\text{Ba}(\text{PO}_4)_4\text{O}:\text{Ce}^{3+}$

Figure 8-4 presents the excitation and emission spectra of $\text{CBP}:\text{Ce}^{3+}$ at 1.8 mol% doping with respect to Ca, compared to the commercially available, typical blue phosphor $\text{BaAlMg}_{10}\text{O}_{17}:\text{Eu}^{2+}$ (LP-B4). $\text{CBP}:\text{Ce}^{3+}$ has a broad blue-green emission spectrum with the peak position at 477 nm and a full width at half maximum of 98 nm, wider than the 53 nm from the BAM; it can therefore contribute a higher Ra to LED fabrication. Figure 8-5 shows the excitation and emission spectra of $\text{CBP}:\text{Ce}^{3+}$ at different doping level with respect to Ca. The doublet emission band is indicative of typical Ce^{3+} luminescence and can be fitted by two Gaussians separated by 2000 cm^{-1} as shown in Figure 8-6. The emission at 477 nm corresponds to the $5d \rightarrow 4f$ transition of the Ce^{3+} ions. The maximum of the excitation band is at 370 nm giving a Stokes shift of about 5300 cm^{-1} . The color coordinates on

the CIE chromaticity diagram are (0.172, 0.267).

It was unable to determine the distribution of Ce^{3+} in CBP directly from the PXRD, but it is believed that it substitutes at the Ca sites. The ionic radius of the twelve-coordinated Ba is 1.61 Å, and the ionic radii of the seven and eight-coordinated Ca are 1.06 and 1.12 Å. Considering the ionic radii of seven, eight and twelve-coordinated Ce^{3+} , which are 1.07, 1.14 and 1.34 Å, respectively, occupation of Ce^{3+} at the two Ca sites can be expected.¹¹ According to the following empirical Equation 8-1 by Dorenbos, the absorption energy in eV can be approximately related for Ce^{3+} and Eu^{2+} dopants in the same host material, as long as both dopants sit in the same crystallographic site:¹²

$$E(\text{Eu}^{2+}, \text{CBP}) = (0.64 \pm 0.02) \times E(\text{Ce}^{3+}, \text{CBP}) + (0.53 \pm 0.06) \quad \text{Equation 8-1}$$

$E(\text{Eu}^{2+}, \text{CBP})$ and $E(\text{Ce}^{3+}, \text{CBP})$ represent the absorption energies of Eu and Ce in the CBP host. Based on this equation, the expected excitation peak wavelength of $\text{CBP}:\text{Eu}^{2+}$ is 467 nm as calculated from the excitation peak (373 nm) for $\text{CBP}:\text{Ce}^{3+}$. This agrees very well with the previous work on $\text{CBP}:\text{Eu}^{2+}$, which found an excitation maximum at 465 nm. Neglecting the contribution of the difference in Stokes shift between Eu^{2+} and Ce^{3+} , the emission peak wavelength of $\text{CBP}:\text{Eu}^{2+}$ can also be estimated from the emission wavelength (480 nm) of $\text{CBP}:\text{Ce}^{3+}$ using Equation 8-1. At 568 nm, this is close to the measured emission peak of 550 nm. By comparing Ce^{3+} and Eu^{2+} in excitation and emission, we conclude that both are in the same sites, surrounded by the similar ligand fields of the two Ca sites.

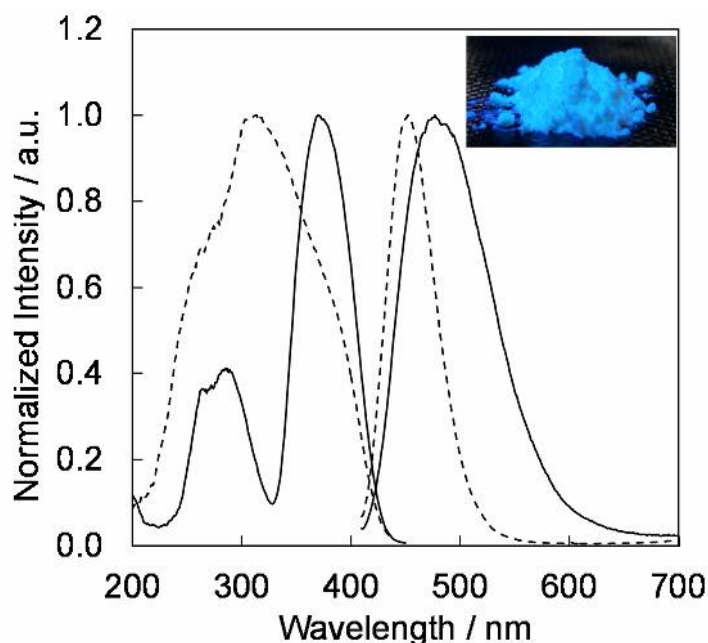


Figure 8-4 Photoluminescence and photoluminescence excitation spectra of CBP activated with 1.8 mol% of Ce^{3+} (solid line) and $\text{BaAlMg}_{10}\text{O}_{17}:\text{Eu}^{2+}$ (dashed line) excited at 400 nm. The inset shows a photograph of the $\text{CBP}:\text{Ce}^{3+}$ excited by a 400 nm LED.

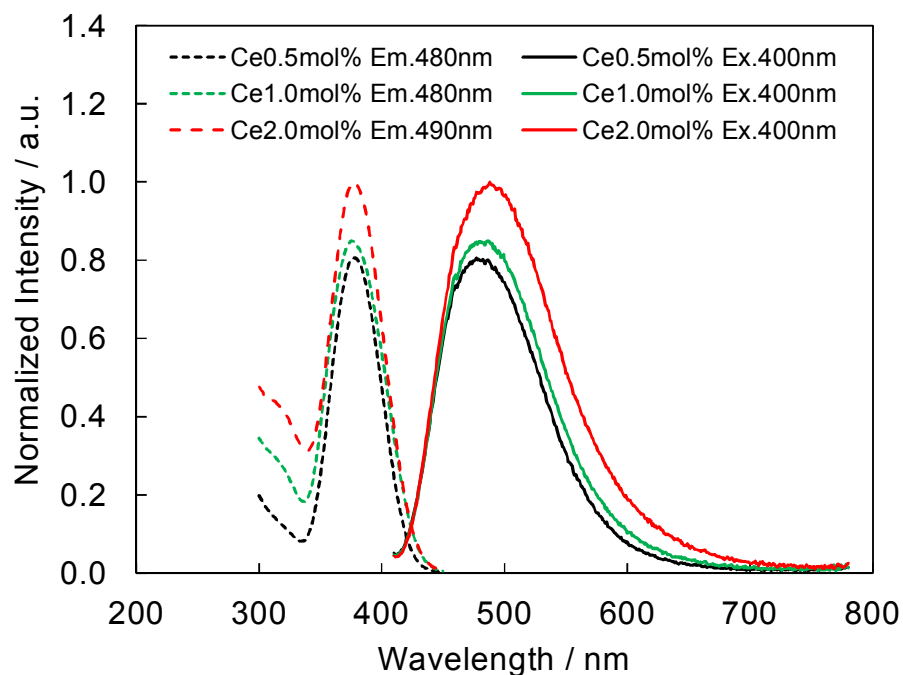


Figure 8-5 Photoluminescence (solid line) and photoluminescence excitation (dashed line) spectra of CBP activated with 0.5 mol%, 1.0 mol% and 2.0 mol% of Ce^{3+} .

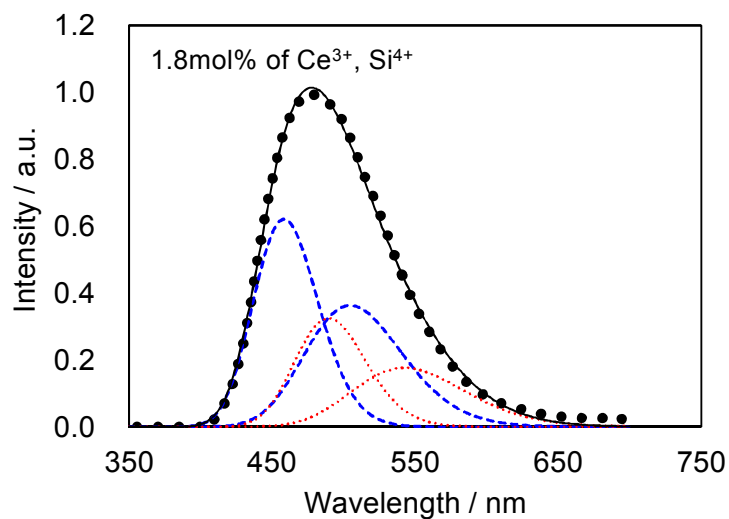


Figure 8-6 Decomposition of the Photoluminescence spectrum excited at 400 nm. Observed (dotted line), fitted curve (solid line) and deconvoluted Gaussian components for Ca1 site (blue dashed line) and Ca2 site (red dashed line).

8.3.3 Ce^{3+} , Si^{4+} co-doping in $\text{Ca}_6\text{Ba}(\text{PO}_4)_4\text{O}$

In an attempt to enhance the light conversion efficiency of the $\text{CBP}:\text{Ce}^{3+}$ phosphor, Ce^{3+} and Si^{4+} co-doping was performed, targeted the Ca and P sites, respectively. This co-doping effectively improved the emission peak intensity by as much as 100 % and maintained a high peak intensity over a wide Ce^{3+} concentration region, as shown in Figure 8-7. The co-doping suppressed the grayish sample color that develops with Ce doping alone; this can be attributed to preventing defect generation by forming charge-compensating pairs (Ca^{2+} substituted by Ce^{3+} and P^{5+} by Si^{4+}).

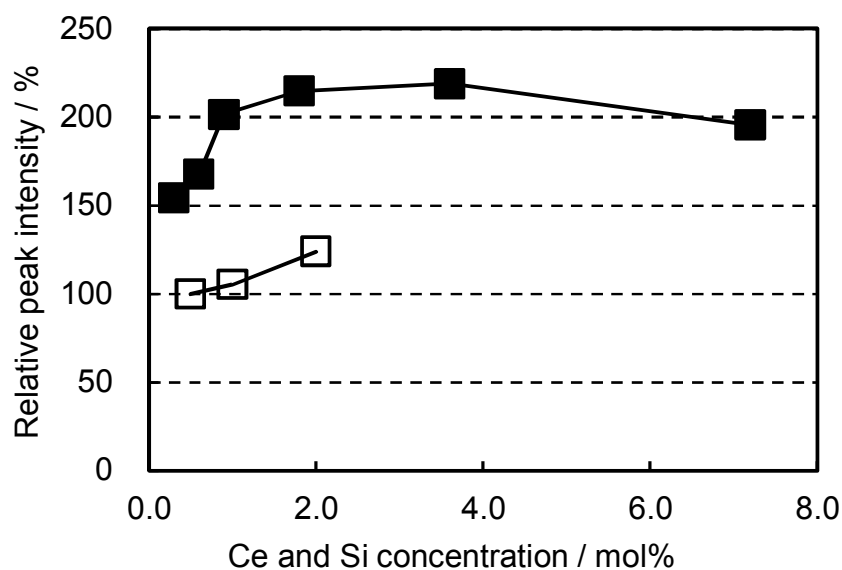


Figure 8-7 Relative peak intensity as a function of Ce concentration excited at 400 nm;

□: $(\text{Ca}_{1-x}\text{Ce}_x)_6\text{Ba}(\text{PO}_4)_4\text{O}$, ■: $(\text{Ca}_{1-x}\text{Ce}_x)_6\text{Ba}(\text{P}_{1-6x/4}\text{Si}_{6x/4}\text{O}_4)_4\text{O}$.

The co-doped samples also exhibit unique characteristics in the color shift as a function of $\text{Ce}^{3+}/\text{Si}^{4+}$ doping concentration. As presented in Figure 8-8, Ce^{3+} single doping shifts the emission color linearly with the doping level. In contrast to this, $\text{Ce}^{3+}/\text{Si}^{4+}$ co-doping showed a much smaller change in emission color with an increase of concentration. The linear shift of the emission color with increasing Ce^{3+} concentration is generally explained by the enhancement of reabsorption due to the overlap between absorption and emission.¹³

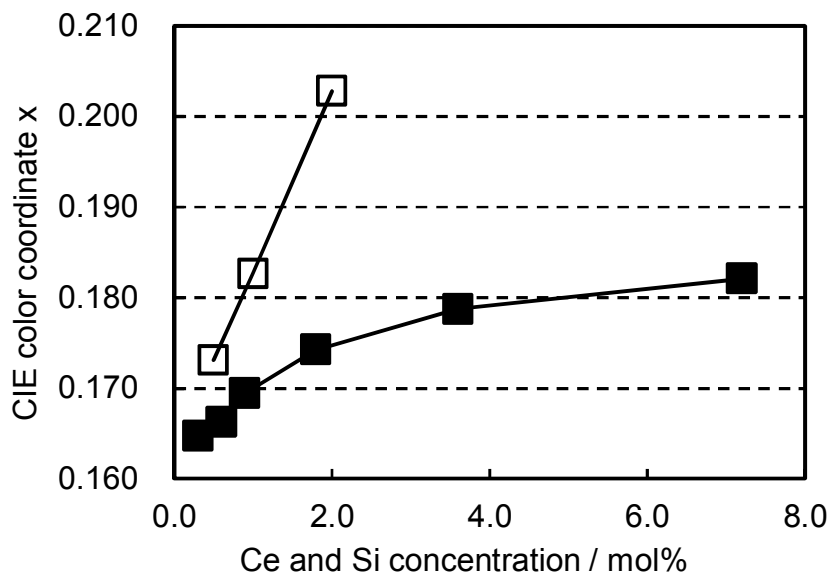


Figure 8-8 Color shift as a function of Ce concentration excited at 400 nm;

□: $(\text{Ca}_{1-x}\text{Ce}_x)_6\text{Ba}(\text{PO}_4)_4\text{O}$, ■: $(\text{Ca}_{1-x}\text{Ce}_x)_6\text{Ba}(\text{P}_{1-6x/4}\text{Si}_{6x/4}\text{O}_4)_4\text{O}$.

Apparent differences in the shape of the excitation spectra was also observed between Ce^{3+} single doping and $\text{Ce}^{3+}/\text{Si}^{4+}$ co-doping. To probe the reason for the small emission color shift in the $\text{Ce}^{3+}/\text{Si}^{4+}$ samples, the lowest energy excitation band was decomposed into two Gaussian components for the Ca1 and Ca2 sites. Figure 8-9 shows the results for the lowest energy excitation bands of CBP activated with 0.9 mol% of Ce^{3+} and with 0.9 mol% of $\text{Ce}^{3+}/\text{Si}^{4+}$, respectively. These decompositions for samples with various doping levels indicated clear differences in the site preference of Ce^{3+} between single doping and co-doping. For both Ca1 and Ca2 sites (assuming that Ca2 excites at a longer wavelength), peak positions shift to the longer wavelength side with single doping. By contrast, the peak positions shift to shorter wavelengths in co-doped samples (Figure 8-10). A slight red shift can be expected due to the reabsorption with increasing Ce^{3+} concentration, as explained above. However, a large blue shift in the co-doping samples overwhelms the red shift and can be attributed to the weakening crystal field on both the Ca1 and Ca2 sites as the lattice expands. Figure 8-11 shows the relative peak intensities of the lowest energy excitation band for Ce^{3+} on the Ca2 site against its intensity at 0.3 mol% doping and indicates a preference of Ce^{3+} for the Ca2 site. Single doping does not increase the relative peak intensity, which implies that only co-doping stimulates the relative preference of substitution by Ce^{3+} for the Ca2 site, which is relatively compressed by comparison with Ca1.

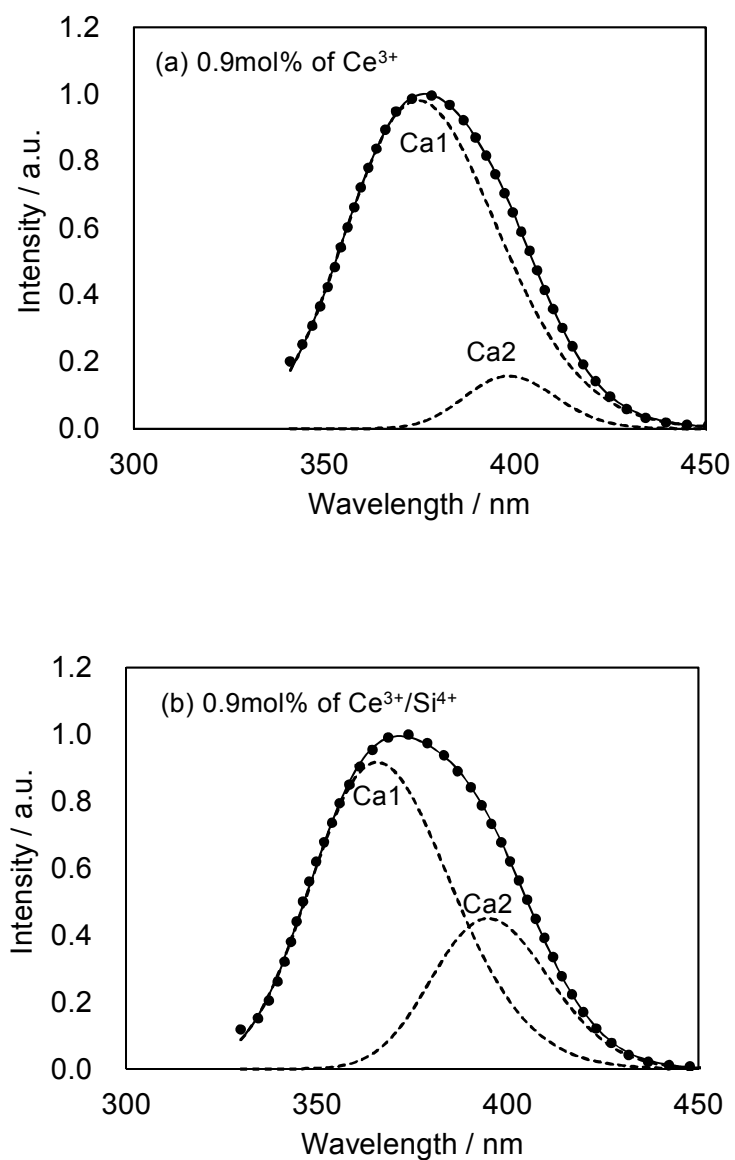


Figure 8-9 Decomposition of the lowest energy excitation band monitored at 480 nm. Observed (dotted line), fitted curve (solid line) and deconvoluted Gaussian components for Ca1 and Ca2 sites (dashed lines). (a) CBP activated with 0.9 mol% of Ce^{3+} (b) CBP activated with 0.9 mol% of $\text{Ce}^{3+}/\text{Si}^{4+}$.

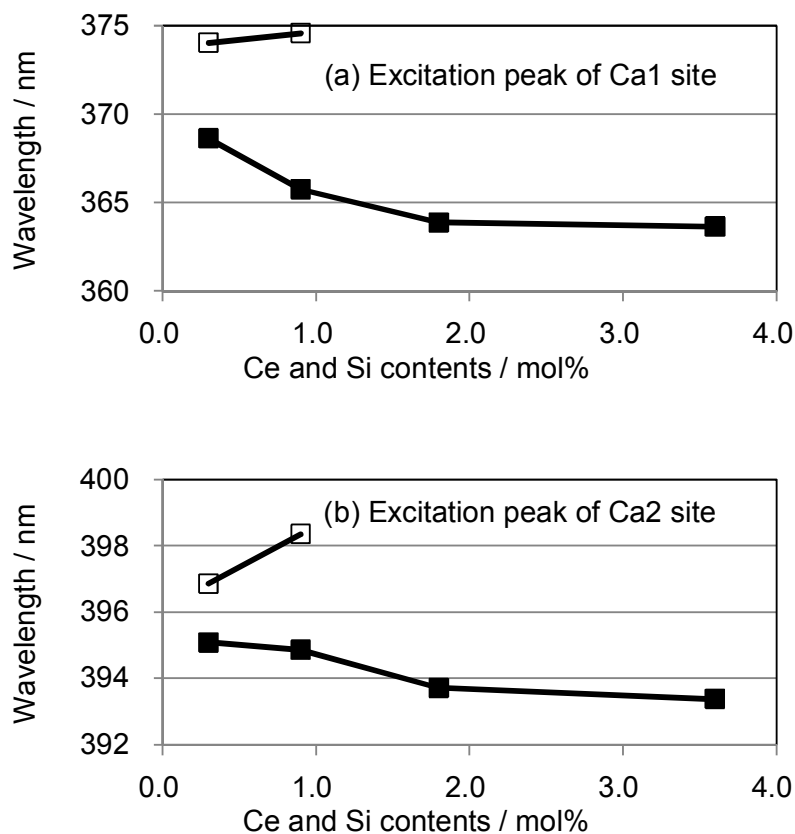


Figure 8-10 Peak positions of the deconvoluted excitation bands for (a) Ca1 and (b) Ca2;
 □: $(\text{Ca}_{1-x}\text{Ce}_x)_6\text{Ba}(\text{PO}_4)_4\text{O}$, ■: $(\text{Ca}_{1-x}\text{Ce}_x)_6\text{Ba}(\text{P}_{1-6x/4}\text{Si}_{6x/4}\text{O}_4)_4\text{O}$.

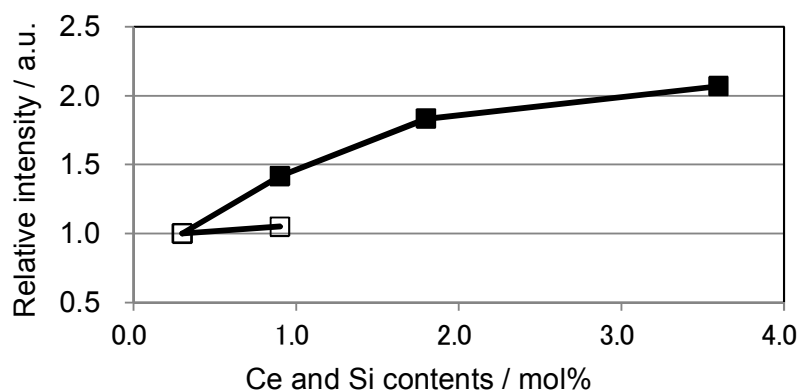


Figure 8-11 Relative peak intensity of the deconvoluted excitation band monitored at 480 nm for Ca2 site normalized at 0.3 mol% doping level; □: $(\text{Ca}_{1-x}\text{Ce}_x)_6\text{Ba}(\text{PO}_4)_4\text{O}$, ■: $(\text{Ca}_{1-x}\text{Ce}_x)_6\text{Ba}(\text{P}_{1-6x/4}\text{Si}_{6x/4}\text{O}_4)_4\text{O}$.

As shown in Figure 8-12, substitution of Si into P sites generates no second phases. Figure 8-13 shows the unit cell volume of the CBP samples as a function of Ce^{3+} or $\text{Ce}^{3+}/\text{Si}^{4+}$ doping concentration. Co-doping expands the unit cell volume with increasing $\text{Ce}^{3+}/\text{Si}^{4+}$ concentration due to substitution of Si on the P site (the ionic radii of the four-coordinated Si and P are 0.26 Å and 0.17 Å, respectively). Effective charge compensation has been previously reported for Ce^{3+} doping into the Ca site in $(\text{Ca},\text{Ce})_3\text{Sc}_2\text{Si}_3\text{O}_{12}$, replacing Sc^{3+} by Mg^{2+} and Ca^{2+} by Na^+ or Li^+ .¹⁴ Similarly, Al^{3+} substitution has been reported to maintain γ -phase formation and control the distribution of Ce^{3+} in $\text{Ca}_2\text{SiO}_4:\text{Ce}^{3+}$.¹⁵ The present work can be the first report of effective charge compensation for Ce-doped alkaline-earth phosphate phosphors by co-doping with Si, though Si substitution in phosphates is well-known in AlPO_4 -based molecular sieves.¹⁶

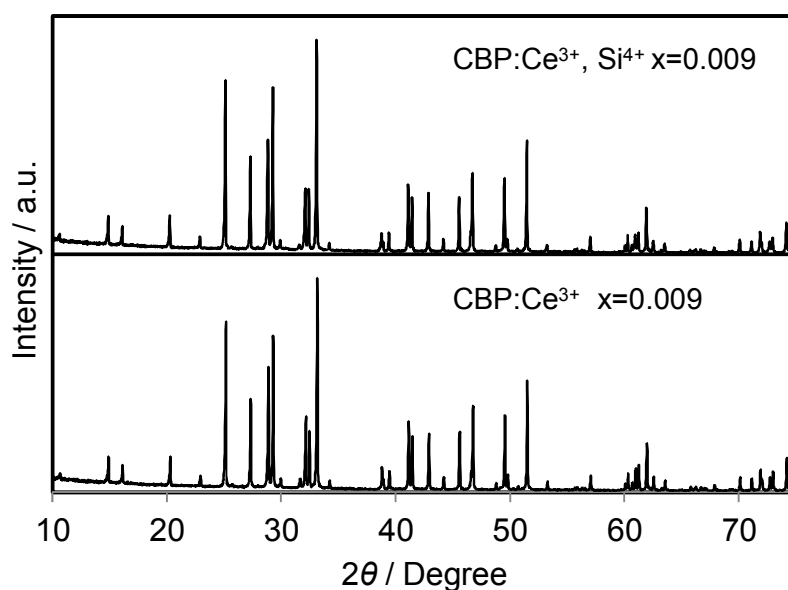


Figure 8-12 Experimental PXRD patterns of $(\text{Ca}_{1-x}\text{Ce}_x)_6\text{Ba}(\text{PO}_4)_4\text{O}$ and $(\text{Ca}_{1-x}\text{Ce}_x)_6\text{Ba}(\text{P}_{1-6x/4}\text{Si}_{6x/4}\text{O}_4)_4\text{O}$ in the range of $2\theta = 10\text{--}75^\circ$.

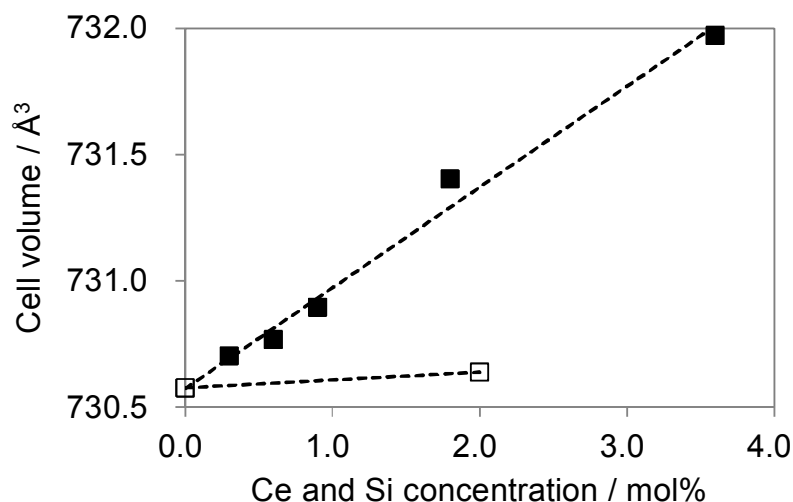


Figure 8-13 Cell volume expansion as a function of Ce^{3+} concentration;

□: $(\text{Ca}_{1-x}\text{Ce}_x)_6\text{Ba}(\text{PO}_4)_4\text{O}$, ■: $(\text{Ca}_{1-x}\text{Ce}_x)_6\text{Ba}(\text{P}_{1-6x/4}\text{Si}_{6x/4}\text{O}_4)_4\text{O}$.

The marked increase in unit cell volume probably accounts for the blue-shift in the emission as the level of $\text{Ce}^{3+}/\text{Si}^{4+}$ co-doping increases. The absence of such an increase with single Ce^{3+} doping is expected since there is no obvious reason in this case for the lattice to expand. Furthermore, charge compensation must be achieved by a more complex mechanism, which probably limits the solubility. However, the underlying reason for the relative preference for Ce^{3+} substitution at the Ca2 site in the case of co-doping is less clear. The most likely explanation is that single doping leads to a preference for Ce^{3+} substitution at the Ca1 site, where charge compensation could be partly met by the higher oxygen coordination number. This is less necessary in the co-doped sample, leading to a more even distribution of Ce^{3+} over the two sites.

The combination of a uniform Ce distribution, in order to minimize concentration quenching, and insertion of the Ce^{3+} into the more compressed Ca2 site is important in order to match the excitation range with near-UV LEDs. $\text{Ce}^{3+}/\text{Si}^{4+}$ co-doping enables this, and improves the luminescent intensity of $\text{CBP}:\text{Ce}^{3+},\text{Si}^{4+}$. Based on the 90 % internal quantum efficiency of BAM at 300 nm,¹⁷ the internal quantum efficiency of $\text{CBP}:\text{Ce}^{3+},\text{Si}^{4+}$ is 70 % at 400 nm excitation, which is higher than the value of 60 % reported for $\text{Ba}_9\text{Y}_2\text{Si}_6\text{O}_{24}:\text{Ce}^{3+}$ by Seshadri *et al.*⁴ Comparing the value with the 74 % achieved for P46-Y3 at 455 nm excitation measured in same configuration, $\text{CBP}:\text{Ce}^{3+},\text{Si}^{4+}$ is a very promising phosphor for LED use. It shows better performance than any of the other Ce^{3+} doped phosphates that we have studied, an observation that we ascribe to the presence of isolated oxide ions in the coordination sphere of the calcium ions.

Figure 8-14 shows the reflectance spectra for undoped and Ce-doped CBP. The reflectance of undoped CBP remains at about 90 % in the spectral range of 250-750 nm, with a sudden drop below 250 nm corresponding to the absorption at the bandgap in CBP. The Ce^{3+} doping introduces a strong, broad absorption in the range 200-450 nm associated with its $4f^1 \rightarrow 5d^1$ transition. The slightly lower reflectance of only 83.5 % in the range

above 450 nm may be linked to compensation of the charge balance in the $\text{CBP}:\text{Ce}^{3+}$ by defects such as Ca vacancies. For reference, 0.3 mol% $\text{Ce}^{3+}/\text{Si}^{4+}$ doped CBP maintains 85 % reflectance in this range.

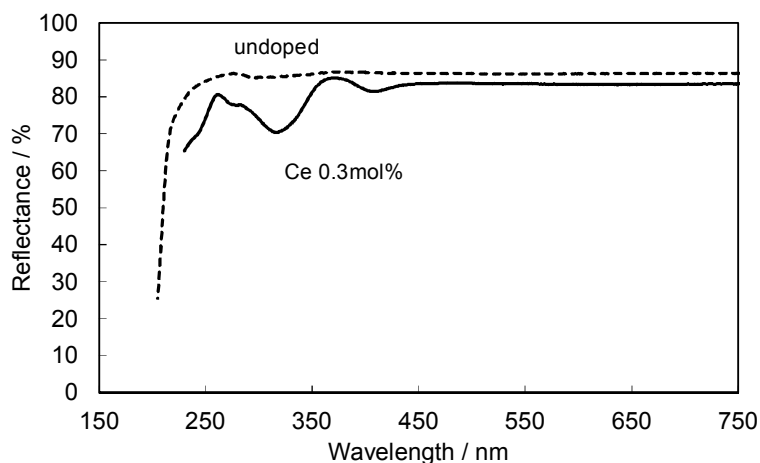


Figure 8-14 Reflectance spectra of an undoped CBP sample (dashed line) and a sample doped with 0.3 mol% of Ce (solid line).

8.3.4 Temperature dependence of the photoluminescence

One of the key requirements for a good phosphor for SSL is the need to maintain performance at the operating temperature of the device. Figure 8-15 shows the temperature dependence of the photoluminescence of $(\text{Ca}_{0.982}\text{Ce}_{0.018})_6\text{Ba}(\text{P}_{0.982}\text{Si}_{0.018}\text{O}_4)_4\text{O}$ excited at 400 nm, compared with P46-Y3 excited at 455 nm. $\text{CBP}:\text{Ce}^{3+}$ showed much smaller thermal quenching than P46-Y3, maintaining 80 % of light output at 150 °C whereas P46-Y3 retains only 40 %. CBP exhibits quite small color shift in the temperature range of 25 to 150 °C, which is suitable for LED use.

The temperature dependence of PL was measured below room temperature from 75 K to 300 K (Figure 8-16 for $\text{CBP}:\text{Eu}^{2+}$ and Figure 8-17 for $\text{CBP}:\text{Ce}^{3+}$). Interestingly, when temperature increases, $\text{CBP}:\text{Ce}^{3+}$ presents no blue shift. It can be attributed to the energy split of the $5d$ level of Ce^{3+} into E_g and T_{2g} , which is much clearer and well split than $5d$ of Eu^{2+} . The energy difference of the $5d$ level between E_g and T_{2g} can be roughly estimated by the shape of excitation spectra, and it is about 0.8 eV from Figure 8-4. For example, in $\text{CBP}:\text{Eu}^{2+}$, the energy difference of 0.12 eV is estimated by the peak shift from about 580 nm to 550 nm (Figure 8-16). This energy increase by thermally assistance may not be enough for the energy split of $5d$ in Ce^{3+} .

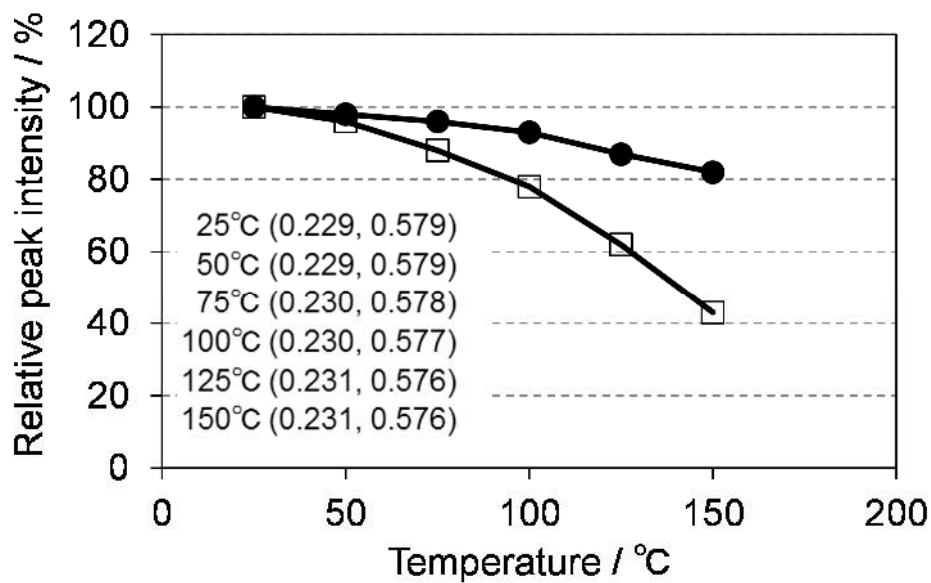


Figure 8-15 Temperature dependence of the photoluminescence of $(\text{Ca}_{0.982}\text{Ce}_{0.018})_6\text{Ba}(\text{P}_{0.982}\text{Si}_{0.018}\text{O}_4)_4\text{O}$ excited at 400 nm (filled circles) and P46-Y3 excited at 455 nm (open squares). The inset shows color coordinates at each temperature.

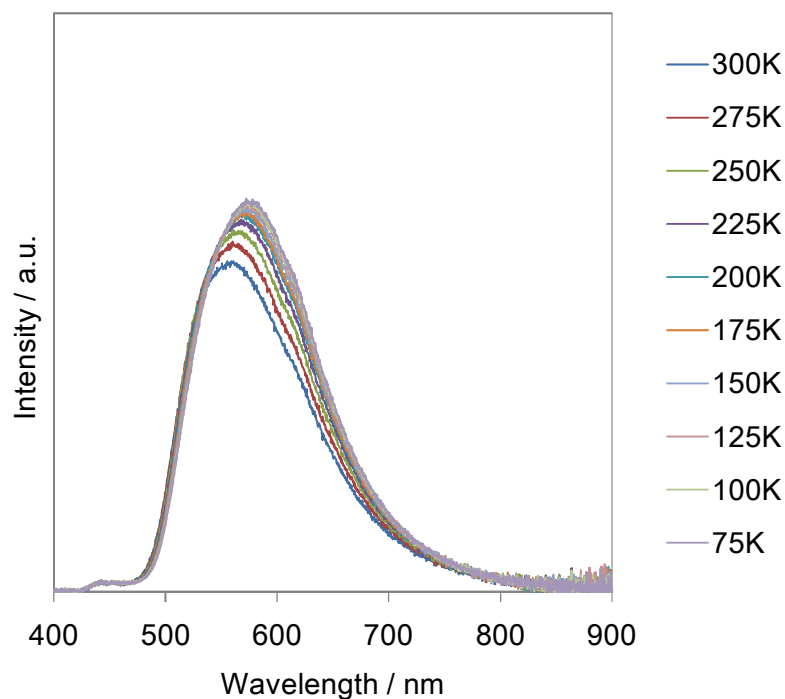


Figure 8-16 PL of CBP activated with 1 mol% of Eu^{2+} , excited by 400 nm near UV LED light at lower temperature from 75 K to 300 K.

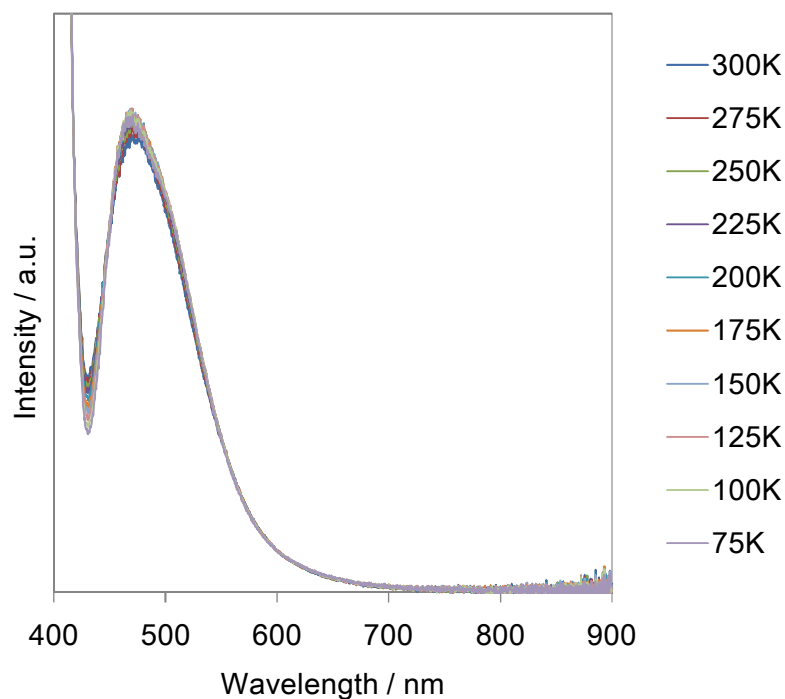


Figure 8-17 PL of CBP activated with 1 mol% of Ce^{3+} , excited by 400 nm near UV LED light at lower temperature from 75 K to 300 K.

8.3.5 Luminescence from a white LED

The $\text{CBP}:\text{Ce}^{3+},\text{Si}^{4+}$ phosphor is highly suitable as a blue-green phosphor for SSL based upon near-UV LEDs operating at 400 nm. Equally, $\text{CBP}:\text{Eu}^{2+}$ is an exceptional yellow phosphor for the same LED wavelength since its excitation spectrum spans from about 250 to over 450 nm.⁵ The PL and PLE spectra of two samples of $\text{CBP}:\text{Ce}^{3+},\text{Si}^{4+}$ and $\text{CBP}:\text{Eu}^{2+}$ underline this point (Figure 8-18). The white LED is therefore fabricated consisting of the $\text{CBP}:\text{Ce}^{3+},\text{Si}^{4+}$ (blue-green), $\text{CBP}:\text{Eu}^{2+}$ (yellow), $\text{CaAlSi}_3\text{N}_3:\text{Eu}^{2+}$ (red),¹⁸ and a near-UV LED with emission at 400 nm (Figure 8-19). Its correlated color temperature (CCT) was 4448 K and the CIE color coordinates were (0.370, 0.403). The luminous efficacy and external quantum efficiency of the LED at a high forward current of 350 mA were 45 lmW^{-1} and 20.8 %, respectively. It achieved a relatively flat, broad spectrum from blue to red with good color quality at an average color rendering index (Ra) of 93. The observed CIE chromaticity coordinates of white LED were distinctly stable within $x=0.370\text{-}0.380$ and $y=0.403\text{-}0.408$ at the operation current from 20 mA to 350 mA. Amazingly, The Ra were unchanged at all in this range.

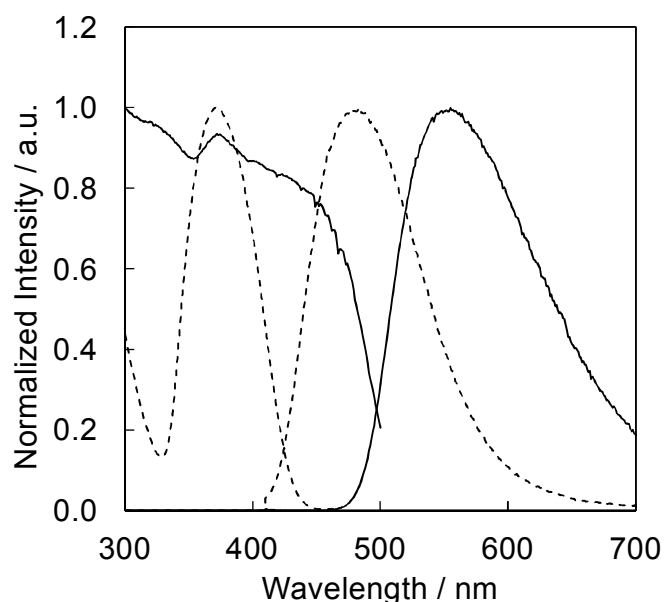


Figure 8-18 PL and PLE spectra of CBP activated with Eu^{2+} (solid line) and Ce^{3+} (dashed line). Excited at 400 nm for both, monitored at 550 nm for $\text{CBP}:\text{Eu}^{2+}$ and at 480 nm for $\text{CBP}:\text{Ce}^{3+}$.

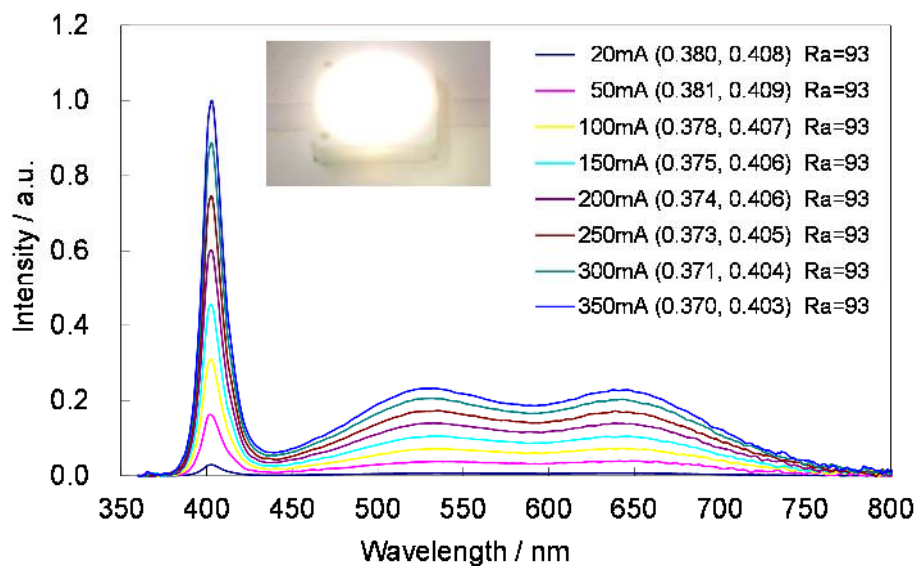


Figure 8-19 Luminescence spectrum of a white LED consisting of the $\text{CBP}:\text{Ce}^{3+},\text{Si}^{4+}$, $\text{CBP}:\text{Eu}^{2+}$, $\text{CaAlSi}_3\text{N}_3:\text{Eu}^{2+}$ phosphor and a near-UV LED. The inset shows a photograph of the white LED in operation, color coordinates and Ra at each operation current.

8.4 Summary

A new blue-green phosphor, $\text{Ca}_6\text{Ba}(\text{PO}_4)_4\text{O}:\text{Ce}^{3+}$, has been reported. Co-substitution of P with Si was used as an effective mechanism to enhance the luminescence; $\text{Ca}_6\text{Ba}(\text{PO}_4)_4\text{O}:\text{Ce}^{3+},\text{Si}^{4+}$ shows strong blue-green emission with a peak position at 480 nm and a high internal efficiency of 70 %. Thermal quenching of the luminescence is much smaller than in P46-Y3. A white LED using $\text{CBP}:\text{Ce}^{3+},\text{Si}^{4+}$, $\text{CBP}:\text{Eu}^{2+}$, $\text{CaAlSi}_3\text{N}_3:\text{Eu}^{2+}$ and a near-UV LED showed excellent performance.

8.5 References

- 1 G. Gundiah, J. L. Wu and A. K. Cheetham, *Chem. Phys. Lett.* 2007, **441**, 250.
- 2 A.A. Setlur and U. Happek, *J. Solid State Chemistry*, 2010, **183**, 1127.
- 3 K. A. Denault, N. C. George, S. R. Paden, S. Brinkley, A. A. Mikhailovsky, J. Neuefeind, S. P. DenBaars and R. Seshadri, *J. Mater. Chem.* 2012, **22**, 18204.
- 4 J. Brgoch, C. K. H. Borg, K. A. Denault, A. A. Mikhailovsky, S. P. DenBaars and R. Seshadri, *Inorg. Chem.* 2013, **52**, 8010.
- 5 N. Komuro, M. Mikami, Y. Shimomura, E. G. Bithell and A. K. Cheetham, *J. Mater. Chem. C*, 2014, **2**, 6084.
- 6 K. Y. Jung and J. H. Kim, *J. Lumin.* 2008, **128**, 2004.
- 7 X. Zhang, H. He, Z. Li, T. Yu and Z. Zou, *J. Lumin.* 2008, **128**, 1876.
- 8 M. Shang, G. Li, D. Geng, D. Yang, X. Kang, Y. Zhang, H. Lian and J. Lin, *J. Phys. Chem. C*, 2012, **116**, 10222.
- 9 T. J. B. Holland and S. A. T. Redfern, *Miner. Mag.*, 1997, **61**, 65.
- 10 K. Momma and F. Izumi, *J. Appl. Crystallogr.* 2011, **44**, 1272.
- 11 R. D. Shannon, *Acta Crystallogr. Sect. A*, 1976, **32**, 751.
- 12 P Dorenbos, *J. Phys.: Condens. Matter*, 2003, **15**, 4797
- 13 K. Sakuma, N. Hirosaki and R.-J. Xie, *J. Lumin.*, 2007, **126**, 843.
- 14 Y. Shimomura, T. Kurushima, M. Shigeiwa and N. Kijima, *J. Electrochem. Soc.*, 2008, **155**, J45
- 15 A. Kalaji, M. Mikami and A. K. Cheetham, *Chem. Mater.* 2014, **26**, 3966.
- 16 M. Lok, C. A. Messina, R. L. Patton, R. T. Gajel, T. R. Cannan, and E. M. Flanigen, *J. Amer. Chem. Soc.* 1984, **106**, 6092.
- 17 A. Bol and A. Meijerink, *J. Phys. Chem. B*, 2001, **105**, 10197
- 18 K. Uheda, N. Hirosaki, Y. Yamamoto, A. Naito, T. Nakajima, and H. Yamamoto, *Electrochem. & Sol. State Lett.* 2006, **9**, H22.

Chapter 9 Conclusions

This dissertation was concerned with the study to establish the relation between the crystal structure and luminescence of phosphors to suggest clues to find new practical phosphors for SSL.

As an introduction, the background of this research was explained. In Chapter 2, the technical background of this research was presented including some recent technologies aiming to balance the prosperity of human beings and environmental conservation. In Chapter 3, the fundamentals of photoluminescence in phosphors were explained with particular attention paid to Ce^{3+} and Eu^{2+} ions, followed by the introduction to some practical phosphors regarding the crystal structure and the emission performance. In Chapter 4, the experimental methods used for sample preparation and characterization were introduced including some fundamentals of analysis.

In Chapter 5, the considerably broad emission of $\text{Ca}_4(\text{PO}_4)_2\text{O}:\text{Eu}^{2+}$ phosphor at 77 K covering from 500 nm to 800 nm was studied. The relation between the crystal structure and emission spectra was discussed by refining the crystal structure of $\text{Ca}_4(\text{PO}_4)_2\text{O}:\text{Eu}^{2+}$ using powder neutron diffraction data. The importance of the higher anion polarizability and the heavy distortion of the coordination polyhedra were highlighted. The idea of the ECoN was introduced for describing the degree of distortion differentiating the eight Ca sites in the $\text{Ca}_4(\text{PO}_4)_2\text{O}:\text{Eu}^{2+}$ structure and related to the broad emission spectra. The different thermal quenching on the representing two Ca sites was also discussed and attributed to the degree of auto ionization.

In Chapter 6, the new red phosphor, $\text{Sr}_4(\text{PO}_4)_2\text{O}:\text{Eu}^{2+}$, was studied. The crystal structure of $\text{Sr}_4(\text{PO}_4)_2\text{O}:\text{Eu}^{2+}$ is isotopic to $\text{Ca}_4(\text{PO}_4)_2\text{O}:\text{Eu}^{2+}$, which also shows deep red emission. Their emission and excitation spectra at room temperature are very similar despite $\text{Sr}_4(\text{PO}_4)_2\text{O}:\text{Eu}^{2+}$ having a much larger unit cell volume than $\text{Ca}_4(\text{PO}_4)_2\text{O}:\text{Eu}^{2+}$. The importance of the higher anion polarizability and the heavy distortion of the coordination polyhedron were confirmed based on the idea of the electronegativity of the cations and the ECoNs. The different thermal quenching behaviors for Eu^{2+} dopants in $\text{Sr}_4(\text{PO}_4)_2\text{O}:\text{Eu}^{2+}$ and $\text{Ca}_4(\text{PO}_4)_2\text{O}:\text{Eu}^{2+}$ were also discussed and attributed to the degree of auto/photo-ionization caused by the different band gaps of the materials. The importance of the large band gap of the host lattice in avoiding non-radiative processes of energy relaxation was also confirmed.

In Chapter 7, a new yellow phosphor, $\text{Ca}_6\text{Ba}(\text{PO}_4)_4\text{O}:\text{Eu}^{2+}$, has been reported. The unknown structure of $\text{Ca}_6\text{Ba}(\text{PO}_4)_4\text{O}$ was solved *ab initio* from synchrotron X-ray powder diffraction data. When combined with a blue InGaN LED, $\text{Ca}_6\text{Ba}(\text{PO}_4)_4\text{O}:\text{Eu}^{2+}$ shows good characteristics suitable for a white LED due to a broad excitation band from the near-UV to the blue region and strong yellow broader emission with a peak position at 553 nm, which attribute to the better color rendering index of white LEDs than P46-Y3 (YAG: typical commercial yellow phosphor).

In Chapter 8, a new blue-green phosphor, $\text{Ca}_6\text{Ba}(\text{PO}_4)_4\text{O}:\text{Ce}^{3+}$, has been reported. Co-substitution of Ca-P with Ce-Si was used as an effective measure to enhance the luminescence; $\text{Ca}_6\text{Ba}(\text{PO}_4)_4\text{O}:\text{Ce}^{3+},\text{Si}^{4+}$ shows strong blue-green emission with a peak position at 480 nm and a high internal efficiency of 70 %. Thermal quenching of the luminescence is much smaller than in P46-Y3. A white LED using $\text{Ca}_6\text{Ba}(\text{PO}_4)_4\text{O}:\text{Ce}^{3+},\text{Si}^{4+}$, $\text{Ca}_6\text{Ba}(\text{PO}_4)_4\text{O}:\text{Eu}^{2+}$, $\text{CaAlSiN}_3:\text{Eu}^{2+}$ and a near-UV LED showed excellent performance.

It is important for the host materials to balance the large band gap and the strong crystal field on the dopants (such as Eu^{2+} or Ce^{3+} ions). There is always conflict between them. When the electronegativity of metal cations is higher, which has an advantage for stronger crystal fields, that host material potentially has a smaller band gap, and vice versa. However isolated oxygen might help to solve this problem. As being introduced in this work, when the crystal structure has individual cation sites for the dopants (such as Eu^{2+} or Ce^{3+} ions) without making a solid solution in one phase, there are chances in the host material for a stronger crystal field on a dopant maintaining a large band gap. By designing the combination of cations with different electronegativities, ionic radii and valence numbers, it can be possible to control the site preference of the dopants into individual sites. This concept is so called crystal site engineering. It enables host materials to achieve strong crystal fields locally on particular sites. When it comes to finding new phosphors with multiple individual sites, isolated oxygen ions can be quite useful. First, the system with isolated oxygen ions has not been studied well yet, and multiple cation phases with different individual sites might have been difficult to find since it does not cover a wide area on the phase diagram compared with the solid solution phases. Therefore, very careful research activity might be required. Second, the isolated oxygen ion offers the chance of distorted polyhedral structures around cation sites since the polyhedral structures around oxygen ions are different between oxide units (such as phosphate) and isolated ones. Thus, utilizing the multiple cation structures and isolated oxygen ions will be a good stimulation to find new phases and/or phosphors in oxide system for SSL.

I hope this dissertation will be of interest to both the optical materials specialists and the broader materials chemistry community.

Acknowledgements

I am deeply grateful to the all support I received through my work in Mitsubishi Chemical Corporation, at University of Cambridge and at University of Tsukuba.

Working under the supervision of Prof. Katsuhiro Akimoto (Institute of Applied Physics, University of Tsukuba) was an absolute pleasure. I am very grateful for his guidance and support throughout the course of my PhD. He has been always supportive to me for about twenty years since I first enrolled in his laboratory for my master's degree at University of Tsukuba in 1996.

I wish to acknowledge Prof. Masahiro Sasaki, Prof. Toshiaki Hattori (Institute of Applied Physics, University of Tsukuba) and Prof. Satoshi Koizumi (NIMS: National Institute of Materials Science) for their incisive comments and valuable advice to this work. I wish to thank Prof. Akira Uedono (Institute of Applied Physics, University of Tsukuba) for motivating me to publish papers and to get PhD. It was the trigger all the way here. I also acknowledge Mr. Halim Abdul, who is my colleague at University of Tsukuba, for his assistance with the work in the University.

Most of this work was conducted under the collaboration between Mitsubishi Chemical Corporation and University of Cambridge in the UK from 2011 to 2013. I am deeply grateful to the supervision of Prof. Anthony K. Cheetham during my research in Cambridge and the continuing support thereafter. I would also like to thank him for encouraging me to attend conferences around the world that made my perspective broadened and brushed up my scientific insight.

I would like to thank all the members of the Functional Inorganics and Hybrid Materials Group at University of Cambridge (Thiru, Isabelle, Paul, Ali, Hamish, Erica, Satoshi, Shakiba, Ryan, Jin, Sebastian, Patrick, Tom, Emma, Wei, Shuai, Anna, Mark, Dhivya, Shijing and Clement). I thoroughly enjoyed working with them, including having tea time, playing squash and going out for Pub lunch. I must particularly thank some members of the group who helped me tremendously during my stay. Dr. Isabelle Etchart (currently at Saint-Gobain CertainTeed Ceilings), her guidance to the group was incredibly helpful for me to adapt to a new environment. Dr. Paul Saines (currently at University of Kent) taught me how to perform Rietveld refinements, and helped me to obtain neutron and X-ray synchrotron diffraction data. His expertise in crystal structure refinement supported my analysis moving forward. Dr. Erica G. Bithell (Institute of Continuing Education, University of Cambridge) helped me to obtain the electron diffraction data, which was essential for this work to solve the unknown new crystal structure. Dr. Thirumurugan Alagarsamy (currently at School of Chemistry Indian Institute of Science Education and Research), his gentle but stubborn attitude led us to in-depth discussion and he always showed full consideration for my family. Dr. Satoshi Tominaka (currently at NIMS), his coherent attitude to research taught me a lot about discipline as a researcher. I am still looking forward to having meaningful discussion with him. Dr. Hamish Yeung (currently at NIMS), he always showed his interest in anything. His curiosity never

ceased, which gave me a huge impact for a scientist. He also gave me a lot of valuable feedbacks on this dissertation. Finally, it was a delight to work with Dr. Ali Kalaji (currently at Cristal) in Cambridge. All his assistance with the experimental work at the University and living tips there were of great help for me and my family. Our discussions have been always constructive and informative for our next actions.

I also express my deepest gratitude to the members in Mitsubishi Chemical Group. Mr. Keizou Usui, my former boss in Mitsubishi Chemical Corporation, is the one who totally supported me to grab the chance working in Cambridge. I could have never had it without his support. Mr. Yukio Tokunaga and Dr. Takayuki Hisamune also backed me up for my challenge. Dr. Kyouta Uheda (MCRC: Mitsubishi Chemical Group - Science and Technology Research Center), he gave me an introduction to crystallography and the overview of the research abroad. Mr. Masashi Aoyagi, he helped me in PL measurement at low temperature and LED evaluations. I must particularly thank Dr. Masayoshi Mikami (MCHC R&D Synergy Center, Inc.) for his huge contribution to the computational work for the DOS and the theoretical discussion in this dissertation. I learnt a lot about photoluminescence through our discussions.

I would like to express my sincere gratitude to the two departed, who worked with me in Mitsubishi Chemical Corporation. The late Mr. Etsuo Shimizu, he taught me an overwhelming amount about phosphors and his profession influenced me a lot. The late Mr. Yuuji Yoshizumi, he always showed an interest with my work and always told me what I should be as an engineer.

Finally, I wish to thank my wife Keiko and my son Masayuki for being there for me in Cambridge, and for all their support during the period of the PhD.

List of Publications

[1] Journal of Materials Chemistry C, 2014, 2, 6084–6089

Synthesis, structure and optical properties of europium doped calcium barium phosphate – a novel phosphor for solid-state lighting

Naoyuki Komuro, Masayoshi Mikami, Yasuo Shimomura, Erica G. Bithell and Anthony K. Cheetham

[2] Journal of Materials Chemistry C, 2015, 3, 204–210

Synthesis, structure and optical properties of cerium-doped calcium barium phosphate – a novel blue-green phosphor for solid-state lighting

Naoyuki Komuro, Masayoshi Mikami, Yasuo Shimomura, Erica G. Bithell and Anthony K. Cheetham

[3] Journal of Luminescence 162 (2015) 25–30

Structure–property correlations in Eu-doped tetra calcium phosphate phosphor: A key to solid-state lighting application

Naoyuki Komuro, Masayoshi Mikami, Paul J. Saines and Anthony K. Cheetham

[4] Journal of Materials Chemistry C, 2015, 3, 7356–7362

Deep red emission in Eu²⁺-activated Sr₄(PO₄)₂O phosphors for blue-pumped white LEDs

Naoyuki Komuro, Masayoshi Mikami, Paul J. Saines, Katsuhiko Akimoto and Anthony K. Cheetham